Universität Stuttgart

Institut für Wasser- und Umweltsystemmodellierung

Mitteilungen

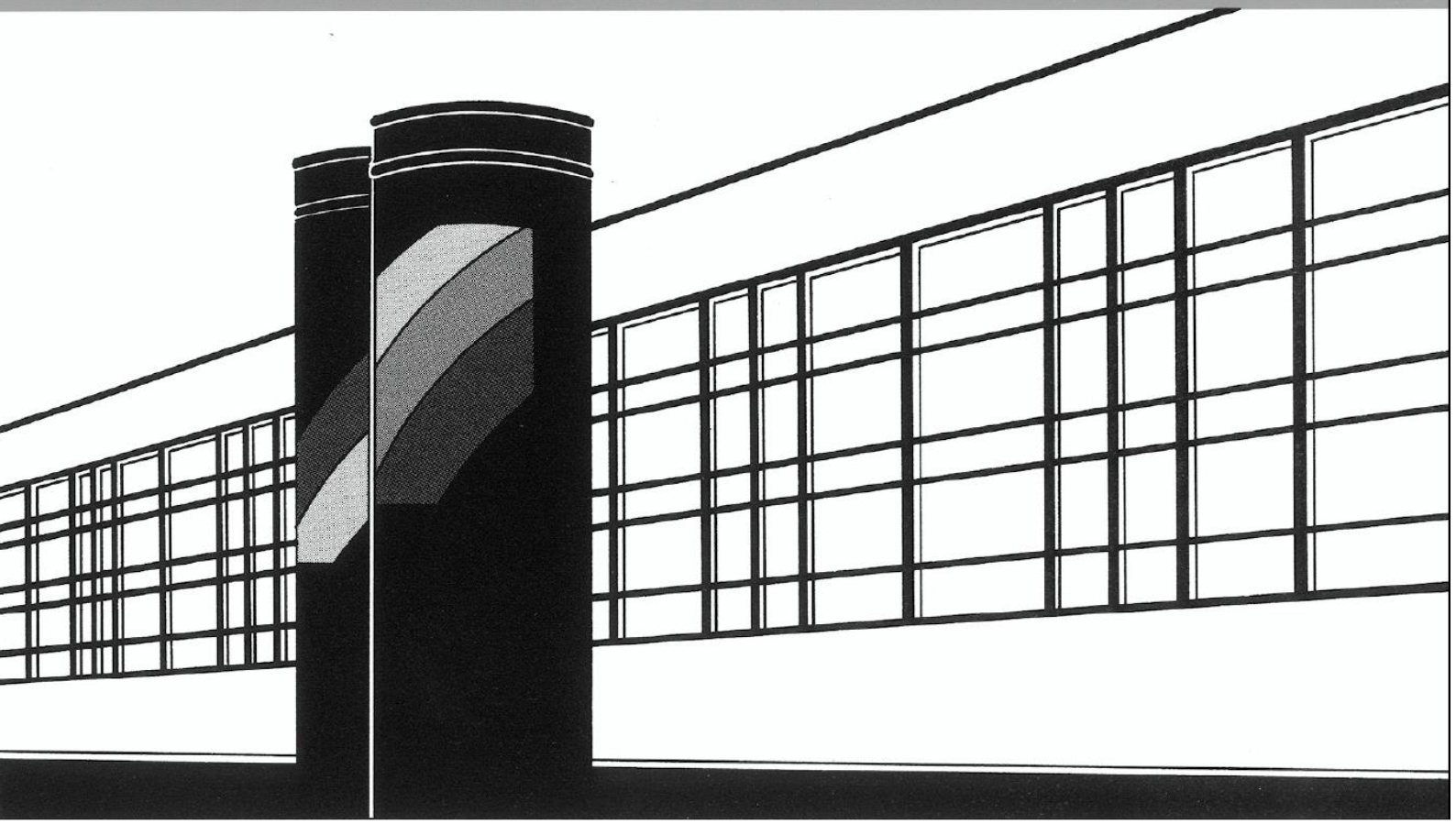

Heft 265 Martin Beck

Conceptual approaches for the analysis of coupled hydraulic and geomechanical processes

Conceptual approaches for the analysis of coupled hydraulic and geomechanical processes

von der Fakultät Bau- und Umweltingenieurwissenschaften der Universität Stuttgart zur Erlangung der Würde eines Doktor-Ingenieurs (Dr.-Ing.) genehmigte Abhandlung

vorgelegt von

Martin Michael Beck

aus Freiburg im Breisgau

Hauptberichter:	apl. Prof. Dr.-Ing. Holger Class
Mitberichter:	Prof. Dr.-Ing. Rainer Helmig
	Prof. Dr. Inga Berre

Tag der mündlichen Prüfung: 15. November 2018

Institut für Wasser- und Umweltsystemmodellierung
der Universität Stuttgart
2019

Heft 265

Conceptual approaches for the analysis of coupled hydraulic and geomechanical processes

von
Dr.-Ing.
Martin Beck

Eigenverlag des Instituts für Wasser- und Umweltsystemmodellierung
der Universität Stuttgart

D93 Conceptual approaches for the analysis of coupled hydraulic and geomechanical processes

Bibliografische Information der Deutschen Nationalbibliothek
Die Deutsche Nationalbibliothek verzeichnet diese Publikation in der Deutschen Nationalbibliografie; detaillierte bibliografische Daten sind im Internet über http://www.d-nb.de abrufbar

Beck, Martin:
Conceptual approaches for the analysis of coupled hydraulic and geomechanical processes, Universität Stuttgart. - Stuttgart: Institut für Wasser- und Umweltsystemmodellierung, 2019

(Mitteilungen Institut für Wasser- und Umweltsystemmodellierung, Universität Stuttgart: H. 265)
Zugl.: Stuttgart, Univ., Diss., 2019
ISBN 978-3-942036-69-6

NE: Institut für Wasser- und Umweltsystemmodellierung <Stuttgart>: Mitteilungen

Herausgegeben 2019 vom Eigenverlag des Instituts für Wasser- und Umweltsystem-modellierung

Druck: DCC Kästl e.K., Ostfildern

Danksagung

An dieser Stelle möchte allen danken, die mich auf dem Weg zu dieser Arbeit unterstützt und zu ihrem Gelingen beigetragen haben. Zuerst gilt mein Dank meiner Frau Katja, die für mich Rückhalt, Motivation und Ablenkung war. Dank ihr haben wir insbesondere die letzte Phase dieser Arbeit, die mit der Geburt unserer Tochter Pia zusammenfiel, gut gemeistert. Pia wiederum danke ich für die freundlichen und fröhlichen Begrüßungen zu Hause. Auch meinen Eltern möchte ich an dieser Stelle für ihre ungebrochene Unterstützung und ihr immer offenes Ohr danken.

Meinem Hauptberichter Holger Class gebührt ein besonderer Dank. Mit seiner ruhigen und gelassenen Art hat er mir immer wieder Rückhalt und Vertrauen vermittelt. Er überließ mir während meiner Arbeit viele Freiheiten, um eigenen Ideen nachzugehen, und stand gerne für Diskussionen zu neuen Ergebnissen und Einfällen zur Verfügung. In schwierigen Situationen hat er mir mit seiner Kompetenz und Erfahrung weitergeholfen und mich mit seinem Optimismus und seiner Gelassenheit unterstützt. Auch abseits der Forschung wird mir manches gemeinsame Erlebnis in Erinnerung bleiben, insbesondere unsere Dienstreisen nach Mailand, Barcelona und Israel. Neben der Übernahme des Mitberichts danke ich Rainer Helmig für seine offene und menschliche Art, mit der er die einzigartige Stimmung am Lehrstuhl prägt. Seine Lebendigkeit motiviert, erlaubt tolle fachliche wie außerfachliche Diskussionen und schafft Kontakte, von denen insbesondere seine Doktoranden profitieren. I also want to thank Inga Berre for co-supervising my thesis and for a warm welcome whenever I met her on conferences, workshops or in Bergen.

Prudence Lawday, Maria Costa und Stefanie Siegert haben mir dankenswerterweise beim Umgang mit der Verwaltung und Bürokratie weitergeholfen. Michelle Hartnick und David Werner bin ich dankbar für ihre Unterstützung bei Computerproblemen. Meinem langjährigen Zimmerkollegen Martin danke ich für die gute Atmosphäre im Büro sowie für Rat und Tat, wenn ich mal nicht weiterwusste. Auch sein stetiges Bewerben des Eclipse Debuggers soll an dieser Stelle honoriert werden. Gabi und Sina waren treue Mitläuferinnen bei der freitäglichen Jogging-Runde, die für mich eine willkommene Abwechslung zur Arbeit am Schreibtisch war. Christoph gilt mein Dank in zahlreicher Funktion: Seine Kommentare haben mir beim Schreiben dieser Arbeit weitergeholfen. Und ohne sein Drängen, frühzeitig damit zu beginnen, wäre die Endphase meiner Dissertation sicher anstrengender geworden. Und auch wenn die von ihm geschätzte Laufroute wohl nun in Vergessenheit gerät, hat er mit seinen Gesprächsthemen unsere Laufgruppe während seiner Zeit als Kollege bereichert. Bernd Flemisch gilt mein Dank als leitender Entwickler von DuMu^{x} ebenso wie für hilfreiche Tipps und geduldige Fehlersuchen. Auch dem Rest der Kollegen danke ich an dieser Stelle für die produktive Zusammenarbeit und die gute Arbeitsatmosphäre.

Der DFG danke ich für die finanzielle Unterstützung im Rahmen des Graduiertenkollegs NUPUS (IRTG 1398) und des Sonderforschungsbereichs 1313. Die Europäische Union hat dankenswerterweise meine Arbeit im Rahmen des Projektes FracRisk (Grant Agreement No. 636811) unterstützt.

Contents

List of Figures **V**

List of Tables **IX**

Nomenclature **XI**

Abstract **XV**

Zusammenfassung **XVII**

1 Introduction **1**

1.1 Hypotheses 2

1.2 Structure of the thesis 3

2 Fundamentals **5**

2.1 Fluid flow through porous media 5

2.1.1 The porous medium 5

2.1.2 Scales 6

2.1.3 Porosity 8

2.1.4 Phases 9

2.1.5 Saturation 9

2.1.6 Permeability 10

2.1.7 Capillary pressure 10

2.1.8 Relative permeability 12

2.1.9 Advection 14

2.2 Rock mechanics 15

2.2.1 Rock classification 15

2.2.2 Definition of stress 16

2.2.3 Displacement and strain 18

2.2.4 Linear Elasticity 21

2.3 Poroelasticity 24

2.3.1 Effective Porosity 25

2.3.2 Effective Permeability . . . 27
2.3.3 Transformation of the stress tensor . . . 28
2.3.4 Mohr's circle . . . 30
2.3.5 Rock Failure . . . 32
2.3.6 Failure evaluation . . . 33
2.4 Summary . . . 36

3 Modelling flow and geomechanics in porous media 37
3.1 Balance equations . . . 38
3.1.1 Mass balance equations . . . 38
3.1.2 Momentum balance equation . . . 39
3.1.3 Constitutive equations and supplementary constraints . . . 41
3.2 Spatial discretisation . . . 42
3.2.1 Box method . . . 43
3.2.2 Standard Galerkin finite element method . . . 44
3.3 Temporal discretisation . . . 45
3.4 Solution strategies . . . 45
3.4.1 Fully-coupled scheme . . . 46
3.4.2 Fixed-stress scheme . . . 46
3.5 Simulation software . . . 51
3.6 Homogeneous one-phase numerical test case . . . 51
3.6.1 Scenario description . . . 51
3.6.2 Comparison with TOUGH-FLAC . . . 52
3.6.3 Comparison Fixed-stress - Fully-coupled . . . 54
3.6.4 Conclusions . . . 58
3.7 CO_2 injection numerical test case . . . 58
3.7.1 Scenario description . . . 58
3.7.2 General results . . . 60
3.7.3 Fully-coupled and fixed-stress . . . 66
3.7.4 Conclusions . . . 69
3.8 Efficiency comparison . . . 69
3.8.1 Theoretical considerations . . . 69
3.8.2 Numerical test case . . . 70
3.9 Conclusions . . . 73

4 Fault reactivation 75
4.1 Modelling concepts . . . 76

4.2 Lab-scale numerical test cases 78
4.2.1 Homogeneous rock sample 78
4.2.2 Heterogeneous rock sample with a fault 79
4.2.3 Conclusions 80
4.3 Field-scale numerical test cases 82
4.3.1 Scenario description 82
4.3.2 Results 84
4.3.3 Effect of the permeability 88
4.3.4 Conclusions 90

5 Summary **93**
5.1 Conclusions and Outlook 94

Bibliography **97**

A Derivation of the effective porosity **109**

B Software **113**

List of Figures

2.1 Images of a Berea Sandstone sample obtained with different techniques. . . . 5
2.2 Structure of a Barnett Shale sample on different spatial scales. 6
2.3 Definition of a representative elementary volume. 8
2.4 Example for the transfer from the micro-scale to the macro-scale. 9
2.5 Capillary pressure-saturation relationship for a Barnett Shale sample and for a Berea Sandstone sample. 12
2.5 Examples for relative permeability curves. 13
2.6 Stress definition. 17
2.7 Visualisation of stress components on a cube in three dimensions. 18
2.8 Visualisation for the definitions of displacement and strain. 19
2.9 Laboratory measurements for stress and strain of a cylindrical Berea Sandstone sample. 21
2.10 Illustration of the different elastic moduli. 22
2.11 Stress components in different coordinate systems. 30
2.12 The Mohr circle. 31
2.13 Effect of the pore pressure on the Mohr circle. 32
2.14 Examples for different types of fractures. 33
2.15 The Mohr circle and failure (worst case). 34
2.16 The Mohr circle and failure. 34
2.17 The Mohr circle in three dimensions. 36

3.1 Weighting functions and basis functions for the presented methods. 43
3.2 Numerical routine for the original version of TOUGH-FLAC using the pore compressibility (top), for the recent version using the fixed-stress assumption (middle) and for the iterative fixed-stress scheme as implemented in DuMu^{x} (bottom). 50
3.3 Set-up of the homogeneous one-phase test case (left) and domain discretisation (right). 52

3.3 Pressure evolution at the injection simulated using TOUGH-FLAC, and the cell-centred (CC) discretisation in DuMu^{x} for a fixed-stress scheme with just one coupling step (equal to zero iterations) and a fully-converged simulation. 53
3.4 Comparison of selected geomechanical parameters. 54
3.5 Evolution of the pressure p over time for different solution strategies. 55
3.6 Deviation in percent of the zero-iteration fixed-stress scheme relative to the fully-iterate scheme at different points in time. 56
3.7 Evolution of the pressure p depending on the number of sequential iterations. 57
3.8 Comparison of the displacements. 57
3.9 Set-up of the CO_2 scenario (left) and domain discretisation (right). 59
3.10 Evolution of p_w and S_n over time at different locations. 61
3.11 Spatial distribution of the CO_2 saturation S_n and the wetting pressure p_w for two points in time during the pressure build-up phase of the simulation. . . . 62
3.12 Spatial distribution of the CO_2 saturation S_n and the wetting pressure p_w at two points in time during the pressure decrease. 63
3.13 Pressure evolution for different scenario variations. 64
3.14 Comparison of the displacements. 65
3.15 Deformation of the cells around the injection exaggerated by a factor of 1000. 66
3.16 Pressure over sequential iterations for fully-coupled and fixed-stress scheme. . 66
3.17 Comparison of the temporal evolution of p_w and S_n obtained using the fully-coupled and the fixed-stress scheme with zero iterations. 67
3.18 Comparison of the spatial distribution of p_w and S_n obtained using the fully-coupled and the fixed-stress scheme with zero iterations in an early stage of the simulation ($t = 100$ days for p_w, $t = 200$ days for S_n). 68
3.19 Comparison of the spatial distribution of p_w and S_n obtained using the fully-coupled and the fixed-stress scheme with zero iterations at $t = 900$ days. . . . 68
3.20 Setup of the test case for measuring the computational effort. 71
3.21 Measured ratio of numbers of instruction/unknowns^2 for different numbers of unknowns. 73

4.1 Compression of a homogeneous rock sample. 79
4.2 Compression of a heterogeneous rock sample. 81
4.3 Set-up of the hydraulic fracturing scenario after Rutqvist et al. (2013) (left) and domain discretisation (right). 82
4.4 Pressure and stress evolution over time at the injections cell in the fault in 1475 m depth for a fault permeability $k_{fault} = 5.0 \cdot 10^{-13}$ m^2. 84
4.5 Pressure p and pressure margin p_{shear} for shear failure along fault at $t = 0$ s and at $t = 2900$ s. 85

4.6 Shear stress changes within the fault during fault reactivation. 86
4.7 Deformation state around the injection, exaggerated by a factor of 1000. . . . 86
4.8 Difference in displacement $\Delta u_{y'}$ in the y'-direction on the fault with respect to the displacement prior to fault reactivation (left). For failed elements, the slip is calculated from difference between the displacement on the right and on the left side (grey arrows on the left, plot on the right). 87
4.9 Pressure evolution over time for different fault permeabilities. 89
4.10 Pressure and stress evolution over time at the injections cell (coordinates of the cell center: 505, 1475). 89
4.11 Slip after fault reactivation for varying permeabilities. 90

List of Tables

2.1 Conversion of elastic moduli for homogeneous isotropic linear elastic materials. 23

3.1 Material properties of the CO_2-injection scenario. 60
3.2 Instructions fetched by a direct solver (SuperLU) for different discretisations to solve one Newton update for the fully-coupled scheme (FC) and for one iteration of the fixed-stress approach (FS). FS(2p) and FS(el) denote the respective sequential sub-problems for flow and geomechanics. 72

4.1 Material properties of the hydraulic fracturing scenario. 83

Nomenclature

Greek Letters

α	Biot coefficient	[−]
α_{VG}	Van Genuchten parameter	[−]
β	effective stress coefficient for the pore volume	[−]
β_{frict}	angle of internal friction	[−]
ϵ_i	normal strain in i-direction	[−]
$\boldsymbol{\epsilon}$	strain tensor	[−]
γ	interfacial tension	[N/m]
Γ_{ij}	tensoral shear strain in j-direction on surface normal to i-direction	[−]
γ_{ij}	engineering shear strain in j-direction on surface normal to i-direction	[−]
λ	Lamé's first parameter	[Pa]
λ_α	mobility of phase α	$[\mathrm{Pa}^{-1} \cdot \mathrm{s}^{-1}]$
λ_{BC}	Brooks-Corey parameter	[−]
μ	dynamic viscosity	$[\mathrm{kg}/(\mathrm{m} \cdot \mathrm{s})]$
μ_{frict}	friction coefficient	[−]
ν	Poisson's Ratio	[−]
ϕ	porosity	[−]

ϕ_{eff}	effective porosity	[–]
ϱ	density	[kg/m^3]
ϱ_α	phase density	[kg/m^3]
ϱ_{b}	bulk density	[kg/m^3]
ϱ_{rm}	density of the rock matrix	[kg/m^3]
$\boldsymbol{\sigma}$	stress tensor	[Pa]
$\boldsymbol{\sigma}_{\text{eff}}$	effective stress tensor	[Pa]
σ_i	normal stress in i-direction	[Pa]
σ_{m}	mean principal stress	[Pa]
σ_1	maximum principal stress	[Pa]
σ_2	minimum (2D)/intermediate (3D) principal stress	[Pa]
σ_3	minimum principal stress (3D)	[Pa]
σ_{v}	volumetric stress	[Pa]
τ_{ij}	shear stress in j-direction normal to the i-direction	[Pa]
θ	contact angle	[–]

Roman Letters

E	Young's modulus	[Pa]
G	Shear modulus	[Pa]
g	(scalar) gravitational acceleration	[m/s^2]
$\mathbf{g}$	vector of gravitational acceleration $(0,\ 0\ {-g})^{\text{T}}$	[m/s^2]
$\mathbf{K}$	intrinsic permeability	[m^2]

$\mathbf{k}$	(scalar) intrinsic permeability	$[\mathrm{m}^2]$
$\mathbf{K}_{\mathrm{eff}}$	effective permeability	$[\mathrm{m}^2]$
$\mathbf{k}_{\mathrm{eff}}$	(scalar) effective permeability	$[\mathrm{m}^2]$
$\mathbf{K}_{\mathrm{f}}$	hydraulic conductivity	$[\mathrm{m/s}]$
$k_{\mathrm{r}\alpha}$	relative permeability of phase α	$[-]$
K	Bulk modulus	[Pa]
K_{dr}	Drained bulk modulus	[Pa]
K_{f}	Bulk modulus of the fluid	[Pa]
K_{p}	Bulk modulus of the pore space	[Pa]
K_{s}	Bulk modulus of the solid	[Pa]
K_{u}	Undrained bulk modulus	[Pa]
m_{VG}	Van Genuchten parameter	$[-]$
n_{VG}	Van Genuchten parameter	$[-]$
p	pressure	[Pa]
p_α	pressure of phase α	[Pa]
p_{c}	capillary pressure	[Pa]
p_{e}	entry pressure	[Pa]
p_{eff}	effective pressure	[Pa]
q	specific discharge	$[\mathrm{m/s}]$
q_α	source/sink for phase α	$[\mathrm{kg}/(\mathrm{m}^3 \cdot \mathrm{s})]$
Re	Reynolds number	$[-]$

S_α	saturation of phase α	[–]
S_e	effective saturation	[–]
$S_{\mathrm{r}\alpha}$	residual saturation of phase α	[–]
$\boldsymbol{u}$	solid displacement	[m]
$\boldsymbol{v}$	velocity	[m/s]
V_b	bulk volume	[m^3]
$\boldsymbol{v}_\mathrm{D}$	Darcy velocity	[m/s]
$\boldsymbol{v}_{\mathbf{D},\,\boldsymbol{\alpha}}$	Darcy velocity of phase α	[m/s]
V_p	pore volume	[m^3]

Subscripts

α	index for the fluid phase: wetting phase (w) or non-wetting phase(n)
c	capillary
dr	drained
eff	effective
n	non-wetting phase
w	wetting phase
u	undrained

Superscripts

n	coupling step index
k	Newton iteration index
n	time-step index

Abstract

The current world's energy consumption relies heavily on the utilisation of the Earth's subsurface. Coal, oil and natural gas together account for 81-85% of the world's primary energy consumption in 2017 (IEA, 2018; BP, 2018). Often the extraction of these raw materials requires fluid injections into the subsurface, be it in the context of the production of shale gas through hydraulic fracturing or in form of the disposal of waste-water from conventional and unconventional oil and gas production. Furthermore, geothermal power generation or the storage of carbon dioxide also involve the injection of fluids. Such injections have an effect on the pressure field of the fluids present in the subsurface as well as on the stress and the deformation of the reservoir rocks. Examples where this could become a critical issue are when earthquakes are induced or when deformation compromises the integrity of sealing layers. Thus, it is important to understand the interaction of the hydraulic and geomechanical processes.

Numerical simulations are a powerful tool for this purpose but require to choose an appropriate modelling approach. This work addresses the issue by comparing different approaches to model coupled fluid flow and geomechanics. This is far from being trivial since sophisticated mathematical methods compete with pragmatic approaches optimized for practicability. In addition, a new volume-based approach for modelling the reactivation of faults and the resulting earthquakes is presented.

Modelling flow and geomechanics in porous media When modelling coupled flow and geomechanics, one is faced with the decision whether the balance equations are solved simultaneously (referred to as *fully-coupled*) or one after another in a *sequential* scheme. The accuracy and stability of the fully-coupled approach are set against its computational cost, which becomes crucial when application-based scenarios of high complexity and large spatial and temporal scales ought to be simulated. Solving the coupled equations for flow and geomechanics separately could be computationally beneficial, but poses the challenge in what way the equations are split up and which information has to be transferred between them. In addition, the question arises whether solving the equations for flow and geomechanics just once is sufficient or whether one needs to repeat the process several times, resulting in an iterative

scheme. These considerations set the scope of the provided analysis: A fully-coupled approach, a simple sequential scheme and a sophisticated iterative sequential scheme (realised using the fixed-stress split) are compared with respect to accuracy and efficiency. All approaches were implemented within the open-source simulator DuMu^{x}.
The comparison for different numerical test cases reveals that several iterations are needed for the sequential scheme to match the accuracy of the fully-coupled approach. Not iterating causes deviations that are especially prominent when transient effects dominate the simulation. Beside this, confidence in the achieved results was raised since the ones calculated with the non-iterative sequential scheme in DuMu^{x} matched the ones obtained by the sequential TOUGH-FLAC software package. In addition, an analysis of the computational effort needed to solve the linear system of equations for the sequential and the fully-coupled scheme was performed. It allows the conclusion that the advantage of solving two smaller systems of equations for the sequential scheme is used up by the need to perform several iterations to achieve a similar accuracy as the fully-coupled approach. Thus, the fully-coupled scheme is the preferable choice if one intends to achieve the most accurate results. Relative to fully-coupled approach, a sequential scheme can offer more efficiency for the price of accuracy.

Fault reactivation The interaction of raised pressures and a changed stress field can lead to shear failure on a fault and, as a consequence, to earthquakes. Whether shear failure happens is evaluated in this work using the Mohr Circle and the Mohr–Coulomb failure criterion. While this process is fairly undisputed, different representations of the fault (e.g. by phase-field models, discrete surfaces or finite-thickness elements) and the physics during a seismic event (e.g. a friction coefficient dependent or independent of the slip rate) compete with each other. The complex structure of a fault zone is represented by finite-thickness elements here since this captures the mechanical behaviour accurately, offers a broad applicability and fits well into the existing implementation. Based on the conception that during an earthquake previously accumulated seismic energy is released, we propose to model a seismic event by a characteristic drop in shear stress on the fault. The volume-based stress-drop approach produces consistent and plausible results, is applicable to field-scale scenarios and capable of capturing effects observed in reality. The most interesting finding with respect to the processes that lead to fault reactivation is that a higher permeability of the fault zone could possibly result in a larger earthquake.

Zusammenfassung

Der gegenwärtige weltweite Energieverbrauch ist auf eine Nutzung des Untergrunds der Erde angewiesen: Kohle, Öl und Gas machten im Jahr 2017 zusammen 81-85% des weltweiten Energieverbrauchs aus (IEA, 2018; BP, 2018). Häufig erfordert die Förderung dieser Rohstoffe die Injektion von Fluiden in den Untergrund, sei es im Zusammenhang von Schiefergasförderung mittels Hydraulic Fracturing oder wenn bei konventioneller wie unkonventioneller Öl- und Gasfördung anfallendene Abwässer im Untergrund entsorgt werden. Des Weiteren spielen Fluidinjektionen auch bei der Stromerzeugung aus Erdwärme und bei der Speicherung von Kohlenstoffdioxid unter der Erdoberfläche eine Rolle. Solche Injektionen beeinflussen das Druckfeld der im Untergrund befindlichen Fluide genauso wie die Spannung und Verformungen der Reservoirgesteine. Dies kann kritische Ausmaße annehmen, wenn dadurch Erdbeben ausgelöst werden oder wenn die Verformungen die Intaktheit von abdichtenden Gesteinsschichten beeinträchtigen. Ein Verständnis der interagierenden hydraulischen und geomechanischen Prozesse ist daher wichtig.
Numerische Simulationen sind hierfür ein leistungsstarkes Instrument, erfordern aber die Auswahl eines geeigneten Modellansatzes. Diese Arbeit beschäftigt sich mit dieser Problematik, indem verschiedene Ansätze zur gekoppelten Modellierung von Strömung und Geomechanik verglichen werden. Ein solcher Vergleich ist keineswegs trivial, denn hier konkurrieren anspruchsvolle mathematische Methoden mit pragmatischen und auf Anwendbarkeit optimierten Ansätzen. Darüber hinaus präsentiert die Arbeit einen neuen, volumenbasierten Ansatz zur Modellierung der Reaktivierung von Störungen und den sich daraus entwickelnden Erdbeben.

Modellierung von Strömung und Geomechanik in porösen Medien Bei der Modellierung von gekoppelter Strömung und Mechanik muss entschieden werden, ob die zugehörigen Bilanzgleichungen gleichzeitig (*voll-gekoppelt* genannt) oder nacheinander im Rahmen einer *sequentiellen* Vorgehensweise gelöst werden sollen. Der Genauigkeit und Stabilität des vollgekoppelten Ansatzes steht dessen Rechenaufwand gegenüber, was besonders dann entscheidend ist, wenn Szenarien von hoher Komplexität und großem räumlichen und zeitlichen Ausmaß simuliert werden sollen. Die gekoppelten Gleichungen für Strömung und Geomechanik separat

voneinander zu lösen, kann bezogen auf den Rechenaufwand vorteilhaft sein. Die Auftrennung der Gleichungen und die Art der Informationsweitergabe zwischen den Teilen stellt jedoch eine Herausforderung dar. Darüber hinaus ist zu beantworten, inwieweit das einfache Lösen der Gleichungen ausreichend ist oder ob dies mehrfach im Rahmen eines Iterationsverfahrens durchgeführt werden muss. Diese Überlegungen stecken den Rahmen für die vorgestellte Analyse ab: Ein voll-gekoppelter Ansatz, eine einfache sequentielle Vorgehensweise und ein ausgeklügeltes iteratives Verfahren (realisiert mithilfe des *fixed-stress split*) werden bezüglich Genauigkeit und Effizienz verglichen. Alle Ansätze sind dabei in der frei verfügbaren Simulationssoftware DuMu$^{\text{x}}$ implementiert.
Beim Vergleich der verschiedenen numerischen Testfälle wird deutlich, dass im Fall des sequentiellen Verfahrens mehrere Iterationen notwendig sind, um die Genauigkeit des voll-gekoppelten Ansatzes zu erreichen. Ein Nicht-Iterieren führt zu Abweichungen, die besonders auffällig sind, wenn transiente Effekte die Simulationen dominieren. Da die nicht-iterierten Ergebnisse aus DuMu$^{\text{x}}$ und die mithilfe des sequentiellen Softwarepakets TOUGH-FLAC berechneten Resultate miteinander übereinstimmen, konnte das Vertrauen in die erzielten Ergebnisse erhöht werden. Darüber hinaus wurde eine Analyse des Rechenaufwands für das Lösen des linearen Gleichungssystems jeweils für den sequentiellen und den voll-gekoppelten Ansatz durchgeführt. Daraus lässt sich folgende Schlussfolgerung ziehen: Der Vorteil, zwei kleinere Gleichungssysteme statt eines großen zu lösen, wird dadurch zunichte gemacht, dass mehrere sequentielle Iterationen benötigt werden, um die Genauigkeit des voll-gekoppelten Ansatzes zu erreichen. Dementsprechend sollte dem voll-gekoppelten Ansatz der Vorzug gegeben werden, wenn genaue Ergebnisse benötigt werden. Relativ dazu bietet ein sequentielles Verfahren mehr Effizienz zum Preis geringerer Genauigkeit.

Reaktivierung von Störungen Die Interaktion von erhöhten Drücken und einem geänderten Spannungsfeld kann zur Reaktivierung von Störungen und somit auch zu Erdbeben führen. Ob Scherversagen auftritt, wird in dieser Arbeit über den Mohrschen Spannungskreis und das Mohr-Coulombsche Versagenskriterium bestimmt. Während dieser Prozess recht unumstritten ist, konkurrieren unterschiedliche Modellvorstellungen der Störung (zum Beispiel als Phasenfeld, als diskrete Fläche oder als Element mit endlicher Dicke) und der Physik während eines seismischen Ereignisses (zum Beispiel ein von der Versatzgeschwindigkeit unabhängiger oder abhängiger Reibungskoeffizient) miteinander. Die komplexe Struktur einer Störungszone wird über Elemente endlicher Dicke abgebildet, da dies das mechanische Verhalten korrekt beschreibt, eine breite Anwendbarkeit bietet und gut in die bestehende Implementierung passt. Ein Erdbeben kann als Freisetzung zuvor gespeicherter seismischer Energie aufgefasst werden. Entsprechend wird in dieser Arbeit ein seismisches Ereignis als charakteristischer Abfall der Scherspannung in der Störungszone modelliert. Der volumenbasierte Ansatz produziert dabei

konsistente und plausible Ergebnisse, ist auf Szenarien auf der Feldskala anwendbar und kann in der Realität beobachtete Prozesse abbilden. In Bezug auf das Verständnis für die Prozesse, die zur Reaktivierung von Störungen führen, ist die interessanteste Erkenntnis, dass in einer besser durchlässigen Störungszone potentiell stärkere Erdbeben ausgelöst werden können.

1 Introduction

In 2017, the global consumption of energy has increased by 2.1-2.2 %, more than twice the growth rate in 2016 and the fastest since 2013. At the same time, the CO_2 emissions grew by 1.4-1.6% after three years with no or little change from 2014 to 2016 according to the Statistical Review of World Energy by BP and the Global Energy & CO_2 Status Report by the International Energy Agency (IEA) (BP, 2018; IEA, 2018). Global economic growth, lower fossil-fuel prices and weaker energy efficiency efforts contributed to that increase. Both reports also note that 2017 has seen a record high of natural gas consumption with 22-23.4% of the global primary energy consumption.

A key development in this context has been the combination of horizontal drilling and hydraulic fracturing, allowing an economically feasible gas production from very low permeable shale formations. The United States have been the focal point of this *shale gas revolution*. As a consequence, the United States transformed from one of the world's biggest importers of gas into being self-sufficient in less than a decade, with a 12-fold increase in shale gas production from 2000 to 2010 (Wang et al., 2014). Beside the increased portion of renewables-based electricity generation, the switch from burning natural gas instead of coal has considerably contributed to the third consecutive year of decline in CO_2 emissions in the United States (IEA, 2018). Nonetheless, the boom of shale-gas production has also given rise to environmental concerns. Water use and management present challenges for shale-gas production (e.g. Nicot and Scanlon, 2012; Gregory et al., 2011). The potential for drinking and groundwater contamination has been a commonly raised concern, too (e.g. Jackson et al., 2013; Osborn et al., 2011). Shale-gas production has also been made responsible for an increased seismic activity. It is important to distinguish here between earthquakes that occurred in the vicinity of hydraulic fracturing operations (e.g. Holland, 2013; Skoumal et al., 2015) and earthquakes that have been linked to the disposal of fluid waste into deep formations (e.g. Horton, 2012). The latter is a practice not limited to shale gas, but also used in the context of conventional oil and gas production. The most prominent example is the Mw 5.7 earthquake in November 2011 in Oklahoma, which has been linked to waste-water injections from the oil production in the Wilzetta North field (Keranen et al., 2013).

The process of fluid injections altering the stress state in the subsurface has also been a topic of discussion in the context of carbon capture and storage, where one intends to inject

CO_2 instead of emitting it into the atmosphere. For this technology, the question whether the injection could trigger earthquakes, which, even if small, could threaten the integrity of sealing rock formations has been the subject of some controversy (Zoback and Gorelick, 2015; Vilarrasa and Carrera, 2015; Juanes et al., 2012; Zoback and Gorelick, 2012). Furthermore, Verdon et al. (2013) provide a comparison for three large-scale sites, namely the Sleipner, Weyburn, and In Salah field, where CO_2 is injected at rates of $\sim$1 megatonne/year or more. They conclude that increased pore pressures can induce significant deformation (In Salah) and that the pore pressure-deformation interaction can be complex (Weyburn).
It becomes clear that current developments in the world's energy production and consumption are intertwined with technologies where fluid injections into the subsurface play a key role. Be it waste-water disposal, hydraulic fracturing or CO_2 injections, the occurring processes cannot be fully understood if the interaction of fluid flow and geomechanics is left out of consideration. Numerical models can provide valuable contributions in this respect and will be discussed in this thesis. In detail, this work presents volume-based conceptual approaches for the analysis of coupled hydraulic and geomechanical processes.

1.1 Hypotheses

When models are used to represent aspects of the real world, the scientific debate often revolves around the question, which model is better suited or more accurate for the intended purpose. In addition, the mentioned applications can exhibit large temporal and spatial scales as well as complex geometries, so the corresponding simulations become computationally demanding. Thus, a comparison of different model approaches should consider (a) how accurate the relevant physics are represented and (b) how computationally efficient the scheme is as decision criteria. This is also true here, where the question whether the equations for flow and geomechanics are solved simultaneously (referred to as *fully-coupled*) or sequentially is a central issue. The latter poses the challenge of splitting the two coupled equations in a way that they can be solved one after another. To compensate the loss of information regarding the coupling, schemes that iterate the sequential solutions of the equations have been developed.
During an earthquake, previously built-up stress is released. The difference in stress before and after the earthquake is referred to as the *stress drop*. For the process of this release, the question for an appropriate conceptual model arises again.
These two questions inspire the two hypotheses which will be tested in this work:

Hypothesis 1 *If one aims to perform efficient simulations of coupled flow and geomechanics without sacrificing accuracy, the balance equations should be solved in a fully-coupled way.*

This requires to test approaches on the efficient and rather pragmatic end of the spectrum as well as mathematically sophisticated alternatives to the fully-coupled approach.

Hypothesis 2 *The process of fault reactivation can be represented in a meaningful way by the stress drop as the characteristic parameter.*

Where such an approach is situated relative to existing approaches provides first insight into whether it is justified. The hypothesis will be further tested by applying the implementation to a set of numerical scenarios.

1.2 Structure of the thesis

The motivation and two hypotheses were outlined in this chapter. The second chapter will present the fundamental physical definitions and concepts. First, it will cover fluid flow in porous media and continue with a section on rock mechanics. The last section of the chapter will bring both together by introducing the theory of poroelasticity. The third chapter will focus on modelling flow and geomechanics in porous media. The mathematical equations, the numerical models and the solution strategies will be explained. A set of numerical test cases allows to compare the different approaches. The forth chapter contains a new proposed modelling concept for fault reactivation and numerical test cases illustrating its capabilities. The fifth chapter will give a summary and an outlook beyond the scope of this thesis.

2 Fundamentals

2.1 Fluid flow through porous media

2.1.1 The porous medium

The applications covered in this work involve the injection of fluids into rock formations. The material of these rock formations comprises not only the rock itself, but also the voids within the rock. The rock itself, in turn, is made up of smaller pieces called rock grains. They form a skeleton around the voids and are referred to as the *matrix* while the voids are called *pores*. Both taken together are a *porous medium*. The pores can vary greatly in size and thus, they are subdivided into *macro-pores* (>50 nm), *meso-pores* (2–50 nm), and *micro-pores* (<2 nm) (Rouquerol et al., 1994).

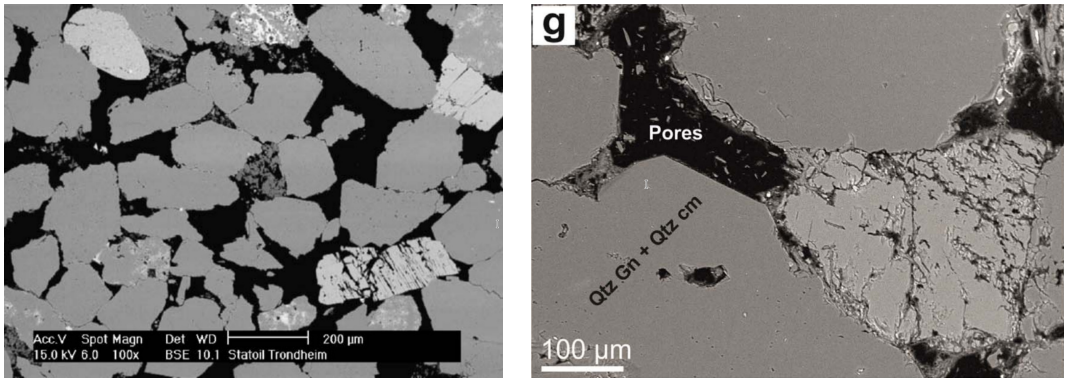

(a) Back-scattered electron image of a thin section from a Berea Sandstone sample. The grains are composed of feldspar (light grey), quartz (medium grey), and clays (dark grey). The pore space is black.
Reprinted from Øren and Bakke (2003), Copyright ©2003, with permission from Elsevier.

(b) Image of a thin section from a Berea Sandstone obtained with cathode luminescence scanning electron microscopy. Quartz grains and cement (Qtz Gn, Qtz cm) are shown again in medium grey, feldspar in light grey and the pores in black.
Reprinted from Kareem et al. (2017), Copyright ©2017, with permission from Elsevier.

Figure 2.1: Images of a Berea Sandstone sample obtained with different techniques.

A typical example for a porous medium is sandstone. The Berea Sandstone has become the standard sandstone used by the petroleum industry due to its relatively uniform physical properties. It contains mainly quartz, but also minor amounts of clay and feldspar (Lesmes and Frye, 2001; Churcher et al., 1991). Images of thin sections from Berea Sandstones samples are shown in Figure 2.1a and 2.1b.
The Barnett Shale, which is United States' oldest shale gas play (Patzek et al., 2013) and was the country's leading shale gas producer for a decade until 2011 (EIA, 2001), can also be described as a porous medium. But when compared to the Berea Sandstone, the field emission scanning electron microscope (FE-SEM) images in Figure 2.2a and 2.2b illustrate that the scale of the Barnett's structures is very different: While pores and rock grains in case of the Berea Sandstone are in the order of few hundreds to several tens of microns, long fibrous aggregates of clay and residual kerogen of the Barnett form macro- and meso-pores ranging from a few hundred down to a few nanometres.

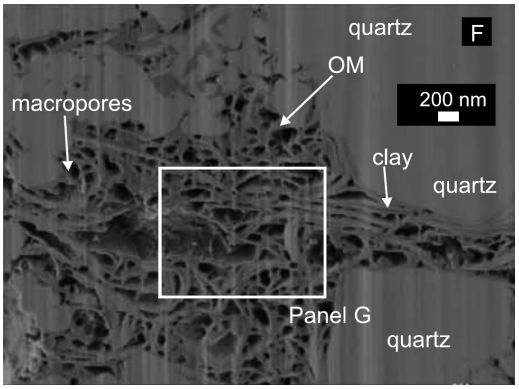

(a) FE-SEM image of a Barnett sample. Macropores are found within kerogen and clay aggregates. OM = organic matter. Close-up of Panel G in Fig. 2.2b.
Taken from Chalmers et al. (2012), Fig. 11 F. Copyright ©2012. The American Association of Petroleum Geologists (AAPG). Reprinted by permission of the AAPG whose permission is required for further use.

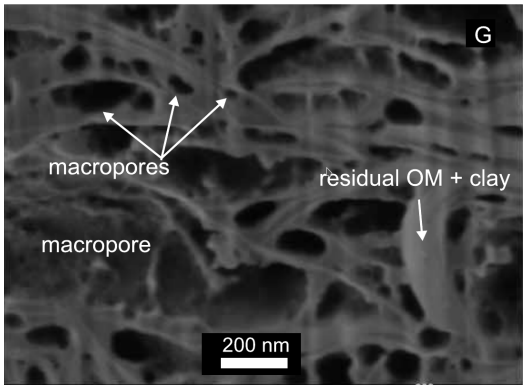

(b) Close-up of the long fibrous aggregates of clay and residual kerogen in Fig. 2.2a, which form a network of macro-pores. OM = organic matter.
Taken from Chalmers et al. (2012), Fig. 11 G. Copyright ©2012. The American Association of Petroleum Geologists (AAPG). Reprinted by permission of the AAPG whose permission is required for further use.

Figure 2.2: Structure of a Barnett Shale sample on different spatial scales.

2.1.2 Scales

The observation of significant differences between the two examples of a porous medium leads to the subject of this section: The scale of the processes that ought to be described is important. The following definitions and concepts have been outlined by several authors

(e.g. Bear, 1988; Helmig, 1997) and will be summarized here to lay the ground for all further derivations.

It might be tempting to model the collision of individual molecules and the surrounding walls by classical mechanics, but the large amount of molecules required to model a meaningful volume of fluid (assuming a mass of 18.02 u per water molecule and that 1 mL weighs 1 g, 1 mL water would contain $3.343 \cdot 10^{22}$ water molecules) renders such an approach on the molecular level not feasible for the modelling of flow and transport.

By taking information about molecular properties and interactions such as the molecular mass or dipole moments into account and by transferring them into properties averaged for a large number of molecules, one can treat matter as continua and neglect the actual molecular structure. It is important to choose the number of molecules (or the volume, respectively) over which is averaged large enough to exclude molecular effects but also small enough to capture the relevant processes. Bear (1988) calls such an ensemble of many molecules *particle* and, in order to distinguish this approach from a consideration on a molecular level, Bear (1988) introduced the term *microscopic level*.

The work of Bousige et al. (2016) is an example of how the transfer from the molecular to the microscopic level for materials such as the kerogen fibers in Figure 2.2b with only a few nanometres of thickness can be tackled: By using advanced molecular reconstruction methods and statistical mechanics molecular modelling, they are able to gain insight into the nanostructure of kerogen, which is a first step towards determining the transport and mechanical properties of a shale on a microscopic level.

On the microscopic level, we can now consider fluid and solid as continua and model the flow of the fluid through the pores. But when looking at the Berea and Barnett samples, it becomes apparent that this would only work for simple examples, but not for realistic cases as geometries of the pores are too difficult to describe. This leads to an even coarser continuum approach on a *macroscopic level* (Bear, 1988). This time we need to find a *representative elementary volume* (REV) for our porous medium that encompasses enough pores so the average gives a meaningful value but at the same time is small enough to represent the relevant processes. Figure 2.3 illustrates this dependency: We define the portion, which the volume of the pore space V_{pores} takes up within the total volume V_{tot} as the ratio $r_{\text{pores}} = V_{\text{pores}}/V_{\text{tot}}$. For $V_{\text{pores}} \to 0$, r_{pores} becomes 0 for a point within the matrix and 1 for a point within a pore. For small values of V_{tot}, r_{pores} will vary greatly, but the oscillations become less pronounced with increasing values of V_{tot}. After surpassing a certain threshold value V_0, r_{pores} can be considered as constant and V_0 as an REV. For values greater than V_0, we can switch from microscopic to macroscopic parameters.

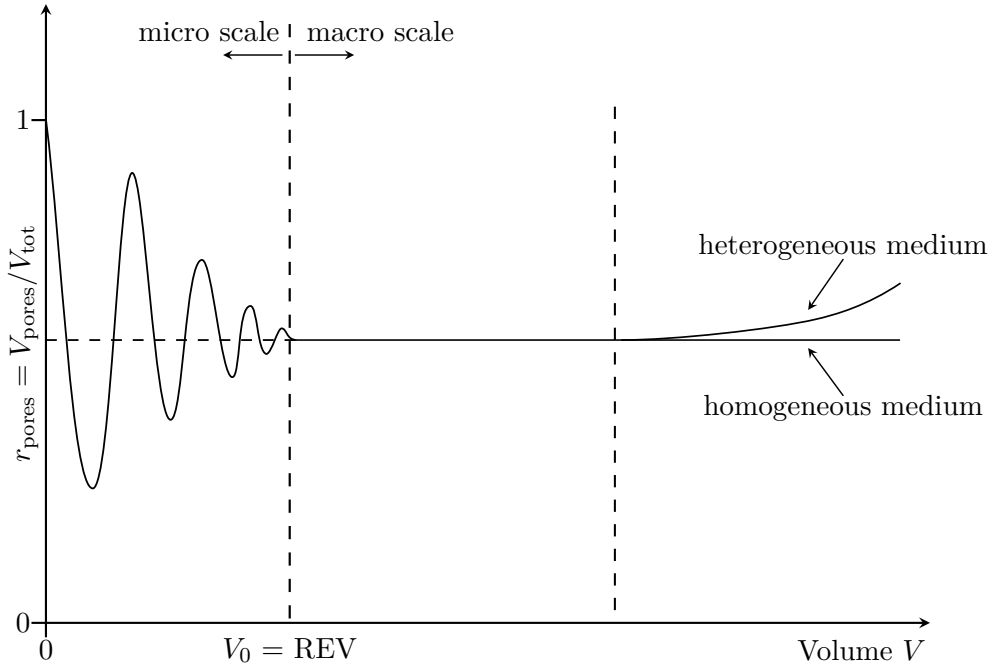

Figure 2.3: Definition of a representative elementary volume (REV) after Bear (1988); Class (2001).

2.1.3 Porosity

The porosity ϕ describes the previously introduced ratio between the pore volume and the total volume on the REV scale:

$$\phi = \frac{V_{\text{pores,REV}}}{V_{\text{tot,REV}}}. \tag{2.1}$$

Figure 2.4 illustrates the microscopic and macroscopic perspective for the Berea Sandstone sample shown in Figure 2.1a: When viewed from a microscopic perspective, one would resolve all mineral grains and pores of the Berea Sandstone as shown in Figure 2.4a. On a macroscopic level, we treat the whole volume as an REV and use a porosity value averaged over this volume to describe which portion of the volume is made up by pores.
The concept is not universally applicable for volumes greater than V_0: If heterogeneities are present, the porosity value can change for increasing volumes (see also Figure 2.3).

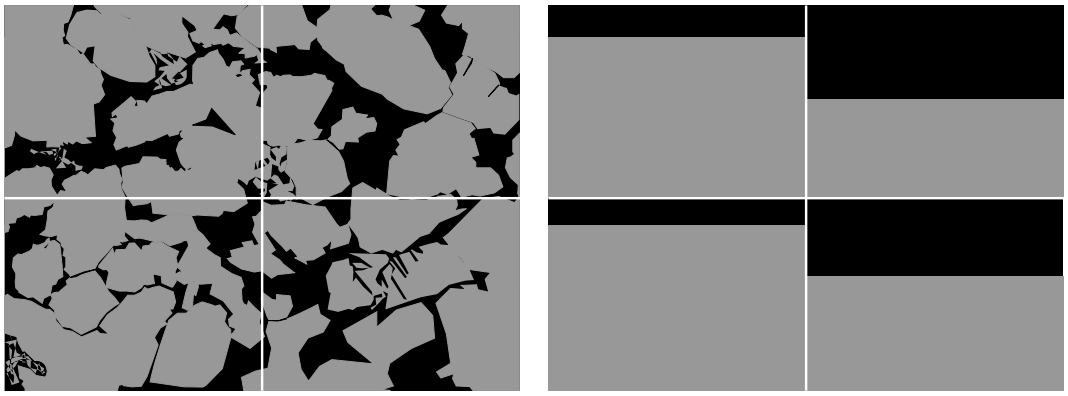

(a) Schematic microscopic structure of the Berea Sandstone sample from Figure 2.1a. All minerals are lumped together as the matrix, which is coloured grey. The pores displayed in black. The picture is split into four partitions.

(b) Averaged structure of the Berea Sandstone sample on the macro scale. Four representative elementary volumes (REVs) are defined, where pores (black) and matrix (grey) can be considered as volume fraction of the total volume.

Figure 2.4: Example for the transfer from the micro-scale to the macro-scale.

2.1.4 Phases

The matrix and the pore space can be further subdivided into different phases. One distinguishes between solid, liquid and gaseous phases. Phases form distinct interfaces, where discontinuities in their otherwise uniform chemical and physical properties occur. Thus, only one gaseous phase, but several liquid and solid phases can be present within our porous medium. But a certain degree of ambiguity exists: Depending on the spatial resolution and the considered processes, a material can be divided into a different number of phases. For instance, the matrix can be treated as one phase for the flow of fluids through the Berea Sandstone sample, but if chemical processes are taken into account, this could necessitate a distinction between the different minerals of the matrix. For mechanical deformation, in turn, the relevant properties could be similar or at least treated as such on the REV-scale.

2.1.5 Saturation

Similar to the concept of the porosity, we define the volume fraction of the pore space occupied by a fluid phase α within the REV as the saturation S_α:

$$S_\alpha = \frac{V_\alpha}{V_{\text{pores,REV}}}. \tag{2.2}$$

The sum of the saturations of all fluid phases present within an REV must equal 1:

$$\sum_{\alpha} S_{\alpha} = 1. \tag{2.3}$$

2.1.6 Permeability

For moving fluids, the ability of the porous medium to let these fluids pass through its pores is decisive. The parameter describing this property is the permeability $\mathbf{K}$. The porosity as a measure for the pore volume influences the permeability, as well as the size, shape and connectivity of the pores. How well a fluid moves through the porous medium also depends on the fluid's properties. To emphasise that the $\mathbf{K}$ is a characteristic property of the porous medium and only describes its contribution, we will refer to it as the *intrinsic permeability*. In contrast, the *hydraulic conductivity* $\mathbf{K}_{\mathrm{f}}$ also contains the fluid's contribution, namely the density ϱ and the dynamic viscosity μ of the fluid, and the acceleration due to gravity g:

$$\mathbf{K_f} = \mathbf{K}\frac{\varrho\, g}{\mu}. \tag{2.4}$$

The connectivity and the pore shape can vary with the spatial direction, thus $\mathbf{K}$ and $\mathbf{K}_{\mathrm{f}}$ are defined as tensors.

2.1.7 Capillary pressure

At the interface of two immiscible fluids in a pore throat a pressure difference is observable. This *capillary pressure* p_c results from the different tendency of the fluids to cling to the solid phase: If adhesive forces outweigh the cohesive forces, the fluid will tend to spread on the surface of the solid. The fluid is then termed the wetting phase. If, vice versa, the cohesive forces are greater than the adhesive forces, the fluid will tend to form drops and is thus called the non-wetting phase. The capillary pressure p_{c} is then defined as the difference between the pressure of the non-wetting phase p_{n} and the wetting phase p_{w}:

$$p_{\mathrm{c}} = p_{\mathrm{n}} - p_{\mathrm{w}}. \tag{2.5}$$

On the REV-Scale, the dependency on the micro-scale forces has to be replaced by an REV-scale quantity. Commonly, such formulations use the previously introduced saturation, such as the one by Brooks and Corey (1964):

$$p_{\mathrm{c}} = p_{\mathrm{e}} \left(\frac{S_{\mathrm{w}} - S_{\mathrm{rw}}}{1 - S_{\mathrm{rw}}} \right)^{-1/\lambda_{\mathrm{BC}}}. \tag{2.6}$$

Here, p_e is the entry pressure, which represents the pressure the non-wetting phase has to overcome to enter an REV fully saturated with the wetting phase. S_{rw} and S_{rn} are the residual saturations of the wetting and non-wetting phase. The parameter λ_{BC} is related to the grain-size distribution and used to fit the curve to experimental data. The term containing the phase saturations can be condensed into the *effective saturation* S_e:

$$S_e = \frac{S_w - S_{rw}}{1 - S_{rw}} \tag{2.7}$$

Another common formulation is the one by Van Genuchten (1980), which uses α, n and m instead of α_{VG}, m_{VG} and n_{VG}:

$$p_c = \frac{1}{\alpha_{VG}} \left(S_e^{-1/m_{VG}} - 1 \right).^{1/n_{VG}} \tag{2.8}$$

The parameters α_{VG}, m_{VG} and n_{VG} are again used to fit the curves to experimental data. Relations to transfer them into their respective Brooks-Corey counterparts exist (e.g. Lenhard et al., 1989). Conceptionally, the Van-Genuchten-relation converges to a capillary pressure value $p_c = 0$ for $S_w \to 1$. This makes it smoother and more continuous in comparison to the Brooks-Corey relation, but at the expense of a representation of the entry pressure.
Krevor et al. (2012) used mercury injection capillary pressure (MICP) measurements to derive the p_c - S_w relationship in a Berea Sandstone sample. The experimental capillary pressure $p_{c,\,Hg/air}$ obtained for the mercury/air system was converted to the corresponding capillary pressure $p_{c,\,CO_2/water}$ in a CO_2/water system using

$$\frac{p_{c,\,CO_2/water}}{p_{c,\,Hg/air}} = \frac{\gamma_{CO_2/water} \cos \theta_{CO_2/water}}{\gamma_{Hg/air} \cos \theta_{Hg/air}} \tag{2.9}$$

with γ as the interfacial tension and θ as the contact angle measured in the wetting fluid. Krevor et al. (2012) assumed $\gamma_{CO_2/water} = 32$ mN m^{-1} and $\gamma_{Hg/air} = 485$ mN m^{-1} and that the contact angles are equal.
Afterwards, they fitted the parameters of Equation 2.6 to the experimental data. Both the experimental data and the fitted Brooks-Corey curve are shown in Figure 2.5 in grey. The course of the curve becomes clear, if one visualises how such an experiment would be realized: Starting with a sandstone sample fully saturated with water as the wetting phase, one would try to gradually replace the wetting phase by the non-wetting phase. For this, the non-wetting pressure needs to be raised relative to the wetting pressure or, in other words, an increase in capillary pressure is required. Up to certain point, no wetting fluid would enter the pores, but if the entry pressure is surpassed, the non-wetting phase will replace some of the wetting phase, so S_w is becomes smaller than 1. This interplay of a decreasing wetting saturation with a rising capillary pressure continues until a lower limit for S_w is reached, where an increase in

p_c causes no change in S_w. This remaining wetting-phase saturation is then equivalent to the residual saturation of the wetting phase S_{rw}.

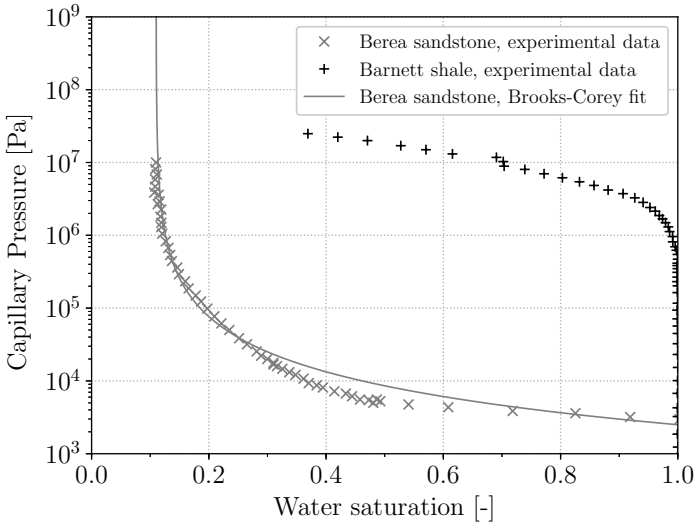

Figure 2.5: Capillary pressure-saturation relationship for a Barnett Shale sample from Moghaddam and Jamiolahmady (2016) and for a Berea Sandstone sample from Krevor et al. (2012). For the Berea Sandstone sample, Krevor et al. (2012) also provide a fit of Equation 2.6 to the experimental data: $p_e = 2.5$ kPa, $S_{rw} = 0.11$, $S_{rn} = 0.0$ and $\lambda_{BC} = 0.67$.

The black data points are taken from Moghaddam and Jamiolahmady (2016) for a Barnett Shale sample. The experimental data was also obtained with MICP and afterwards converted with the method by Krevor et al. (2012) described above. Compared to the data obtained for Berea Sandstone, a significantly higher capillary pressure is required to replace the non-wetting fluid. The differences in the pore structure of the two rocks described previously provide an explanation for the varying behaviour.

2.1.8 Relative permeability

The presence of other phases within the pores creates an additional resistance for the flow of each phase, as in comparison to a case where only one phase is present, less pore space is available for flow. This is taken into account by defining a dimensionless *relative permeability* term $k_{r\alpha}$ of a phase α, which multiplied with the intrinsic permeability $\mathbf{K}$ results in the phase permeability $\mathbf{K}_\alpha$. Brooks and Corey (1964) provide one of the most commonly used

formulations, where the relative permeability is a function of the phase saturations:

$$k_{\mathrm{rw}} = S_{\mathrm{e}}^{\frac{2+3\lambda_{\mathrm{BC}}}{\lambda_{\mathrm{BC}}}}, \tag{2.10}$$

$$k_{\mathrm{rn}} = (1 - S_{\mathrm{e}})^2 \left(1 - S_{\mathrm{e}}^{\frac{2+\lambda_{\mathrm{BC}}}{\lambda_{\mathrm{BC}}}}\right). \tag{2.11}$$

In Figure 2.5, examples for relative permeability curves are shown. On the left, experimental data for CO_2 (grey) and water (black) in a Berea Sandstone sample are displayed, while the data on the right was obtained for CH_4 (grey) and water (black) in a Barnett Shale sample.

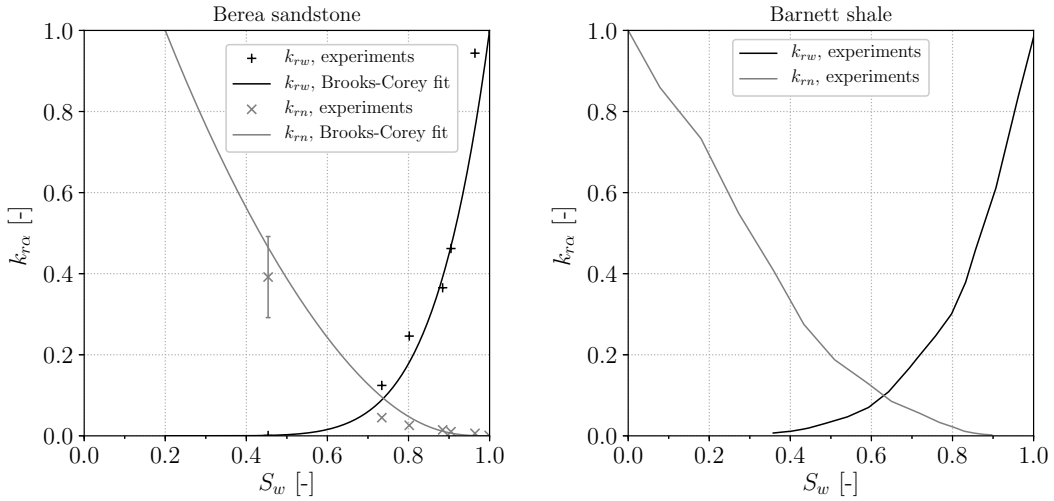

(a) Relative permeability for CO_2 (grey) and water (black) in a Berea Sandstone sample, data obtained by Krevor et al. (2012).

(b) Relative permeability for CH_4 (grey) and water (black) in Barnett Shale sample, data obtained by Penny et al. (2006).

Figure 2.5: Examples for relative permeability curves.

Corresponding to the Van-Genuchten formulation of the capillary pressure-saturation relationship by van Genuchten (1980), the relative permeability can be alternatively calculated with

$$k_{\mathrm{rw}} = \sqrt{S_{\mathrm{e}}} \left(1 - \left(1 - S_{\mathrm{e}}^{1/m}\right)^m\right)^2, \tag{2.12}$$

$$k_{\mathrm{rn}} = (1 - S_{\mathrm{e}})^{1/3} \left(1 - S_{\mathrm{e}}^{1/m}\right)^{2m} \tag{2.13}$$

2.1.9 Advection

If fluids are injected into the subsurface, fluxes driven by pressure gradients and gravitation will occur. Such fluxes are called *advective fluxes*. Based on experiments, the French engineer Henry Darcy formulated the following relationship for a flux $\boldsymbol{q}$ through a porous medium:

$$\boldsymbol{q} = -\frac{\mathbf{K}}{\mu} \cdot \operatorname{grad} p. \tag{2.14}$$

In honour of its spiritual father, this relationship is today called Darcy's Law. It expresses that a fluid will flow from a location with a higher pressure to one with a lower pressure, in opposite direction of the pressure gradient $\operatorname{grad} p$, hence the negative sign. The flux $\boldsymbol{q}$ can be calculated from the discharge per area and thus represents a specific discharge. As it has the unit of a velocity, it is often referred to as the Darcy velocity $\boldsymbol{v}_{\mathrm{D}}$. Nonetheless, for the velocity $\boldsymbol{v}$ within the pores, one has to divide q, or $\boldsymbol{v}_{\mathrm{D}}$, respectively, by the porosity ϕ to account for the fact that the fluid only passes through the cross-sectional area of the pores and not through the total cross-sectional area:

$$\boldsymbol{v} = \frac{\boldsymbol{v}_{\mathrm{D}}}{\phi} = \frac{\boldsymbol{q}}{\phi} \tag{2.15}$$

Darcy's Law has been extended to multi-phase flow (e.g. Helmig, 1997). The Darcy velocity $\boldsymbol{v}_{D,\,\alpha}$ of a phase α is then expressed as

$$\boldsymbol{v}_{\mathrm{D},\,\alpha} = -\frac{k_{\mathrm{r}\alpha}}{\mu_\alpha} \mathbf{K} \left(\operatorname{grad} p_\alpha - \varrho_\alpha \boldsymbol{g}\right) \tag{2.16}$$

with ϱ_α as the density, μ_α the dynamic viscosity of a phase α and $\mathbf{g}$ as the gravity vector. As outlined in Subsection 2.1.8, the intrinsic permeability is scaled with the relative permeability $k_{\mathrm{r}\alpha}$. The term $\frac{k_{\mathrm{r}\alpha}}{\mu_\alpha}$ is often referred to as the *mobility* λ_α of a phase α.
Whether Darcy's law is applicable can be checked with the Reynolds number. This dimensionless quantity describes the ratio of inertial forces to viscous forces. It is calculated from the characteristic length L, the velocity v, the dynamic viscosity μ_α and the fluid's density ϱ. In case of a porous medium, for L a characteristic pore diameter d is chosen, and $\boldsymbol{v}_D$ is used for the velocity:

$$Re = \frac{d\, v_{\mathrm{D}}\, \varrho}{\mu} \tag{2.17}$$

Bear (1988) reports that Darcy's law is a valid assumption for Reynolds numbers between 1 and 10.

2.2 Rock mechanics

Injecting fluids into geologic formations will not only result in advective fluxes, but also induce mechanical deformation of the rocks. Thus, this section will cover the fundamentals of rock mechanics.

2.2.1 Rock classification

Rocks are typically defined as naturally occurring aggregates of minerals. Minerals, in turn, are characterised by their solid crystalline structure, have a specific chemical composition and occur in nature (Grotzinger and Jordan, 2010; Skinner and Porter, 2000). Furthermore, a mineral is usually defined as being inorganic (Grotzinger and Jordan, 2010). Rocks sometimes contain non-crystalline glassy materials, such as obsidian or pumice, and organic matter, such as kerogen in coal and oil shales.
Rocks can form in different geologic environments and by different geologic processes. Thus, rocks are divided into different groups: When molten rock solidifies, the resulting rocks are called *igneous*. Depending on whether these rocks crystallise in the Earth's crust slowly, or are erupted at the Earth's surface and cool quickly, one distinguishes between *intrusive* and *extrusive* igneous rocks. More time allows the crystals to grow larger, which allows to distinguish intrusive and extrusive igneous rocks by the size of their minerals. A typical intrusive igneous rock is granite, while basalt is probably the best known extrusive igneous rock.
The Berea Sandstone and the Barnett Shale described in Section 2.1 belong to a different group: The *sedimentary rocks*. As these rocks are the most relevant rock types for the applications in this work, their genesis will be described in more detail: Sedimentary rocks are a result of loose particles like sand grains, mud or calcareous shells of marine organisms being deposited. These building materials of sedimentary rocks are called *sediments*. They can form when chemical and physical processes degrade existing rocks (so-called *weathering*) and are then transported by wind, rivers, glaciers, ocean currents etc. (commonly known as *erosion*). Derived from the greek word *klastos* meaning "broken", these sediments are referred to as *clastic sediments* (Grotzinger and Jordan, 2010; Skinner and Porter, 2000). But sediments can also form in other ways, for instance when marine organisms precipitate calcite or when evaporation causes halite precipitation from seawater. Accordingly, one calls these sediments *biological* and *chemical sediments*.
Sediments become sedimentary rocks in two ways (Grotzinger and Jordan, 2010; Skinner and Porter, 2000): Continued deposition can bury older sediments, which causes a decrease in volume, porosity and water content as the particles are squeezed closer together due to the

increased lithostatic pressure. Moreover, precipitation of minerals from groundwater can bind the particles together and decrease the porosity, too, which is referred to as *cementation*. These hardening processes convert sediments like mud and sand into shales and sandstone and are summarized under the term *lithification* (Grotzinger and Jordan, 2010). The characteristics of lithification matter for the rock's mechanical response: For instance, Chang et al. (2006) list several empirical relationships between the rock's strength and its porosity. Regarding cementation, Dyke and Dobereiner (1991) report that that silica holding the grains together enhances the rock's strength while clay is considered a rather weak cement.
The third rock group are *metamorphic rocks*, which are formed deep within the Earth. Under the influence of high pressures and temperatures, sedimentary, igneous or other metamorphic rocks experience changes in mineralogy, texture or chemical composition, but maintain their solid form (Grotzinger and Jordan, 2010). As an example, a shale can become a shist or a gneiss.
All three rock types can evolve from one another, thus the term rock cycle is commonly used: As an example, this cycle could start with sediments being deposited in a basin or an ocean. Buried under subsequent layers of sediment, lithification turns them into sedimentary rocks. Under the influence of tectonic plate collisions, these sediments could experience higher pressures and temperatures and become metamorphised. Even higher temperatures and pressures would cause melting, and the resulting magma would be the source material for new igneous rocks. If these rocks are uplifted and exposed to weathering and erosion, new sediments form and the cycle is completed. Obviously, this is just one possible variant of the cycle and many more exist. Furthermore, not all stages have to be completed. For instance, metamorphic rocks could become exposed and weathered without being melted first or sedimentary rocks could be eroded without being turned into other rocks.

2.2.2 Definition of stress

The characterisation of a rock's mechanical behaviour is inconceivable without the physical quantity *stress*. Thus, the definition of stress will be covered in the following using the notation of Jaeger and Cook (1976). For the description of the internal forces acting at a point O inside a body, an arbitrarily chosen, small cross-sectional area δA and a direction $\overrightarrow{\mathrm{OP}}$ orthogonal to this area is assumed (see Figure 2.6, left).
The internal forces acting on the area δA within the body are equivalent to a force $\delta\mathbf{F}$ exerted by the material above this area onto the material below this area (or an equal force in the opposite direction exerted by the material below onto the material above). The stress vector $\boldsymbol{t}_{\overrightarrow{\mathrm{OP}}}$ at point O and with respect to the plane orthogonal to the direction OP is defined as the

limit of the ratio $\delta\mathbf{F}/\delta A$:

$$\boldsymbol{t}_{\overrightarrow{\mathrm{OP}}} = \lim_{\delta A \to 0} \frac{\delta \mathbf{F}}{\delta A} \tag{2.18}$$

When a right-handed Cartesian coordinate system is placed at O so that $\overrightarrow{\mathrm{OP}}$ is oriented in direction of the x-axis, one can distinguish between the components of the stress vector $\boldsymbol{t}_{\mathrm{O}x}$ in x-, y- and z-direction (see Figure 2.6, right). In this case, the component in x-direction, which is perpendicular to δA, will be denoted as the normal stress σ_x, while the components in the plane of the area δA are written as τ_{xy} and τ_{xz}. They are called shear stresses, accounting for the fact that, as Jaeger and Cook (1976) explain, they tend to shear or slide the material in the plane δA.

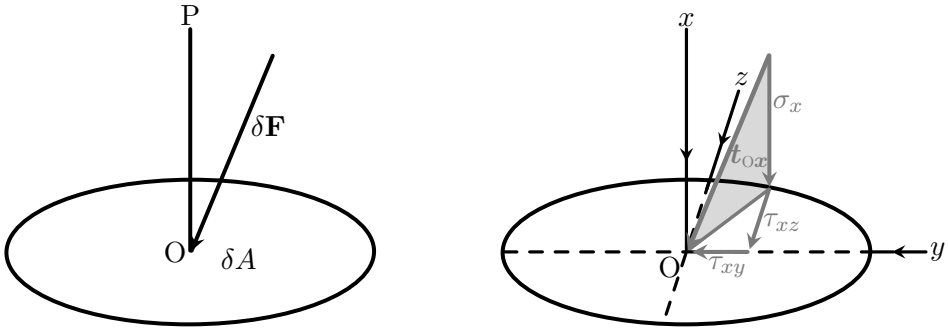

Figure 2.6: Stress definition, after Jaeger and Cook (1976). Illustration of stress as the ratio between the force $\delta\mathbf{F}$ and the area δA on the left and the decomposition into normal and shear components with respect to a coordinate system on the right.

In the same fashion, the stress vectors $\boldsymbol{t}_{\mathrm{O}y}$ and $\boldsymbol{t}_{\mathrm{O}z}$ can be set up with OP oriented in direction of and δA perpendicular to the y- and z-axis, which gives their components τ_{yx}, σ_y and τ_{yz} and τ_{zx}, τ_{zy} and σ_z, respectively. Together, these nine components make up the stress tensor $\boldsymbol{\sigma}$:

$$\boldsymbol{\sigma} = \begin{pmatrix} \sigma_x & \tau_{xy} & \tau_{xz} \\ \tau_{yx} & \sigma_y & \tau_{yz} \\ \tau_{zx} & \tau_{zy} & \sigma_z \end{pmatrix} \tag{2.19}$$

Figure 2.7 displays all of these stress components acting on a cube. For the cube to be at rest, all the forces exerted by the stresses on the faces must be in equilibrium. For symmetry reasons, this leads to

$$\tau_{xy} = \tau_{yx},\ \tau_{xz} = \tau_{zx} \text{ and } \tau_{yz} = \tau_{zy}. \tag{2.20}$$

Thus, the number of independent stress components is reduced to six.

Works on the theory of elasticity (eg. Sokolnikoff, 1956) usually treat tensile normal stresses as positive. But compressive stresses are much more common in the subsurface, thus the *rock mechanics sign convention* defines compressive stresses, i.e. stresses in the negative direction

of the axes, as positive. This sign convention will be used in this work. The stress components shown in Figure 2.7 are accordance with this sign convention.

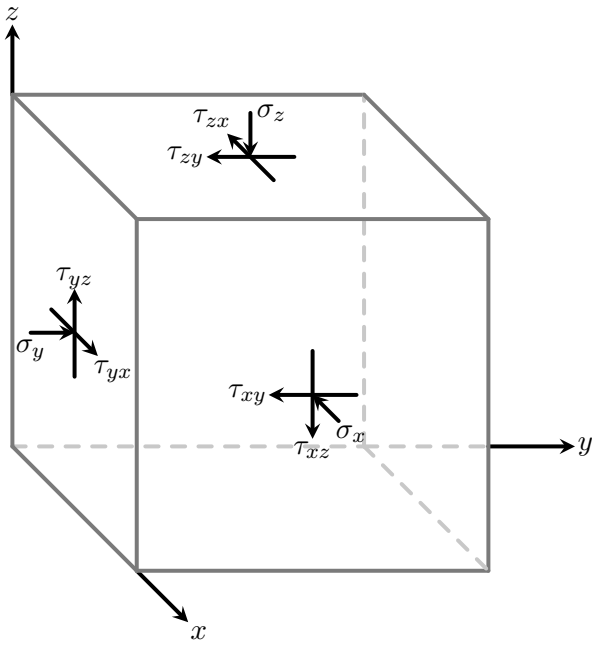

Figure 2.7: Visualisation of stress components on a cube in three dimensions.

2.2.3 Displacement and strain

To describe the deformation of rock, the initial position $\boldsymbol{x}$ with the components x, y and z of every rock particle is compared to its final position $\boldsymbol{x^*} = (x^*, y^*, z^*)$ resulting from the acting forces (see Figure 2.8a). The components u, v, w of the displacement vector $\boldsymbol{u}$ are then defined as

$$u = x - x^*, \; v = y - y^*, \text{ and } w = z - z^*. \tag{2.21}$$

Positive displacements are oriented in negative direction of the axes, so positive displacements correspond with positive stresses in the sense of the rock mechanics sign convention introduced in Subsection 2.2.2.

If movement as a rigid body cannot account for the changed positions of the material particles, the body is strained. The state of strain can be measured as the change in length and as the change of the angle. If the distance l between two material points in the unstrained state becomes the distance l^* in the strained state, the elongation or contraction e is defined as

$$e = \frac{l - l^*}{l}. \tag{2.22}$$

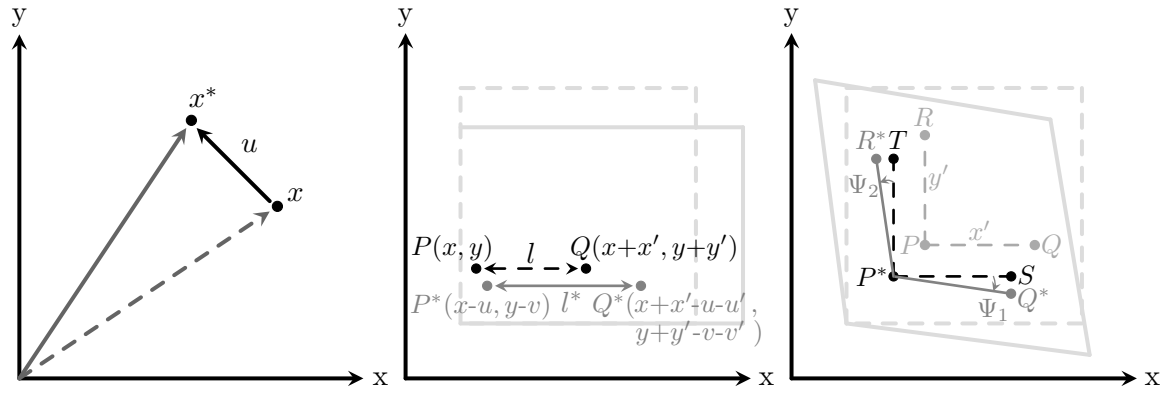

(a) Displacement **(b)** Normal Strain **(c)** Shear Strain

Figure 2.8: Visualisation for the definitions of displacement and strain.

Considering two infinitesimally close points $P(x, y)$ and $Q(x + x', y + y')$ and a continuous displacement field, the components of the displacement of Q^* are $u+u'$ and $v+v'$ (Figure 2.8b). Using Taylor's theorem, u' and v' can be approximated as

$$u' \approx x' \frac{\partial u}{\partial x} + y' \frac{\partial u}{\partial y} \tag{2.23}$$

$$v' \approx x' \frac{\partial v}{\partial x} + y' \frac{\partial v}{\partial y}. \tag{2.24}$$

The squares, products, etc. of x', y' can be neglected as P and Q are infinitesimally close. Furthermore, the derivatives $\partial u/\partial y$ and $\partial v/\partial y$ are zero as the displacements are constant in the y-direction here.

The elongation or strain within this infinitesimal element can then be expressed as

$$\epsilon_x = \frac{\overline{P^*Q^*} - \overline{PQ}}{\overline{PQ}} = \frac{x' - (x' - u')}{x'} = \frac{u'}{x'} = \frac{\partial u}{\partial x}. \tag{2.25}$$

and as

$$\epsilon_y = \frac{\partial v}{\partial y} \tag{2.26}$$

and

$$\epsilon_z = \frac{\partial w}{\partial z} \tag{2.27}$$

in the y- and z-direction. Consistent with the concept of normal stresses, ϵ_x, ϵ_x and ϵ_z are called the normal strain components.

Figure 2.8c shows a case where an infinitesimal element is subjected to both normal and shear forces. The points R, P and Q become R^*, P^* and Q^*. The shear strain describes the angular change. To better illustrate this, the line segments $\overline{P^*S}$ and $\overline{P^*T}$ represent parallel projections

of $\overline{P^*Q^*}$ and $\overline{P^*R^*}$ onto lines parallel to $\overline{PQ}$ and $\overline{PR}$. The tangent of Ψ_1 is then given by

$$\tan\Psi_1 = \frac{\overline{SQ^*}}{\overline{P^*S}} = \frac{(v'/x')x'}{x' + (u'/x')x'} = \frac{\partial v/\partial x}{1 + \partial u/\partial x}. \tag{2.28}$$

Following the derivation of Kutz (2015), small displacement gradients are assumed for the infinitesimal element, so the denominator is very close to unity. Thus, Equation 2.28 can be approximated by

$$\tan\Psi_1 \approx \frac{\partial v}{\partial x}. \tag{2.29}$$

In a similar fashion, the angle Ψ_2 between the line segments $\overline{P^*T}$ and $\overline{P^*R^*}$ can be approximated as

$$\tan\Psi_2 \approx \frac{\overline{TR^*}}{\overline{P^*T}} = \frac{\frac{\partial u}{\partial y}}{1 + \frac{\partial v}{\partial y}}, \tag{2.30}$$

which again becomes

$$\tan\Psi_2 \approx \frac{\partial u}{\partial y}. \tag{2.31}$$

Using the assumption of small displacements, small displacement gradients and small angles Ψ_1 and Ψ_2, which are expressed in radians here, Equation 2.29 and 2.31 can be simplified to

$$\tan\Psi_1 \approx \Psi_1 \quad \text{and} \quad \tan\Psi_2 \approx \Psi_2. \tag{2.32}$$

The shear strain γ describing the angular change can be defined as the sum of the angles Ψ_1 and Ψ_2:

$$\gamma_{xy} = \gamma_{yx} = \Psi_1 + \Psi_2. \tag{2.33}$$

Combining this with Equation 2.29, 2.31 and 2.32 leads to

$$\gamma_{xy} = \gamma_{yx} = \frac{\partial v}{\partial x} + \frac{\partial u}{\partial y}. \tag{2.34}$$

Alternatively, the shear strain can be defined as the average of the angles Ψ_1 and Ψ_2:

$$\Gamma_{xy} = \Gamma_{yx} = \frac{1}{2}\left(\frac{\partial v}{\partial x} + \frac{\partial u}{\partial y}.\right). \tag{2.35}$$

To distinguish the two definitions, for Γ_{xy} the term *tensoral shear strain* is often used, while γ_{xy} is usually called *engineering shear strain.*

Both normal and shear strain can be written as components of the stress tensor $\boldsymbol{\epsilon}$, similar to

normal and shear stresses making up the stress tensor $\boldsymbol{\sigma}$ in Equation 2.19:

$$\boldsymbol{\epsilon} = \begin{pmatrix} \epsilon_x & \Gamma_{xy} & \Gamma_{xz} \\ \Gamma_{yx} & \epsilon_y & \Gamma_{yz} \\ \Gamma_{zx} & \Gamma_{zy} & \epsilon_z \end{pmatrix} = \frac{1}{2}(\operatorname{grad} \boldsymbol{u} + \operatorname{grad}^{\mathrm{T}} \boldsymbol{u}). \tag{2.36}$$

2.2.4 Linear Elasticity

A common way to analyse the mechanical behaviour of rock is to compress a cylindrical sample while measuring the axial strain $\epsilon_z = \partial w / \partial z$ can be determined (see Figure 2.10a). Such experiments are often performed for two principal stresses to be equal (usually $\sigma_1 > \sigma_2 = \sigma_3$), therefore this experimental set-up is usually referred to as the *triaxial test*. Plotting stress against strain results in the *stress-strain curve*. Experimental data such as shown in Figure 2.9 for a Berea Sandstone sample indicates a linear correlation between stress and strain in the regions of interest. In the same sense, Jaeger and Cook (1976) conclude that the assumption of a linear relationship between stress and strain is reasonable for most rocks until failure occurs.

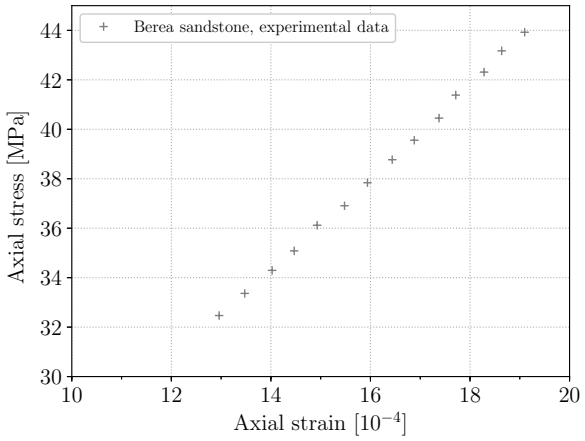

Figure 2.9: Laboratory measurements for stress and strain of a cylindrical Berea Sandstone sample from Hart and Wang (1995), performed under undrained conditions.

For the uniaxial case, i.e. $\sigma_2 = \sigma_3 = 0$, the rock's mechanical response can then be described by

$$\sigma = E\,\epsilon \tag{2.37}$$

with E as the *Young's modulus* describing the rock's stiffness. When Equation 2.37 is applicable, the material is characterised as *linearly elastic*. The equation is also known as Hooke's law after the British physicist Robert Hooke.

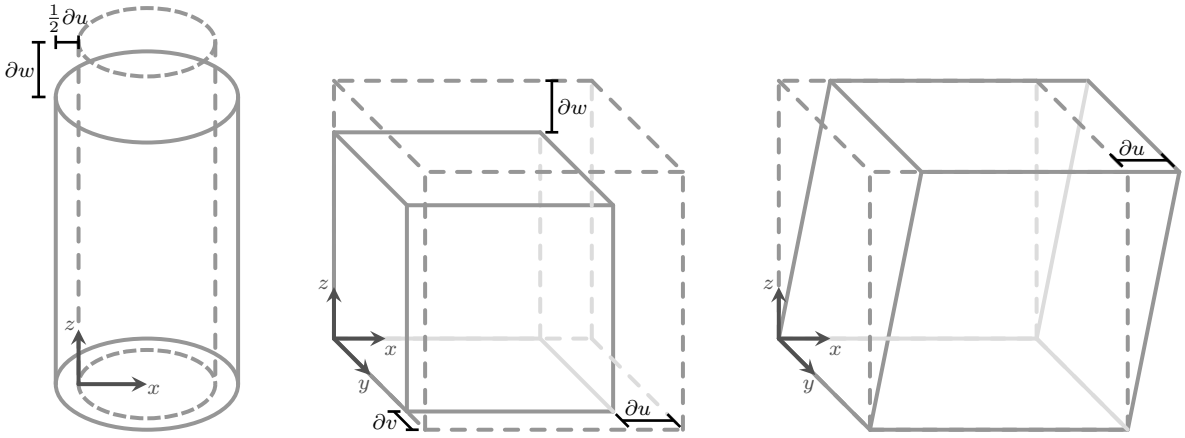

(a) Young's modulus, Poisson's ratio

(b) Bulk modulus

(c) Shear modulus

Figure 2.10: Illustration of the different elastic moduli.

If this one-dimensional definition of linear elasticity is extended to three dimensions, the stress and strains tensors with 9 entries each require a fourth order tensor with 81 entries so that each stress component is a linear function of the strain components. Symmetry and energetic considerations together with the assumption of isotropy reduce the number of entries to two (Jaeger and Cook, 1976). Regarding the experiment described above, the contraction of the cylindrical rock sample due to a compressive stress σ_z will be accompanied by lateral expansion and thus cause negative strain $-\epsilon_x$ normal to σ_z (see Figure 2.10a). Consequently, the Poisson's ratio

$$\nu = -\frac{\epsilon_x}{\epsilon_z} = -\frac{\partial u/\partial x}{\partial w/\partial z} \tag{2.38}$$

describing this effect is commonly used as the second elastic constant (Jaeger and Cook, 1976). This leads to the following relationship for stress and strain in three dimensions:

$$\begin{pmatrix} \epsilon_x \\ \epsilon_y \\ \epsilon_z \\ \gamma_{yz} \\ \gamma_{xz} \\ \gamma_{xy} \end{pmatrix} = \frac{1}{E} \begin{pmatrix} 1 & -\nu & -\nu & 0 & 0 & 0 \\ -\nu & 1 & -\nu & 0 & 0 & 0 \\ -\nu & -\nu & 1 & 0 & 0 & 0 \\ 0 & 0 & 0 & 2(1+\nu) & 0 & 0 \\ 0 & 0 & 0 & 0 & 2(1+\nu) & 0 \\ 0 & 0 & 0 & 0 & 0 & 2(1+\nu) \end{pmatrix} \begin{pmatrix} \sigma_x \\ \sigma_y \\ \sigma_z \\ \tau_{yz} \\ \tau_{xz} \\ \tau_{xy} \end{pmatrix} \tag{2.39}$$

Beside the Young's modulus and Poisson's ratio, three more elastic constants are commonly used. If the rock sample is subjected to equal stresses in all direction ($\sigma_1 = \sigma_2 = \sigma_3 = \sigma_\mathrm{v}$, the so-called *volumetric stress*, Figure 2.10b), the bulk modulus K describes its resistance to compression:

$$K = \frac{\sigma_\mathrm{v}}{\epsilon_\mathrm{v}} \tag{2.40}$$

with $\epsilon_\mathrm{v} = \epsilon_x + \epsilon_y + \epsilon_z$ as the volumetric strain. The ratio of shear stress and shear strain defines the shear modulus (see Figure 2.10c):

$$G = \frac{\tau_{xy}}{\Gamma_{xy}} \tag{2.41}$$

Lamé's first parameter λ has no obvious physical interpretation but can be calculated from any two of the elastic moduli previously described. This is true for all moduli, as Table 2.1 shows.

Table 2.1: Conversion of elastic moduli for homogeneous isotropic linear elastic materials: Given any two elastic moduli, any other of the elastic moduli can be calculated according to these formulas. The formulas are taken from Mavko et al. (1998). $^*X = \sqrt{E^2 + 9\lambda^2 + 2E\lambda}$

	K	E	λ	G	ν
K, E	K	E	$\frac{3K(3K-E)}{9K-E}$	$\frac{3KE}{9K-E}$	$\frac{3K-E}{6K}$
K, λ	K	$\frac{9K(K-\lambda)}{3K-\lambda}$	λ	$\frac{3(K-\lambda)}{2}$	$\frac{\lambda}{3K-\lambda}$
K, G	K	$\frac{9KG}{3K+G}$	$K - \frac{2G}{3}$	G	$\frac{3K-2G}{2(3K+G)}$
K, ν	K	$3K(1-2\nu)$	$\frac{3K\nu}{1+\nu}$	$\frac{3K(1-2\nu)}{2(1+\nu)}$	ν
E, λ	$\frac{E+3\lambda+X^*}{6}$	E	λ	$\frac{E-3\lambda+X^*}{4}$	$\frac{2\lambda}{E+\lambda+X^*}$
E, G	$\frac{EG}{3(3G-E)}$	E	$\frac{G(E-2G)}{3G-E}$	G	$\frac{E}{2G} - 1$
E, ν	$\frac{E}{3(1+\nu)}$	E	$\frac{E\nu}{(1+\nu)(1-2\nu)}$	$\frac{E}{2(1+\nu)}$	ν
λ, G	$\lambda + \frac{2G}{3}$	$\frac{G(3\lambda+2G)}{\lambda+G}$	λ	G	$\frac{\lambda}{2(\lambda+G)}$
λ, ν	$\frac{\lambda(1+\nu)}{3\nu}$	$\frac{\lambda(1+\nu)(1-2\nu)}{\nu}$	λ	$\frac{\lambda(1-2\nu)}{2\nu}$	ν
G, ν	$\frac{2G(1+\nu)}{3(1-2\nu)}$	$2G(1+\nu)$	$\frac{2G\nu}{1-2\nu}$	G	ν

2.3 Poroelasticity

Up to this point, the considerations on the mechanical behaviour of rock treated the rock as a solid. However, many rocks are in fact porous and contain fluid-filled pores (see Section 2.1). The contribution of those fluids to the mechanical response of a rock is taken into account within the theory of poroelasticity. Detouray and Cheng (1993) provide a comprehensive study of the theory. The relationships presented in the following are taken from their work.
Beside the solid and the fluid, the pore space also controls the strength of the porous rock through properties such as the distribution of the pores and their size, shape and orientation. This becomes apparent if one imagines a pile of loose sand, where the individual grains' contribution to the strength is negligible in comparison the packing density of the grains.
Consequently, the total resistance of a porous material to compression denoted with the bulk modulus K can be split into the contribution of the solid K_s, the fluid K_f and the pore volume K_p.
The total bulk modulus K can be measured in two ways: One can either determine the resistance to compression while allowing the fluid to escape (so-called *drained conditions*) or seal the surface to keep the fluid inside the sample (so-called *undrained conditions*). The drained bulk modulus K_dr is a measure for the porous solid frame without fluid and can be expressed as function of K_s, K_p and ϕ:

$$K_\mathrm{dr} = \frac{K_\mathrm{p}}{\phi}\left(1 - \frac{K_\mathrm{p}}{K_\mathrm{p} + \phi K_\mathrm{s}}.\right) \tag{2.42}$$

For relatively rigid solid grains, $K_\mathrm{s} \to \infty$, so only K_p and ϕ control the compressibility:

$$K_\mathrm{dr} = \frac{K_\mathrm{p}}{\phi} \tag{2.43}$$

The undrained bulk modulus K_u takes the effect of the fluid's compressibility K_f into account:

$$K_\mathrm{u} = K_\mathrm{dr}\left(1 + \frac{\left(1 - \frac{K_\mathrm{dr}}{K_\mathrm{s}}\right)^2}{\frac{K_\mathrm{dr}}{K_\mathrm{s}}\left(1 - \frac{K_\mathrm{dr}}{K_\mathrm{s}}\right) + \phi\left(\frac{K_\mathrm{dr}}{K_\mathrm{f}} - \frac{K_\mathrm{dr}}{K_\mathrm{s}}\right)}\right) \tag{2.44}$$

If again the solid grains are assumed to be incompressible (i.e. $K_\mathrm{dr}/K_\mathrm{s} \to 0$), this becomes:

$$K_\mathrm{u} = K_\mathrm{dr} + \frac{K_\mathrm{f}}{\phi} \tag{2.45}$$

Comparing the Equation 2.45 and 2.43 reveals that the undrained bulk modulus is the sum of the drained bulk modulus and fluid's contribution. This coincides with the intuition that a

porous material behaves more stiff under undrained conditions than under drained conditions. In similar line of thinking, Karl von Terzaghi formulated in 1923 that the pore pressure reduces the acting stress under loading. For this reduced stress, he coined the term *effective stress* $\boldsymbol{\sigma'}$, which he defined as

$$\boldsymbol{\sigma'} = \boldsymbol{\sigma} - p\,\mathbf{I}. \tag{2.46}$$

Here, the pore pressure p counteracts the compressive stress $\boldsymbol{\sigma}$. In 1941, Maurice Anthony Biot reformulated this to

$$\boldsymbol{\sigma'} = \boldsymbol{\sigma} - \alpha\, p\,\mathbf{I} \tag{2.47}$$

with α as the Biot coefficient, which is defined as

$$\alpha = 1 - \frac{K_{\mathrm{dr}}}{K_{\mathrm{s}}} \tag{2.48}$$

For $K_{\mathrm{s}} \to \infty$, Biot's formulation coincides with Terzaghi's definition of the effective stress. In the two-phase system, instead of the pore pressure p, the *effective pore pressure* p_{eff} is used, which is calculated from pressure of each phase weighted by the respective saturations:

$$p_{\mathrm{eff}} = S_{\mathrm{w}} p_{\mathrm{w}} + S_{\mathrm{n}} p_{\mathrm{n}}. \tag{2.49}$$

2.3.1 Effective Porosity

The components of the porous medium exhibit different responses to stress and pressure changes. To describe this, the different bulk moduli were introduced. This has also consequences for the porosity ϕ. Its change is defined as:

$$\mathrm{d}\phi = \mathrm{d}\left(\frac{V_{\mathrm{p}}}{V_{\mathrm{b}}}\right) = \frac{\mathrm{d}V_{\mathrm{p}}}{V_{\mathrm{b}}} - \phi\frac{\mathrm{d}V_{\mathrm{b}}}{V_{\mathrm{b}}} \tag{2.50}$$

with the pore volume V_{p} and the bulk volume V_{b}. With Equation 2.47 and 2.40, the change in bulk volume V_{p} can be described as a function of the volumetric stress σ_{v} and the pore pressure p

$$\frac{\mathrm{d}V_{\mathrm{b}}}{V_{\mathrm{b}}} = -\frac{1}{K_{\mathrm{dr}}}\left(\mathrm{d}\sigma_{\mathrm{v}} - \alpha\,\mathrm{d}p\right) \tag{2.51}$$

By introducing an effective stress coefficient

$$\beta = 1 - \frac{K_{\mathrm{p}}}{K_{\mathrm{s}}} \tag{2.52}$$

for the pore volume V_p (equivalent to the Biot coefficient α for the bulk volume V_b), the change in the pore volume V_p can be expressed as

$$\frac{\mathrm{d}V_\mathrm{p}}{V_\mathrm{p}} = -\frac{1}{K_\mathrm{p}}\left(\mathrm{d}\sigma_\mathrm{v} - \beta\,\mathrm{d}p\right) \tag{2.53}$$

as described in Detouray and Cheng (1993). By using Equation 2.51 and 2.53 and by exploiting $V_\mathrm{p} = \phi\, V_\mathrm{b}$, $\mathrm{d}\phi$ becomes

$$\begin{aligned}\mathrm{d}\phi = \quad & -\frac{1}{K_\mathrm{p}}\,\phi\,\mathrm{d}\sigma_\mathrm{v} + \frac{\beta}{K_\mathrm{p}}\,\phi\,\mathrm{d}p \\ & +\frac{1}{K_\mathrm{dr}}\,\phi\,\mathrm{d}\sigma_\mathrm{v} - \frac{\alpha}{K_\mathrm{dr}}\,\phi\,\mathrm{d}p\end{aligned} \tag{2.54}$$

or

$$\begin{aligned}\mathrm{d}\phi = \quad & -\frac{1}{K_\mathrm{p}}\,\phi\,\mathrm{d}\sigma_\mathrm{v} + \frac{1-\frac{K_\mathrm{p}}{K_\mathrm{s}}}{K_\mathrm{p}}\,\phi\,\mathrm{d}p \\ & +\frac{1}{K_\mathrm{dr}}\,\phi\,\mathrm{d}\sigma_\mathrm{v} - \frac{1-\frac{K_\mathrm{dr}}{K_\mathrm{s}}}{K_\mathrm{dr}}\,\phi\,\mathrm{d}p\end{aligned} \tag{2.55}$$

which simplifies to

$$\mathrm{d}\phi = \left(-\frac{\phi}{K_\mathrm{dr}} + \frac{\phi}{K_\mathrm{p}}\right)\left(-\mathrm{d}\sigma_\mathrm{v} + \mathrm{d}p\right). \tag{2.56}$$

Using $K_\mathrm{p} = \frac{\phi}{\alpha}K_\mathrm{dr}$ (Detouray and Cheng, 1993), one obtains

$$\mathrm{d}\phi = \left(-\frac{\phi}{K_\mathrm{dr}} + \frac{\alpha}{K_\mathrm{dr}}\right)\left(-\mathrm{d}\sigma_\mathrm{v} + \mathrm{d}p\right). \tag{2.57}$$

Finally, with $\frac{1}{K_\mathrm{s}} = \frac{1-\alpha}{K_\mathrm{dr}}$, the change in porosity can be expressed as

$$\mathrm{d}\phi = \left(\frac{1}{K_\mathrm{dr}}(1-\phi) - \frac{1}{K_\mathrm{s}}\right)\left(-\mathrm{d}\sigma_\mathrm{v} + \mathrm{d}p\right). \tag{2.58}$$

This is in agreement with the relationship published in Han and Dusseault (2003), which was derived from the different compressibilities defined in Zimmerman (1991) instead of the different bulk moduli. Han and Dusseault (2003) further replace the stress with volumetric strain, so Equation 2.58 becomes

$$\mathrm{d}\phi = \left(1 - \frac{K_\mathrm{dr}}{K_\mathrm{s}} - \phi\right)\left(-\mathrm{d}\epsilon_\mathrm{v} + \frac{1}{K_\mathrm{s}}\mathrm{d}p\right). \tag{2.59}$$

For the assumption of very rigid grains ($K_\mathrm{s} \to \infty$), this reduces to

$$\mathrm{d}\phi = -\left(1-\phi\right)\mathrm{d}\epsilon_\mathrm{v}. \tag{2.60}$$

This allows to calculate an *effective porosity* ϕ_{eff} from the volumetric strain ϵ_{v} and the initial porosity ϕ_0 (assuming $\epsilon_{\text{v},0} = 0$):

$$\phi_{\text{eff}} = \frac{\phi_0 - \epsilon_{\text{v}}}{1 - \epsilon_{\text{v}}} \tag{2.61a}$$

or as a function of the displacements by referring to the volumetric strain ϵ_{v} as div $\mathbf{u}$:

$$\phi_{\text{eff}} = \frac{\phi_0 - \text{div } \mathbf{u}}{1 - \text{div } \mathbf{u}} \tag{2.61b}$$

Some of the steps of this derivation are explained in more detail in the appendix.
One could also argue that the change in the denominator in Equation 2.61a and 2.61b is negligible, so it becomes

$$\phi_{\text{eff}} = \phi_0 - \epsilon_{\text{v}}. \tag{2.62}$$

Instead of deriving the porosity change from the interacting components of the porous material and their respective bulk moduli, one can also define a pore compressibility

$$c_{\text{p}} = \frac{\mathrm{d}V_{\text{p}}}{V_{\text{p}}} \frac{1}{\mathrm{d}p} = \frac{1}{\phi} \frac{\mathrm{d}\phi}{\mathrm{d}p} \tag{2.63}$$

which just depends on the changes in pore pressure. By comparing this equation with Equation 2.53, it becomes apparent that the definition of the pores compressibility ignores the stress contribution and assumes incompressible grains ($\alpha = \beta = 0$). Thus, the pore compressibility is related to K_{p} and K_{dr} by

$$c_{\text{p}} = \frac{1}{K_{\text{p}}} = \frac{1}{\phi K_{\text{dr}}}. \tag{2.64}$$

In a linearised form, the effective porosity is then obtained from the difference between the initial pressure p_0 and the current pressure p:

$$\phi_{\text{eff}} = \phi_0 + \frac{1}{K_{\text{dr}}}(p - p_0). \tag{2.65}$$

2.3.2 Effective Permeability

The change in porosity will also have an effect on the permeability tensor. To distinguish it from the intrinsic permeability tensor $\mathbf{K}$, is will be referred to as the *effective permeability tensor* $\mathbf{K}_{\text{eff}}$. A classical model to the determine the effective permeability is the Kozeny-Carman relationship (Carman, 1937; Kozeny, 1927). The relationship idealizes the porous medium as circular pipes of constant cross-section. The diagonal entries k_{eff} of the permeability tensor

are then calculated from the porosity ϕ with

$$k_{\text{eff}} = B\frac{\phi^3}{S^2}, \tag{2.66}$$

where B is a geometric factor and S the pore surface area per volume of rock. It is common to express S in terms of the average diameter of the grains d (e.g. Mavko and Nur, 1997):

$$S = \frac{3}{2}\frac{1-\phi}{d}, \tag{2.67}$$

so Equation 2.66 becomes

$$k_{\text{eff}} = B\frac{\phi^3}{(1-\phi)^2}d^2. \tag{2.68}$$

Here, the factor 3/2 is included in the constant B.
Mavko and Nur (1997) argue that the relationship should be expanded by a percolation porosity ϕ_c representing the threshold porosity at which pores become disconnected:

$$k_{\text{eff}} = B\frac{(\phi-\phi_c)^3}{(1+\phi_c-\phi)^2}d^2 \approx B(\phi-\phi_c)^3 d^2 \tag{2.69}$$

This accounts for effects such as cementation in sedimentary rocks. B and ϕ_c can be chosen to give a good fit with experimental data.
Beside the Kozeny-Carman relationship and its derivatives, many other empirical relationships for porosity and permeability exist. As an example, Rutqvist and Tsang (2002) modified an exponential relationship obtained for experimental data by Davies and Davies (1999):

$$k_{\text{eff}} = k_0 \exp\left(22.2\left(\frac{\phi_{\text{eff}}}{\phi_0} - 1\right)\right) \tag{2.70}$$

It is listed here as it is commonly used for some of the scenarios that will be covered in this work.

2.3.3 Transformation of the stress tensor

Changing the orientation of the coordinate system will have an effect on the respective stress tensor. A common way to derive the transformation for a two-dimensional case is based on the equilibrium of forces such as described in Jaeger and Cook (1976) and Hudson and Harrison (1997): A square element is rotated in a way, so that the corners A and B touch two sides of the original square (see Figure 2.11, left). Everything except the triangle OAB is now cut off and the stress components acting on the sides are examined. The length of sides are: AB = d,

OB $= d\cos\theta$ and OA $= d\sin\theta$. Thus, the equilibrium of forces in direction of x' gives

$$\begin{aligned}\Sigma F_{x'} &= (\sigma_x\, d\cos\theta)\cos\theta + (\sigma_y\, d\sin\theta)\sin\theta \\ &\quad + (\tau_{xy}\, d\cos\theta)\sin\theta + (\tau_{yx}\, d\sin\theta)\cos\theta + \sigma_{x'}\, d \\ &= 0. \end{aligned} \tag{2.71}$$

Using $\tau_{xy} = \tau_{yx}$, this simplifies to

$$\sigma_{x'} = \sigma_x \cos^2\theta + \sigma_y \sin^2\theta + 2\,\tau_{xy}\sin\theta\cos\theta. \tag{2.72}$$

Evaluating the forces in y'-direction gives

$$\begin{aligned}\Sigma F_{y'} &= -(\sigma_x\, d\cos\theta)\sin\theta + (\sigma_y\, d\sin\theta)\cos\theta \\ &\quad + (\tau_{xy}\, d\cos\theta)\cos\theta - (\tau_{yx}\, d\sin\theta)\sin\theta - \tau_{x'y'}\, d = 0, \end{aligned} \tag{2.73}$$

which again simplifies to

$$\tau_{x'y'} = \tau_{xy}\,(\cos^2\theta - \sin^2\theta) - (\sigma_x - \sigma_y)\sin\theta\cos\theta. \tag{2.74}$$

To determine $\sigma_{y'}$, θ can be replaced by $\theta + \pi/2$, as $\sigma_{y'}$ is perpendicular to $\sigma_{x'}$:

$$\sigma_{y'} = \sigma_x \sin^2\theta + \sigma_y \cos^2\theta - 2\,\tau_{xy}\sin\theta\cos\theta \tag{2.75}$$

Altogether, the stress transformation can be summarised in matrix form as

$$\begin{pmatrix} \sigma_{x'} & \tau_{x'y'} \\ \tau_{x'y'} & \sigma_{y'} \end{pmatrix} = \begin{pmatrix} \cos\theta & \sin\theta \\ -\sin\theta & \cos\theta \end{pmatrix} \begin{pmatrix} \sigma_x & \tau_{xy} \\ \tau_{xy} & \sigma_y \end{pmatrix} \begin{pmatrix} \cos\theta & -\sin\theta \\ \sin\theta & \cos\theta \end{pmatrix}. \tag{2.76}$$

When Equation 2.72 and 2.75 are added, it becomes apparent, that the sum of the respective normal stresses is invariant to a rotation of the axis:

$$\sigma_{x'} + \sigma_{y'} = \sigma_x + \sigma_y \tag{2.77}$$

Furthermore, from Equation 2.74 it can be derived that $\tau_{x'y'} = 0$ if

$$\tan 2\theta = \frac{2\,\tau_{xy}}{\sigma_x - \sigma_y}. \tag{2.78}$$

In other words: There exists a value for θ for which the shear stress becomes zero. The directions x' and y' are then the *principal directions* and $\sigma_{x'}$ and $\sigma_{y'}$ the *principal stresses*. The larger of the two is denoted as σ_1 and the smaller one as σ_2.

Beside the derivation from the equilibrium of forces on a triangle, the principal stresses also represent the eigenvalues of the stress tensor and thus can be determined by solving an eigenvalue problem. This allows for an easy calculation of the principal stresses in two and three dimensions.

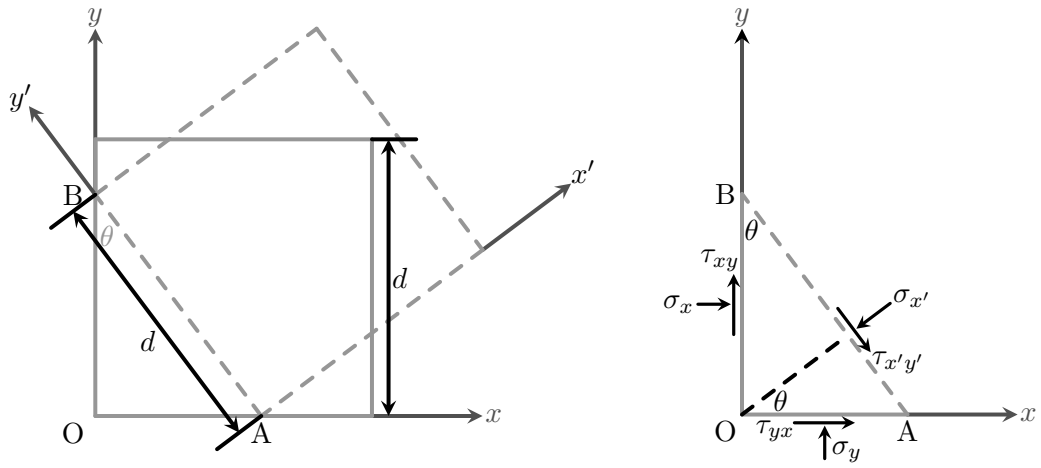

Figure 2.11: Stress components in different coordinate systems.

2.3.4 Mohr's circle

Up to this point, the question of how to deal with rotated stresses lead to the concept of principal stresses. But a slight adaption of the previously derived equations provides an easy visualisation of the transformed stress tensor: Using trigonometric formulae, Equation 2.72 may be written as

$$\sigma_{x'} = \frac{1}{2}(\sigma_x + \sigma_y) + \frac{1}{2}(\sigma_x - \sigma_y)\cos 2\theta + \tau_{xy}\sin 2\theta \tag{2.79}$$

and Equation 2.74 becomes

$$\tau_{x'y'} = \tau_{xy}\cos 2\theta - (\sigma_x - \sigma_y)\sin 2\theta. \tag{2.80}$$

For the x- and y-axis oriented in the direction of the principal stresses, the normal and shear stresses on plane inclined by the angle θ are then

$$\sigma = \frac{1}{2}(\sigma_1 + \sigma_2) + \frac{1}{2}(\sigma_1 - \sigma_2)\cos 2\theta \tag{2.81}$$

$$\tau = -\frac{1}{2}(\sigma_1 - \sigma_2)\sin 2\theta. \tag{2.82}$$

This dependence of the normal and shear stresses can be visualised with Mohr's circle, named after the German civil engineer Christian Otto Mohr, as Equation 2.81 describes a circle with the centre

$$\sigma_{\mathrm{m}} = \frac{1}{2}(\sigma_1 + \sigma_2) \tag{2.83}$$

and the radius

$$\tau_{\mathrm{m}} = \frac{1}{2}(\sigma_1 - \sigma_2). \tag{2.84}$$

Figure 2.12 displays a coordinate system with σ as the x-axis and the absolute value of τ as the y-axis (also known as the Mohr diagram). Normal and shear stress of any orientation inclined by θ with respect to the direction of the principal stresses can then be determined from the x- and y-coordinate of the corresponding point on the (semi-)circle. Please note that an angle θ in the physical space corresponds with 2θ for Mohr's circle.

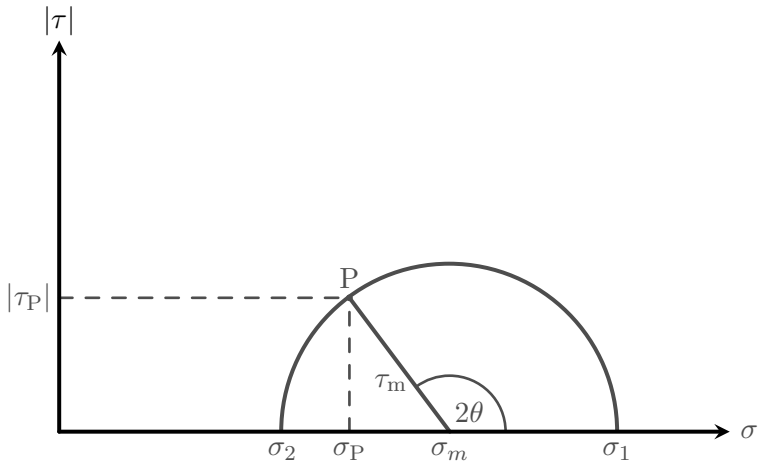

Figure 2.12: The Mohr circle graphically illustrates the stress components acting on a plane inclined by an angle θ. The x-coordinate of a point on the circle corresponds the normal stress σ_P, while the y-coordinate represents the absolute value of the shear stress τ_P.

The pore pressure p reduces the compressive normal stresses (see Equation 2.47). For Mohr's circle, this means that it is shifted to the left (see Figure 2.13).

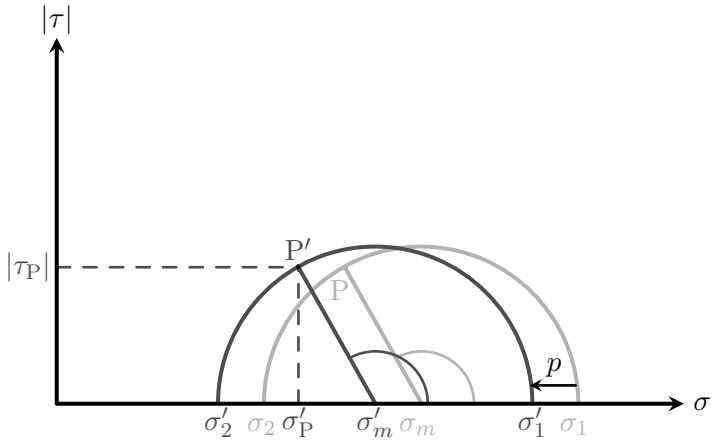

Figure 2.13: The pore pressure p reduces the compressive normal stresses and thus, the Mohr circle is shifted to the left. The stress state P becomes the effective stress state P′ with effective normal stress σ'_P and shear stress τ_P, which is not affected by the pore pressure.

2.3.5 Rock Failure

In Subsection 2.2.4, the concept of elasticity was introduced. A linear relationship between stress and strain was assumed, which lead to a description of the rock's behaviour as linearly elastic. This assumption is of course not unconditionally valid, but restricted to certain stress states. The limit of elastic behaviour is referred to as the *yield point* and above it, loading will cause irreversible changes in the rock's structure or properties. Here, one can distinguish between *ductile* and *brittle* deformation. During ductile behaviour, the rock experiences permanent deformation while maintaining its ability to resist load. In contrast, the rock's ability to resist a load will decrease with increasing deformation in a brittle state (Jaeger and Cook, 1976).

When the point of brittle behaviour is reached during testing, e.g. during the compression experiment of a cylindrical sample described in Subsection 2.2.4, a visible plane of separation – a *fracture* – will most likely occur. If this happens suddenly and without any previously visible irreversible deformation, it is referred to as a *brittle fracture*, whereas a visible irreversible deformation before separation will result in a *ductile fracture*.

A typical orientation of a fracture resulting from compression is shown in Figure 2.14a. Jaeger and Cook (1976) denote such a fracture, which developed in an experimental context, as a *shear fracture*. Nonetheless, its characteristic relative movement along a surface would justify the designation *fault* if viewed from a geologist's perspective. In any case the feature is a result of *shear failure* and can be clearly distinguished from an *extensional fracture* resulting from tensile forces Figure 2.14b. In the following, criteria to estimate the onset of shear and tensile failure will be presented.

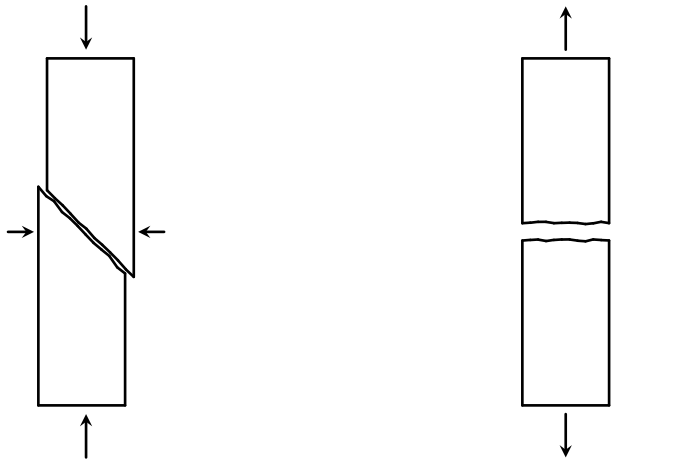

(a) Shear Fracture **(b)** Extensional Fracture

Figure 2.14: Examples for different types of fractures, modified after Jaeger and Cook (1976).

2.3.6 Failure evaluation

A widely used criterion to determine whether shear failure would occur makes use of the Mohr diagram: The *Mohr–Coulomb failure criterion* (after Charles-Augustin de Coulomb and the already mentioned Christian Otto Mohr) states that shear failure occurs when the shear stress τ of the rock surpasses its shear strength τ_s. The shear strength depends linearly on the effective normal stress σ'

$$\tau_\mathrm{s} = \sigma' \tan \beta_\mathrm{frict} + c = \sigma' \mu_\mathrm{frict} + c \tag{2.85}$$

with β_frict as the angle of internal friction, $\mu = \tan \beta_\mathrm{frict}$ as the friction coefficient and c accounting for internal cohesive forces. So the higher the effective compressive normal stresses are, the less likely shear failure occurs. Reducing the effective normal stresses while keeping the shear stress constant however bears the risk of shear failure, which is exactly what occurs when the pore pressure p is raised. In the Mohr diagram, Equation 2.85 is represented by a straight line. This failure curve is displayed in Figure 2.15 for a case with no cohesion. Increasing the pore pressure brings Mohr's circle closer to the failure curve until the circle touches the failure curve. It can be shown that one has

$$\tau_\mathrm{m} = \sigma'_\mathrm{m} \sin \beta_\mathrm{frict} + c \cos \beta_\mathrm{frict} = (\sigma_\mathrm{m} - p) \sin \beta_\mathrm{frict} + c \cos \beta_\mathrm{frict} \tag{2.86}$$

for the intersection point P′ (e.g. Jaeger and Cook, 1976). With this equation, a critical pressure for the onset of shear failure is defined as:

$$p_\mathrm{crit} = \frac{\tau_\mathrm{m}}{\sin \beta_\mathrm{frict}} + \frac{c}{\tan \beta_\mathrm{frict}} + \sigma'_\mathrm{m} \tag{2.87}$$

As long as the pressure difference

$$p_{\text{shear}} = p_{\text{eff}} - p_{\text{crit}} \tag{2.88}$$

between the effective pore pressure p_{eff} and critical pressure p_{crit} is negative, the compressive normal stresses are high enough to prevent shear failure. Similar definitions of a pressure margin were used by Rutqvist et al. (2002) and within the thesis of Darcis (2013).

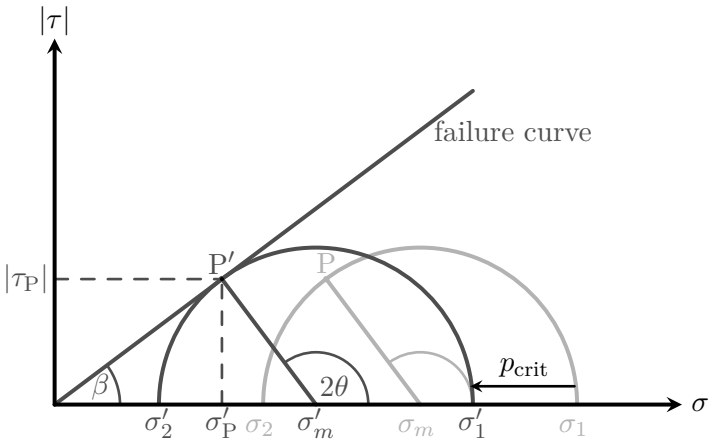

Figure 2.15: For a critical pore pressure p_{crit}, the Mohr circle touches the failure curve defined by the Mohr–Coulomb failure criterion (Equation 2.85).

On closer inspection, one notices that the definition of p_{crit} requires a plane in the orientation of point P′ to be present. In other words, this is a worst case assumption for the onset of shear failure.

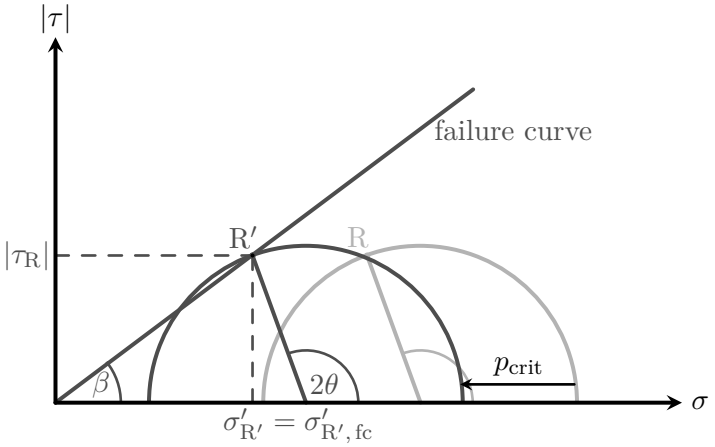

Figure 2.16: If only a failure plane in orientation R′ is present, the Mohr circle has to be shifted further to the left until the effective normal stress $\sigma'_{\text{R}'}$ of stress state R′ is equal to the effective normal stress of the failure curve $\sigma'_{\text{R}',\text{fc}}$ for the same τ.

If only a failure plane in the orientation of point R′ in Figure 2.16 is present, a higher increase

in pore pressure is required to initiate shear failure (i.e. the Mohr Circle has to be shifted further to the left). For such a case, the pressure margin p_{shear} can be defined as the difference between the effective normal stress $\sigma'_{\mathrm{R}'}$ for the orientation R′ and the corresponding $\sigma'_{\mathrm{R}',\,\mathrm{fc}}$ of the failure curve for the same τ:

$$p_{\mathrm{shear}} = \sigma'_{\mathrm{R}'} - \sigma'_{\mathrm{R}',\,\mathrm{fc}} \tag{2.89}$$

with

$$\sigma'_{\mathrm{R}'} = \sigma'_{\mathrm{m}} + \tau_{\mathrm{m}} \cos 2\theta \tag{2.90}$$

and

$$\sigma'_{\mathrm{R}',\,\mathrm{fc}} = \frac{\tau_{\mathrm{s}} - c}{\tan \beta_{\mathrm{frict}}} = \frac{\tau_{\mathrm{m}} \sin 2\theta - c}{\tan \beta_{\mathrm{frict}}} \tag{2.91}$$

Please note that this criterion depends both on the friction angle β_{frict} and the fault angle θ. For the worst case assumption however the criterion is only a function of the friction angle β_{frict} and fault angle θ in the orientation P can be calculated from

$$\theta = (90 + \beta_{\mathrm{frict}})/2. \tag{2.92}$$

One could increase the pore pressure to a point where it matches or even surpasses the least compressive principal stress σ_2. Thus, the stress state in this direction would shift from compressive to tensile. Most rocks have a rather low tensile strength of only a few Megapascals (in contrast to a compressive strength in the order of several hundred Megapascals) (Lockner, 2013). In combination with the fact, that a reasonably sized rock volume will contain pre-existing flaws that have a tensile strength near zero (Zoback, 2007), it is safe to assume that tensile failure would occur as soon as the effective pore pressure p_{eff} surpasses the least compressive principal stress σ_2. Similar to shear failure, a pressure margin calculated from the difference of the two can be formulated:

$$p_{\mathrm{tensile}} = p_{\mathrm{eff}} - \sigma_2. \tag{2.93}$$

Tensile failure occurs, when this pressure margin becomes positive. Rutqvist et al. (2008) used such a formulation to evaluate the potential of tensile failure for a CO_2 injection scenario.
The answer to the question of how these derivations have to be adapted to use them in three dimensions is remarkably simple: Figure 2.17 illustrates that for the considerations on shear failure, only the maximal and minimal shear stress σ_1 and σ_3 matter. The intermediate principal stress σ_2 is irrelevant for the failure evaluation. Thus, in three dimensions all previously derived equations are applicable, if σ_2 is replaced by σ_3.

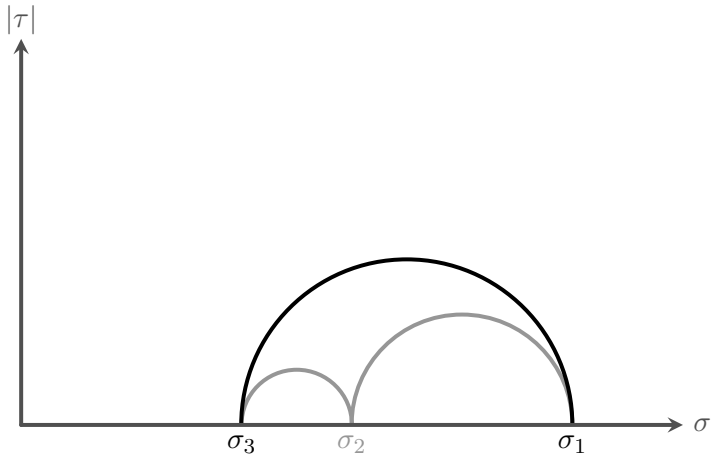

Figure 2.17: The Mohr circle in three dimensions: It becomes clear that for the previously presented considerations, the intermediate principal stressσ_2 is irrelevant and all previously derived equations are applicable, if σ_2 is replaced by σ_3.

2.4 Summary

This chapter described the fundamental physical concepts needed for the description of flow and mechanics in porous media. The introduction of terms and concepts for the characterisation of porous media and the flow processes occurring within them was followed by a section on rock mechanics. These concepts were then combined in the section on poroelasticity, where the focus lay on how fluids and their movement within the pores affects the mechanical behaviour of a rock and vice versa.

The next chapter will cover how these physical concepts can be transferred into a mathematical model and discuss different solution strategies for the derived coupled balance equations for flow and geomechanics in porous media.

3 Modelling flow and geomechanics in porous media

Numerical simulations are a powerful tool to study the processes of flow and geomechanics in porous media. This is especially true for problems where no analytical solutions exist. First, this chapter will outline how the physical concepts described in the previous section can be incorporated into a mathematical model to allow for such simulations. This is done by means of balancing the quantities mass and momentum.
The resulting system of non-linear partial differential equations will be tackled numerically. The sections on the spatial and temporal discretisation will cover how the continuous variables and equations can by approximated by their discrete counterparts.
This lays the groundwork to discuss different strategies for solving the coupled discrete equations of flow and geomechanics within porous media, which will be the focus of this chapter. The classical approaches fall into two categories: *Fully-coupled* and *sequential* methods. While different labels for these schemes exist, as stated in White et al. (2016), the differences are clear: The unknowns of flow and geomechanics are either solved simultaneously for one time-step (also termed *fully-coupled* or *monolithic*) or iteratively by splitting up the coupled problem into two (or more) sub-problems, which are then solved sequentially.
Stability and accuracy of the fully-coupled scheme are set against its higher computational cost (Settari et al., 2001). The ill-conditioned nature of the fully-coupled system has been tackled by using pre-conditioning (White and Borja, 2011), but the efficiency gain remains a key argument for the use of sequential methods. In addition, the ability to combine separate simulators for flow and geomechanics often serves as a motivation for applying such schemes. e.g. by linking the TOUGH multi-phase fluid and heat transport codes with the commercial FLAC3D geomechanical simulator as described in Rutqvist et al. (2002). But to ensure stability and convergence, an elaborate splitting scheme for flow and geomechanics is needed. Kim et al. (2011a), Kim et al. (2011b) and Mikelić and Wheeler (2013) studied the different splitting schemes in detail. Among the investigated strategies, the *undrained split* and the *fixed-stress split* are preferable due to their convergence behaviour and stability. The fixed-scheme has also been applied to couple flow in unsaturated porous media modelled by the Richards equation with linear elasticity (Both et al., 2018).

Beside the fully-coupled and sequential schemes, simplified representations of the flow and geomechanics interaction exist, where the pore compressibility (see Equation 2.63-2.65) is used to account for the increase in pore volume as a result of increased pore pressures. With this simplification, the pressure evolution and the storage capacity for CO_2 injections has been studied using the TOUGH2 simulator (e.g. Birkholzer et al., 2009; Zhou et al., 2008) as well as the geomechancial impact of injections in the context hydraulic fracturing (Rutqvist et al., 2013) and CO_2 storage (Rinaldi et al., 2014) with the TOUGH-FLAC code.
In summary, quite a selection of simulation strategies is available, which were developed with different mind-sets: Methods like the fixed-stress split certainly belong to the elaborate end of the spectrum requiring mathematical and numerical complexity in the solution approach while software tools such as TOUGH-FLAC certainly were designed rather pragmatically and optimized for practicability. This leads to the question that drives the numerical examples of the chapter: How would a sophisticated sequential method such as the fixed-stress scheme compare against a fully-coupled implementation and a TOUGH-FLAC-like model using the pore compressibility? Test cases of relevance for practical applications will be presented to test whether the fully-coupled approach is preferable in terms of efficiency and accuracy as stated in the first hypothesis in the introduction of this work.

3.1 Balance equations

3.1.1 Mass balance equations

A mass balance equation describes mathematically that the mass within a system is conserved. With respect to fluid flow in porous media, the mass balance equation expresses that the mass in the system can only change by fluxes over the system's boundaries or by sources or sinks within the system. In other words: The sum of the mass stored in the system, the accumulated fluxes over the boundaries and the contribution by sources and sinks equals zero. For a phase in a two-phase flow system, this can be expressed as:

$$\frac{\partial\left(\phi S_\alpha \varrho_\alpha\right)}{\partial t} + \operatorname{div}(\varrho_\alpha \boldsymbol{v_\alpha}) + q_\alpha = 0, \quad \alpha \in \{\mathrm{w}, \mathrm{n}\}. \tag{3.1}$$

The first term with ϕ as the porosity, ϱ_α as the density and S_α the saturation of a phase α represents the storage term, the second term with $\boldsymbol{v_\alpha}$ as the velocity of a phase α is the flux term and the sources and sinks of a phase α are denoted by q_α. For the velocity of a phase α, Darcy's Law (see Subsection 2.1.9) is used:

$$\boldsymbol{v}_{\mathrm{D},\,\alpha} = -\frac{k_{\mathrm{r}\alpha}}{\mu_\alpha}\,\mathbf{K}\left(\operatorname{grad} p_\alpha - \varrho_\alpha\,\boldsymbol{g}\right) \tag{2.16 revisited}$$

Inserting this for the velocities in the mass balance equation gives

$$\frac{\partial(\phi\rho_\alpha S_\alpha)}{\partial t} - \operatorname{div}\left\{\rho_\alpha \frac{k_{\mathrm{r}\alpha}}{\mu_\alpha}\,\mathbf{K}\,(\operatorname{grad} p_\alpha - \rho_\alpha\,\mathbf{g})\right\} + q_\alpha = 0 \quad ,\ \alpha \in \{\mathrm{w},\mathrm{n}\}. \tag{3.2}$$

Strictly speaking, by inserting Darcy's law, the equation became a combined mass and momentum balance equation since Darcy's law is a momentum balance equation.
Furthermore, Section 2.3 outlined how porosity and permeability change for deformable porous media. Using these considerations, a balance equation that takes the effect of poroelasticity into account can be formulated for each phase:

$$\frac{\partial(\phi_{\mathrm{eff}}\rho_\alpha S_\alpha)}{\partial t} - \operatorname{div}\left\{\rho_\alpha \frac{k_{\mathrm{r}\alpha}}{\mu_\alpha}\,\mathbf{K}_{\mathrm{eff}}\,(\operatorname{grad} p_\alpha - \varrho_\alpha\,\mathbf{g})\right\} + q_\alpha = 0 \quad ,\ \alpha \in \{\mathrm{w},\mathrm{n}\}. \tag{3.3}$$

If the porosity is considered to be a function of the pressure, the effective porosity ϕ_{eff} can be calculated from Equation 2.65 and the change in porosity in turn determines the change in permeability (e.g. Equation 2.69 or 2.70).
In contrast, a dependence of the porosity on the volumetric strain (Equation 2.61b) introduces the displacements as additional unknowns. This necessitates the formulation of a momentum balance equation for the rock matrix, which will be derived in the following.

3.1.2 Momentum balance equation

The conservation of momentum can be expressed as

$$\operatorname{div}\boldsymbol{\sigma} + \varrho\,\mathbf{g} = 0 \tag{3.4}$$

under the assumption that all time derivatives are negligibly small as a result of quasi-static conditions. In general, $\mathbf{g}$ accounts for all of the body forces but is simplified to the gravity vector here.
For a porous medium, a bulk density ϱ_{b} can be calculated from the weighted densities of the wetting and non-wetting phases ϱ_{w} and ϱ_{n} and the rock matrix ϱ_{rm}:

$$\varrho_{\mathrm{b}} = \phi\,(S_{\mathrm{w}}p_{\mathrm{w}} + S_{\mathrm{n}}p_{\mathrm{n}}) + (1-\phi)\,\varrho_{\mathrm{rm}} \tag{3.5}$$

Section 2.3 defined the effective stress tensor $\boldsymbol{\sigma'}$ taking the contribution of the pore pressure p into account:

$$\boldsymbol{\sigma'} = \boldsymbol{\sigma} - p\,\mathbf{I} \tag{2.47 revisited}$$

For the pore pressure p, the effective pore pressure p_{eff} is used:

$$p_{\text{eff}} = S_{\text{w}} p_{\text{w}} + S_{\text{n}} p_{\text{n}} \qquad \text{(2.49 revisited)}$$

With this, Equation 3.4 becomes

$$\text{div}\ (\boldsymbol{\sigma'} + p_{\text{eff}}\,\mathbf{I}) + \varrho_{\text{b}}\,\mathbf{g} = 0 \tag{3.6}$$

This momentum balance equation can be linearised by subtracting the initial state (denoted by the subscript 0) for effective stress, effective pressure and the bulk density:

$$\Delta\boldsymbol{\sigma'} = \quad \boldsymbol{\sigma'} - \boldsymbol{\sigma'_0} \tag{3.7}$$

$$\Delta p_{\text{eff}} = \quad p_{\text{eff}} - p_{\text{eff},0} \tag{3.8}$$

$$\Delta\varrho_{\text{b}} = \quad \varrho_{\text{b}} - \varrho_{\text{b},0} \tag{3.9}$$

This gives

$$\text{div}(\Delta\boldsymbol{\sigma'} + \Delta p_{\text{eff}}\,\mathbf{I}) - \Delta\varrho_{\text{b}}\mathbf{g} = 0. \tag{3.10}$$

Under the assumption of small porosity changes ($\Delta\phi \approx 0$, $\Delta(1-\phi) \approx 0$) and a constant density of the rock matrix ($\Delta\varrho_{\text{rm}} \approx 0$), the bulk density change becomes

$$\begin{aligned}\Delta\varrho_{\text{b}} &= \Delta\phi(S_{\text{w}}\varrho_{\text{w}} + S_{\text{n}}\varrho_{\text{n}}) + \phi\Delta(S_{\text{w}}\varrho_{\text{w}} + S_{\text{n}}\varrho_{\text{n}}) \\ &\quad + \Delta(1-\phi)\varrho_s + (1-\phi)\Delta\varrho_s \\ &\approx \phi\Delta(S_{\text{w}}\varrho_{\text{w}} + S_{\text{n}}\varrho_{\text{n}})\end{aligned} \tag{3.11}$$

and further simplifies to

$$\Delta\varrho_{\text{b}} \approx \phi\,(\Delta S_{\text{n}}(\varrho_{\text{n}} - \varrho_{\text{w}}) + S_{\text{n}}\Delta\varrho_{\text{n}})\,. \tag{3.12}$$

assuming small changes in ϱ_{n} while $\Delta\varrho_{\text{w}}$ of a possibly compressible non-wetting phase is taken into account. With these simplifications, one arrives at

$$\text{div}(\Delta\boldsymbol{\sigma'} + \Delta p_{\text{eff}}\,\mathbf{I}) + \phi\ (\Delta S_{\text{n}}(\varrho_{\text{n}} - \varrho_{\text{w}}) + S_{\text{n}}\Delta\varrho_{\text{n}})\,.\,\mathbf{g} = 0. \tag{3.13}$$

for the momentum balance of the solid. Darcis (2013) states that the use of the linearised momentum balance equation over the full momentum balance allows for an easier application of initial and boundary conditions.

3.1.3 Constitutive equations and supplementary constraints

To close the system, the following constitutive equations and constraints are used:

- The strain $\boldsymbol{\epsilon}$ is derived from the displacement vector $\boldsymbol{u}$ as follows

$$\boldsymbol{\epsilon} = \frac{1}{2}(\operatorname{grad} \boldsymbol{u} + \operatorname{grad}^{\mathrm{T}} \boldsymbol{u}). \qquad \text{(2.36 revisited)}$$

- Linear elastic behaviour of the rock is assumed. The Young's modulus E and Poisson's ratio ν are used as elastic constants (for details, see Equation 2.39).

- The sum of the fluid saturations adds up to one

$$\sum_{\alpha} S_{\alpha} = 1. \qquad \text{(2.3 revisited)}$$

- The pressures are connected via the capillary pressure (calculated here according to the relation by van Genuchten (1980))

$$p_{\mathrm{c}} = \frac{1}{\alpha_{\mathrm{VG}}} \left(S_{\mathrm{e}}^{-1/m_{\mathrm{VG}}} - 1 \right)^{.1/n_{\mathrm{VG}}}$$
$$\text{with } S_{\mathrm{e}} = \frac{S_{\mathrm{w}} - S_{\mathrm{rw}}}{1 - S_{\mathrm{rw}}} \qquad \text{(2.7, 2.8 revisited)}$$

- The Van-Genuchten formulation is also used for the relative permeability:

$$k_{\mathrm{rw}} = \sqrt{S_{\mathrm{e}}} \left(1 - \left(1 - S_{\mathrm{e}}^{1/m} \right)^{m} \right)^{2},$$
$$k_{\mathrm{rn}} = (1 - S_{\mathrm{e}})^{1/3} \left(1 - S_{\mathrm{e}}^{1/m} \right)^{2m} \qquad \text{(2.13 revisited)}$$

The balance equations of the two fluid phases describe the fluid phases' pressure and saturation distribution, but also depend on the deformation of the rock matrix by means of the effective porosity and permeability. The momentum balance equation allows to determine the deformation resulting from a given pore pressure. Together with the constitutive equations and supplementary constraints, these balance equations give a system of non-linear partial differential equations (PDEs) that describe the interaction of flow and geomechanics in porous media.

For two phases, using the sum of the saturations and capillary pressure-saturation relationship (Equation 2.3 and Equation 2.8) allow to reduce the unknowns of the balance equations of the fluid phases to the pressure of the wetting phase p_{w} and the saturation of the non-wetting

phase S_n. Other combinations, e.g. p_w-p_n or S_w-S_n are also possible. Disadvantages and restrictions of these combinations are discussed in Helmig (1997).
The displacement vector field $\boldsymbol{u}$ is chosen as the primary variable of the momentum balance equation.
The complexity of the intended applications requires to tackle these equations numerically. The following sections will cover the spatial and temporal discretisation of the balance equations.

3.2 Spatial discretisation

The balance equations presented in the previous section have the form

$$\frac{\partial \mathbf{s}(\boldsymbol{w})}{\partial t} + \operatorname{div}\left(\mathbf{f}(\boldsymbol{w})\right) + q(\boldsymbol{w}) = 0 \tag{3.14}$$

accounting for the storage $s(\boldsymbol{w})$, the fluxes $\mathbf{f}(\boldsymbol{w})$ and the sources and sinks $q(\boldsymbol{w})$ for a vector of primary variables $\boldsymbol{w}$. Boundary conditions can be applied in the form of Neumann boundary conditions prescribing a flux or by Dirichlet boundary conditions setting the unknown $\boldsymbol{w}$ to a specific value. The model domain is then subdivided into a mesh of discrete, non-overlapping elements. The sum of the discrete values $\hat{\boldsymbol{w}}_i$ at the nodes of the mesh multiplied with the corresponding basis functions N_i give the trial solution $\tilde{\boldsymbol{w}}$

$$\tilde{\boldsymbol{w}} = \sum_{i=0}^{m} N_i \, \hat{\boldsymbol{w}}_i \tag{3.15}$$

with m as the number of nodes. One can also define the gradient of a primary variable $\tilde{w}$ as

$$\operatorname{grad} \tilde{w} = \sum_{i=0}^{m} \operatorname{grad} N_i \cdot \hat{w}_i. \tag{3.16}$$

In Equation 3.14, $\boldsymbol{w}$ is replaced by the interpolated $\tilde{\boldsymbol{w}}$ and the equation is multiplied with any weighting function W_j. After integrating over the model domain Ω, one obtains

$$\int_\Omega W_j \, \frac{\partial \mathbf{s}(\tilde{\boldsymbol{w}})}{\partial t} \, \mathrm{d}\Omega + \int_\Omega W_j \operatorname{div}\left(\mathbf{f}(\tilde{\boldsymbol{w}})\right) \mathrm{d}\Omega + \int_\Omega W_j \, q(\tilde{\boldsymbol{w}}) \, \mathrm{d}\Omega = 0 \tag{3.17}$$

With the box method and the standard Galerkin finite element method, two variants of the general balance equation, that exhibit different combinations of the basis functions N_i and the weighing functions W_j, will be presented in the following.

3.2.1 Box method

For the box method described in Helmig (1997), a control volume is assigned to each node of the mesh. The edges of these *boxes* are defined by the centre of gravity of the elements and by the midpoint of the elements' faces. First-order Lagrangian polynomials are used for the basis functions N_i. The weighting functions are chosen as piecewise constant functions, being 1 within the associated box and 0 everywhere else (see also Figure 3.1a):

$$W_j(x) = \begin{cases} 1 & \text{if} \quad x \in B_j \\ 0 & \text{if} \quad x \notin B_j \end{cases} \tag{3.18}$$

As a result, the integrals over Ω in Equation 3.17 become integrals evaluated for each of the boxes B_j. Additionally applying the divergence theorem transforms Equation 3.17 into

$$\int_{B_j} \frac{\partial \mathbf{s}(\tilde{\boldsymbol{w}})}{\partial t} + \int_{\Gamma_{B_j}} \mathbf{f}(\tilde{\boldsymbol{w}}) \cdot \mathbf{n} \, \mathrm{d}\Gamma_{B_j} + \int_{B_j} q(\tilde{\boldsymbol{w}}) = 0 \tag{3.19}$$

with Γ_{B_j} as the surface of a box B_j.

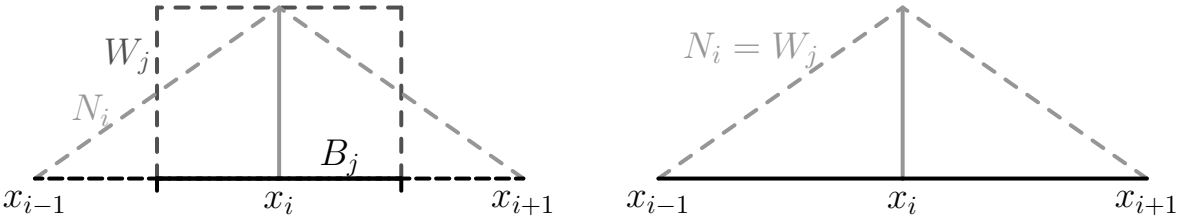

(a) Box method: Linear basis function and piecewise constant weighting functions for a box B_j.

(b) Standard Galerkin finite element method: The basis functions and weighting functions are chosen to be equal.

Figure 3.1: Weighting functions and basis functions for the presented methods.

For the storage term and the source and sink term in Equation 3.19, the mass is lumped to the node, which helps to avoid non-physical oscillations (Celia and Binning, 1992). In detail, these terms are considered to be only a function of the primary variable $\hat{w}_j$ at the respective node and independent of the contribution of all neighbouring nodes. Thus, the integrals can be simplified to the volume of the box V_j:

$$\int_{B_j} \frac{\partial \mathbf{s} \left(\sum_{i=0}^{n} N_i \, \hat{\boldsymbol{w}}_i \right)}{\partial t} \, \mathrm{d}B_j = V_j \, \frac{\partial \mathbf{s}(\hat{\boldsymbol{w}}_j)}{\partial t} \tag{3.20}$$

and

$$\int_{B_j} q \left(\sum_{i=0}^{n} N_i \, \hat{\boldsymbol{w}}_i \right) \mathrm{d}B_j = V_j \; q(\hat{\boldsymbol{w}}_j), \quad \text{for all } j \in \{0, ..., m\}. \tag{3.21}$$

The balance equation for a box B_j at the node i has then the form

$$V_j \frac{\partial \mathbf{s}(\hat{\boldsymbol{w}}_j)}{\partial t} + \int_{\Gamma_{B_j}} \mathbf{f}(\tilde{\boldsymbol{w}}) \cdot \mathbf{n} \, \mathrm{d}\Gamma_{B_j} + V_j \; q(\hat{\boldsymbol{w}}_j) = 0 \tag{3.22}$$

When the flux at a face is calculated, the *upwind scheme* takes the direction of the velocity $v_{i,i-1}$ into account to determine a quantity $\omega^{\mathrm{upw}}_{i,i-1}$ at interface between x_{i-1} and x_i, increasing the stability of the scheme:

$$\omega^{\mathrm{upw}}_{i,i-1} = \begin{cases} \omega_{i-1} & \text{if } v_{i,i-1} \cdot (x_{i-1} \text{ - } x_i) < 0 \\ \omega_i & \text{if } v_{i,i-1} \cdot (x_{i-1} \text{ - } x_i) \geq 0 \end{cases} \tag{3.23}$$

3.2.2 Standard Galerkin finite element method

For the standard Galerkin finite element method, the weighting functions are chosen to be equal to the basis functions (displayed in Figure 3.1b):

$$N_i = W_j \tag{3.24}$$

Combined with the divergence theorem, Equation 3.17 becomes

$$\int_\Omega N_i \frac{\partial \mathbf{s}(\tilde{\boldsymbol{w}})}{\partial t} \, \mathrm{d}\Omega + \int_{\Gamma_\Omega} N_i \, \mathbf{f}(\tilde{\boldsymbol{w}}) \cdot \mathbf{n} \, \mathrm{d}\Gamma_\Omega + \int_\Omega \operatorname{grad} N_i \, \mathbf{f}(\tilde{\boldsymbol{w}}) \, \mathrm{d}\Omega + \int_\Omega N_i \, q(\tilde{\boldsymbol{w}}) \, \mathrm{d}\Omega = 0 \tag{3.25}$$

where Γ_Ω is the surface of the Ω. The integrals are solved using the Gauss quadrature rule. Mass lumping can be applied here, too, resulting in a *Control Volume Finite Element Approach (CVFEM)* (Forsyth, 1991).

Using an equal-order approximation of the pressure and the solid displacement is known to create stability problems (Kim, 2010). To tackle this issue, a staggered grid approach was proposed by Kim (2010). Darcis (2013) avoided the encountered spurious pressure oscillations by discretising the balance equation of the fluid phases with the box method and the momentum balance equation with the standard Galerkin finite element method. This quasi-staggered approach allows for a nodal based approach without explicitly using staggered grids.

The upwind scheme is used for the mobility λ_α and the density ϱ_α in the balance equation for fluid phases.

3.3 Temporal discretisation

A fully implicit Euler scheme is used to replace the time differential ∂t by a backward difference approximation. With this, the balance equation discretised with the box method takes the form

$$V_j \frac{\mathbf{s}(\hat{\boldsymbol{w}}_j^n) - \mathbf{s}(\hat{\boldsymbol{w}}_j^{n-1})}{\Delta t^n} + \int_{\Gamma_{B_j}} \mathbf{f}(\tilde{\boldsymbol{w}}^n) \cdot \mathbf{n} \, \mathrm{d}\Gamma_{B_j} + V_j \; q(\hat{\boldsymbol{w}}_j^n) = 0 \tag{3.26}$$

with $n-1$ and n denoting time-step indices of two subsequent time-steps t^{n-1} and t^n.

3.4 Solution strategies

The combined mass and momentum balance equation for the fluid phases (Equation 3.2) contain the pressure of the wetting phase p_w and the saturation S_n of the non-wetting phase as unknowns. For convenience, the suffix "2p" will be used when referring to the two-phase equations.
The momentum balance equation of the solid (Equation 3.13) is solved for the displacement vector $\hat{\boldsymbol{u}}$ and referred to as "el".
One can combine both balance equations and construe their left side as a residual vector $\boldsymbol{r}(\hat{\boldsymbol{w}}^{n-1}, \hat{\boldsymbol{w}}^n)$ with the components $\boldsymbol{r}_\mathrm{2p}$ and $\boldsymbol{r}_\mathrm{el}$ for the two-phase flow and the elastic momentum balance equation:

$$\boldsymbol{r}(\hat{\boldsymbol{w}}^{n-1}, \hat{\boldsymbol{w}}^n) = \begin{bmatrix} \boldsymbol{r}_\mathrm{2p} \\ \boldsymbol{r}_\mathrm{el} \end{bmatrix} = 0 \tag{3.27}$$

Here, the residual vector $\boldsymbol{r}(\hat{\boldsymbol{w}}^{n-1}, \hat{\boldsymbol{w}}^n)$ is a function of the solution vectors $\hat{\boldsymbol{w}}^{n-1}$ and $\hat{\boldsymbol{w}}^n$ of two subsequent time-steps t^{n-1} and t^n. Both solution vectors (exemplarily written here for $\hat{\boldsymbol{w}}^n$) encompass a 2p-portion $\hat{\boldsymbol{w}}_\mathrm{2p}^n$ with $\hat{\boldsymbol{p}}_\mathrm{w}^n$ and $\hat{\boldsymbol{S}}_\mathrm{n}^n$ and an elastic portion $\hat{\boldsymbol{w}}_\mathrm{el}^n$ with $\hat{\boldsymbol{u}}^n$:

$$\hat{\boldsymbol{w}}^n = \begin{bmatrix} \hat{\boldsymbol{w}}_\mathrm{2p}^n \\ \hat{\boldsymbol{w}}_\mathrm{el}^n \end{bmatrix} \tag{3.28}$$

with

$$\hat{\boldsymbol{w}}_\mathrm{2p}^n = \begin{bmatrix} \hat{\boldsymbol{p}}_\mathrm{w} \\ \boldsymbol{S}_\mathrm{n} \end{bmatrix}^n \text{ and } \hat{\boldsymbol{w}}_\mathrm{el}^n = \hat{\boldsymbol{u}}^n. \tag{3.29}$$

As this system of residual equations exhibits a non-linear behaviour, a Newton scheme is used to drive the residual to zero. For the k-th iteration, $\hat{\boldsymbol{w}}^{n,k}$ is the k-th estimate of the solution at time t^n. To determine the new solution for $k+1$, the Jacobian matrix $\mathbf{J}^k$ is used. Here, $\mathbf{J}^k$

is the matrix of all first-order derivatives of the residual vector at the k-th iteration:

$$\mathbf{J}^k = \left(\frac{\partial \boldsymbol{r}}{\partial \hat{\boldsymbol{w}}} \right)^k \tag{3.30}$$

The new solution vector $\hat{\boldsymbol{w}}^{n,k+1}$ is then determined by solving

$$\mathbf{J}^k \Delta \hat{\boldsymbol{w}} = -\boldsymbol{r}^k \tag{3.31}$$

and by adding the update $\Delta \hat{\boldsymbol{w}}$ to the previous solution vector $\hat{\boldsymbol{w}}^{n,k}$

$$\hat{\boldsymbol{w}}^{n,k+1} = \hat{\boldsymbol{w}}^{n,k} + \Delta \hat{\boldsymbol{w}}. \tag{3.32}$$

Equation 3.27 describes the block-wise structure of residual vector $\boldsymbol{r}$. In the same sense, the Jacobian system solved in each Newton update can be expressed as

$$\begin{bmatrix} \mathbf{J}_{\mathrm{2p,2p}} & \mathbf{J}_{\mathrm{2p,el}} \\ \mathbf{J}_{\mathrm{el,2p}} & \mathbf{J}_{\mathrm{el,el}} \end{bmatrix}^k \begin{bmatrix} \Delta \hat{\boldsymbol{w}}_{\mathrm{2p}} \\ \Delta \hat{\boldsymbol{w}}_{\mathrm{el}} \end{bmatrix} = - \begin{bmatrix} \boldsymbol{r}_{\mathrm{2p}} \\ \boldsymbol{r}_{\mathrm{el}} \end{bmatrix}^k, \tag{3.33}$$

where $\mathbf{J}_{\boldsymbol{a},\boldsymbol{b}}$ is balance equation $\boldsymbol{a}$ differentiated with respect to solution vector $\boldsymbol{b}$. As an example, $\mathbf{J}_{\mathrm{2p,2p}}$ is the derivative of the mass and momentum balance equation for the fluid with respect to $\hat{\boldsymbol{p}}_{\mathrm{w}}$ and $\boldsymbol{S}_{\mathrm{n}}$. The components $\mathbf{J}_{\mathrm{2p,el}}$ and $\mathbf{J}_{\mathrm{el,2p}}$ account for the flow-geomechanics coupling.

3.4.1 Fully-coupled scheme

Within the fully-coupled scheme, the unknowns p_{w} and S_{n} for the two-phase flow and $\hat{\boldsymbol{u}}$ for the geomechanics are solved simultaneously for each time-step. This means that each Newton update is computed from the linear system in Equation 3.33. The use of the full matrix $\mathbf{J}$ explains why this scheme is also often referred to as *monolithic*.

3.4.2 Fixed-stress scheme

A scheme where the unknowns for flow and geomechanics are solved sequentially requires to split up the full problem into a flow and geomechanics sub-problem. One starts with the flow problem and then continues with solving the geomechanics. This routine will be referred to as a *coupling step*. Several of these coupling steps make up an iterative scheme.
The simplest version of such an iterative coupling would be to just transfer p_{w} and S_{n} to the mechanics, and to insert the stresses and strains back into the flow problem in the next

iteration. Unfortunately, this *drained-split* scheme is only conditionally stable while the *fixed-stress* split, in turn, is an unconditionally stable scheme (Kim et al., 2011a; Mikelić and Wheeler, 2013). As the name implies, the stress is assumed to be constant, or, to be more precise, the difference between the volumetric stress of the flow problem $\sigma_{\mathrm{v,\,2p}}^{n,i}$ and the volumetric stress $\sigma_{\mathrm{v,\,el}}^{n,\,i-1}$ of the previous geomechanical solution is zero:

$$\sigma_{\mathrm{v,\,el}}^{n,\,i-1} - \sigma_{\mathrm{v,\,2p}}^{n,\,i} = 0. \tag{3.34}$$

Here, i is the index of the coupling step. Since such a coupling step was defined to start with the flow problem, the last geomechanical solution was obtained in the previous coupling step and thus is denoted with the index $i-1$.
For the geomechanical problem, the pressure of the previous flow problem is prescribed, so $p_{\mathrm{el}}^{n,\,i}$ and $p_{\mathrm{2p}}^{n,\,i}$ are equal within a coupling step i:

$$p_{\mathrm{el}}^{n,\,i} = p_{\mathrm{2p}}^{n,\,i}. \tag{3.35}$$

Thus, one can express Equation 3.34 by the pressures $p_{\mathrm{2p}}^{n,\,i}$ and $p_{\mathrm{2p}}^{n,\,i-1}$ and the volumetric strains $\epsilon_{\mathrm{v,\,2p}}^{n,\,i}$ and $\epsilon_{\mathrm{v,\,el}}^{n,\,i-1}$,

$$(K_{\mathrm{dr}}\ \epsilon_{\mathrm{v,\,el}}^{n,\,i-1} -\ p_{\mathrm{2p}}^{n,\,i-1}) - (K_{\mathrm{dr}}\ \epsilon_{\mathrm{v,\,2p}}^{n,\,i} -\ p_{\mathrm{2p}}^{n,\,i}) = 0. \tag{3.36}$$

Here, K_{dr} is the drained bulk modulus and the Biot coefficient α is assumed to be 1.
The coupling within the flow part arises from the dependence of the porosity on the volumetric strain (Equation 2.61b). With Equation 3.36 one can formulate the flow problem independent of the current displacement vector $\boldsymbol{u}$ by calculating the volumetric strain $\epsilon_{\mathrm{v,2p}}^{n,\,i}$ of the flow problem in the current coupling step i from the pressure difference $p_{\mathrm{2p}}^{n,\,i} - p_{\mathrm{2p}}^{n,\,i-1}$ of the current and the previous coupling step of the flow problem and from the volumetric strain $\epsilon_{\mathrm{v,el}}^{n,\,i-1}$ determined in the previous coupling step for the geomechanics:

$$\epsilon_{\mathrm{v,\,2p}}^{n,\,i} = -\frac{1}{K_{dr}}(p_{\mathrm{2p}}^{n,\,i} - p_{\mathrm{2p}}^{n,\,i-1}) + \epsilon_{\mathrm{v,\,el}}^{n,\,i-1}. \tag{3.37}$$

For the two-phase system, the mass and momentum balance then depends on the primary variables $p_{\mathrm{w}}^{n,\,i}$ and $S_{\mathrm{n}}^{n,\,i}$, as the pressure p becomes the effective pressure p_{eff}

$$p_{\mathrm{eff}} = S_{\mathrm{w}} p_{\mathrm{w}} + S_{\mathrm{n}} p_{\mathrm{n}}. \tag{2.49 revisited}$$

After solving the flow problem altered by the fixed-stress assumption, $p_{\mathrm{w}}^{n,\,i}$ and $S_{\mathrm{n}}^{n,\,i}$ are inserted into the momentum balance of the geomechanics, where only the displacement vector $\mathbf{u}^{n,\,i}$ remains as the primary variable. With this, two separate Jacobian systems can be formulated,

which are solved sequentially:

$$\left[\tilde{\mathbf{J}}_{2\mathrm{p},2\mathrm{p}}\right]^k \begin{bmatrix}\hat{\boldsymbol{p}}_{\mathrm{w}} \\ \hat{\boldsymbol{S}}_{\mathrm{n}}\end{bmatrix} = -\left[\boldsymbol{r}_{2\mathrm{p}}\right]^k . \tag{3.38}$$

$$\left[\tilde{\mathbf{J}}_{\mathrm{el},\mathrm{el}}\right]^k [\hat{\boldsymbol{u}}] = -\left[\boldsymbol{r}_{\mathrm{el}}\right]^k . \tag{3.39}$$

Here, $\tilde{\mathbf{J}}_{2\mathrm{p},2\mathrm{p}}$ and $\tilde{\mathbf{J}}_{\mathrm{el},\mathrm{el}}$ denote the derivatives of the modified balance equations: $\tilde{\mathbf{J}}_{2\mathrm{p},2\mathrm{p}}$ contains the fixed-stress assumption, so the volumetric strain of the current coupling step i and the current Newton iteration k for a time-step n is calculated from

$$\epsilon_{\mathrm{v},\,2\mathrm{p}}^{n,\,i,\,k} = -\frac{1}{K_{dr}}(p_{\mathrm{eff},\,2\mathrm{p}}^{n,\,i,\,k} - p_{\mathrm{eff},\,2\mathrm{p}}^{n,\,i-1}) + \epsilon_{\mathrm{v},\,\mathrm{el}}^{n,\,i-1} \tag{3.40}$$

and the effective pressure values from the flow problem are prescribed within $\tilde{\mathbf{J}}_{\mathrm{el},\mathrm{el}}$. When the porosity update is calculated using Equation 2.62, it is worth noting that a fixed-stress split with just one coupling step is identical to a calculation of the porosity change from the pore compressibility (cf. Equation 2.65): The previous coupling step becomes the previous time-step for zero iterations. Thus, $\epsilon_{\mathrm{v}}^{i-1}$ is equal to zero for the first time-step and dependent only on the pressure difference between the previous and the current time-step for all following time-steps. As these collapse to the difference between the initial and the current pressure, this simplified sequential scheme becomes equivalent to using the pore compressibility or the drained bulk modulus, respectively:

$$\begin{aligned}
\phi_{\mathrm{eff}}^{n} &= \phi_0 - \epsilon_{\mathrm{v}} \\
&= \phi_0 + \frac{1}{K_{dr}}(p_{\mathrm{eff},\,2\mathrm{p}}^{n} - p_{\mathrm{eff},\,2\mathrm{p}}^{n-1}) - \epsilon_{\mathrm{v},\,\mathrm{el}}^{n-1} \\
&= \phi_0 + \frac{1}{K_{dr}}(p_{\mathrm{eff},\,2\mathrm{p}}^{n} - p_{\mathrm{eff},\,2\mathrm{p}}^{n-1}) + \frac{1}{K_{dr}}(p_{\mathrm{eff},\,2\mathrm{p}}^{n-1} - p_{\mathrm{eff},\,2\mathrm{p}}^{n-2}) - \epsilon_{\mathrm{v},\,\mathrm{el}}^{n-2} \\
&= \phi_0 + \frac{1}{K_{dr}}(p_{\mathrm{eff},\,2\mathrm{p}}^{n} - p_{\mathrm{eff},\,2\mathrm{p}}^{n-2}) - \epsilon_{\mathrm{v},\,\mathrm{el}}^{n-2} \\
&\ldots \\
&= \phi_0 + \frac{1}{K_{dr}}(p_{\mathrm{eff},\,2\mathrm{p}}^{n} - p_{\mathrm{eff},\,2\mathrm{p}}^{0})
\end{aligned} \tag{3.41}$$

Figure 3.2 further illustrates the differences between the presented numerical coupling schemes. The top panel shows the numerical routine for the original version of TOUGH-FLAC (a sequential combination of the TOUGH2 multi-phase fluid and heat transport code with the commercial FLAC3D geomechanical simulator as described in Rutqvist et al., 2002), where the pore compressibility is used to calculate the porosity changes within the flow problem. At time t^n, the porosity is thus a function of the current effective pore pressure p_{eff}^n. Next, p_{w}^n

and S_{n}^{n} are transferred to the momentum balance equation to calculate the solution at time t^n. A feedback of the mechanics onto the flow can be achieved via the transfer of a permeability change Δk, which is used in the next flow time-step. If the permeability is constant, the mechanics are just a post-processing and the scheme will be referred to as a *zero-iteration case* in this work.

A more recent version of TOUGH-FLAC (Blanco-Martín et al., 2017) transfers a correction term for the porosity calculated using the fixed-stress assumption back into the flow problem (see Figure 3.2, middle). Again, this correction becomes active in the next time-step of the flow problem. Thus, the porosity within each flow time-step is a function of the current effective pore pressure p_{eff}^{n} and the volumetric strain of the previous time-step $\epsilon_{\mathrm{v,\,el}}^{n-1}$.

An iterative fixed-stress scheme repeats the coupling steps several times until convergence (see Figure 3.2, bottom). Within the flow problem, the volumetric strain $\epsilon_{\mathrm{v,\,2p}}^{n}$ is calculated from Equation 3.37. This implies two things: First, the porosity depends on the values of p_{eff}^{n} and $\epsilon_{\mathrm{v,\,2p}}^{n}$ of the current time-step (given at least one iteration is performed). And second, the approximated $\epsilon_{\mathrm{v,\,2p}}^{n}$ becomes $\epsilon_{\mathrm{v,\,el}}^{n}$ of the geomechanics when the iteration is continued until convergence.

In summary, the use of the pore compressibility and the subsequent solution of the mechanics represents the simplest scheme. It can be enriched by a feedback of the mechanics back onto the flow for the next time-step, be it via a permeability or a porosity update. A sophisticated iterative scheme requires to repeat the coupling step several times for each time-step. In this work, we will examine the end-members of the spectrum, so the first and the last scheme.

In contrast to the discretisation of the balance equations for two-phase flow in the fully-coupled approach by the box method, many well-established software codes such as Eclipse by Schlumberger or TOUGH2 by the Lawrence Berkeley National Laboratory (Pruess et al., 1999) use the cell-centered finite volume method (see e.g. Chen et al., 2006). The fixed-stress approach in this work can use both the box method and cell-centred finite volume method for the discretisation of the two-phase flow equations.

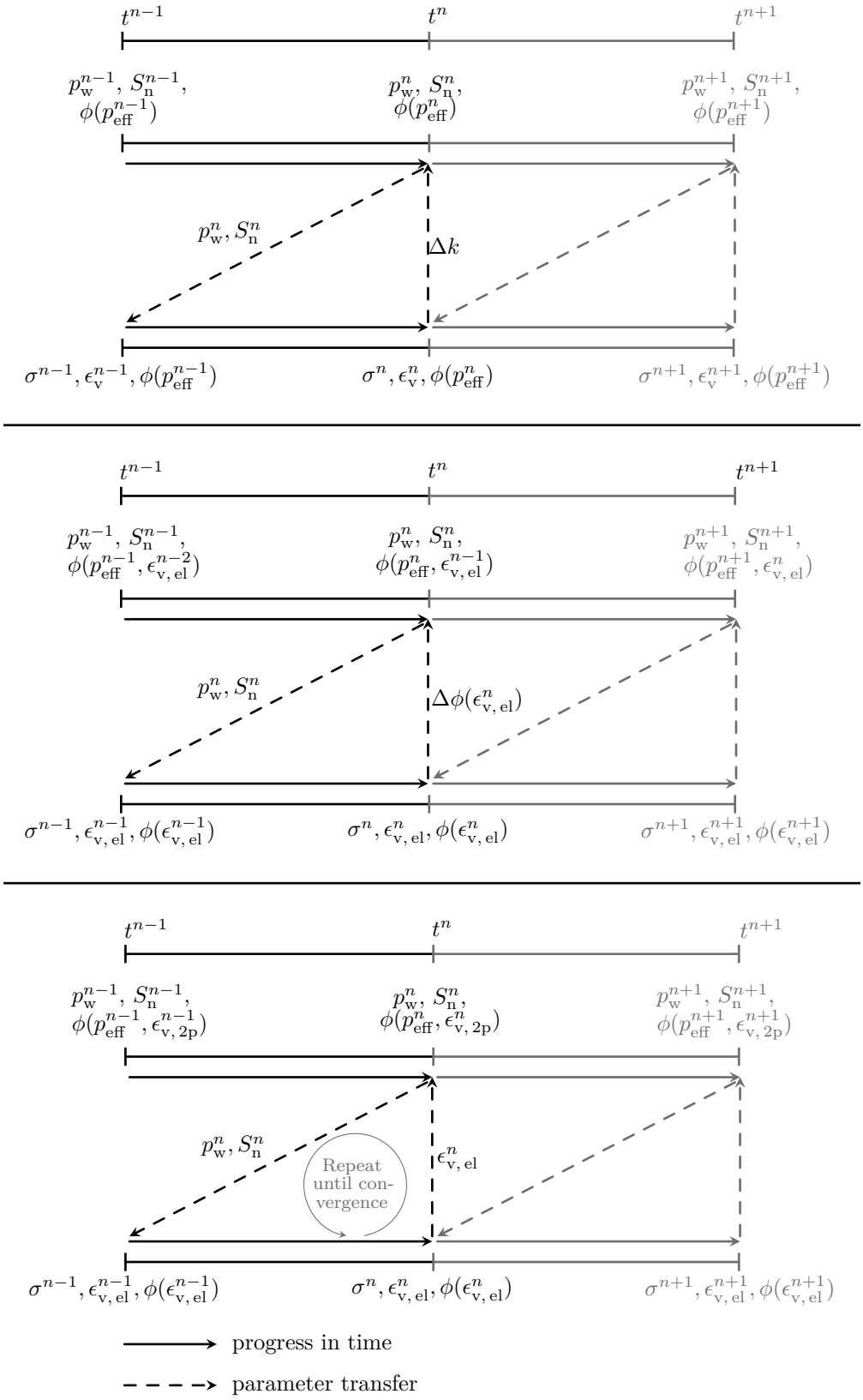

Figure 3.2: Numerical routine for the original version of TOUGH-FLAC using the pore compressibility (top), for the recent version using the fixed-stress assumption (middle) and for the iterative fixed-stress scheme as implemented in DuMu$^\mathrm{x}$ (bottom).

3.5 Simulation software

The simulations presented in the following were performed with the numerical toolbox DuMu^{x} (Flemisch et al., 2011; Ackermann et al., 2017; Fetzer et al., 2017). This open-source simulator for flow and transport processes in porous media is based on the Distributed and Unified Numerics Environment DUNE (Blatt et al., 2016; Blatt and Bastian, 2007; Bastian et al., 2008b,a). Except for the fully-coupled model, which was already implemented within the doctoral thesis of Darcis (2013), all models on top of DuMu^{x}and DUNE were developed within the scope of this work.
In the following, different numerical test cases will be presented to explore the applicability of the different modelling approaches for flow and geomechanics in porous media.

3.6 Homogeneous one-phase numerical test case

3.6.1 Scenario description

The first scenario is a water injection into a homogeneous, two-dimensional domain fully saturated with water. The domain is 2 km $\times$ 2 km in size and located at a depth of 500 m to 2500 m (see Figure 3.3, left).
The pressure distribution is hydrostatic, so it increases by 9.81 MPa per kilometre. For an atmospheric pressure of 0.1 MPa at the ground surface, this results in a pressure of 5 MPa at the top of the domain and 24.6 MPa at the bottom.
Assuming the injection takes place into an aquifer composed of sedimentary rock, e.g. of Berea Sandstone, the porosity is 0.1, the permeability is $1 \cdot 10^{-14}$ m^2 and the density is 2260 kg/m^3. For the porosity, it is certainly a value at the lower end of the range, but the density and permeability lie well within the reported data (e.g Churcher et al., 1991; Manger, 1963).
The Young's modulus is 5 GPa and the Poisson ratio 0.25. Compared to experimental values for Berea Sandstone published by Hart and Wang (1995), this represents a rather low Young's modulus. The Poisson ratio is in agreement with the experimental data.
The vertical stress gradient is calculated from the overburden density, for which 2260 kg/m^3 were chosen, too. A horizontal-over-vertical stress ratio of $R = \sigma_{\mathrm{h}}/\sigma_{\mathrm{v}} = 0.6$ is used consistent with observations by Cipolla et al. (2010). The temperature has a constant value of 35 °C. As visible in Figure 3.3 (right), the domain is refined horizontally around the injection. As this grid is later used to include a fault in the scenario, the grid already contains this feature and the according refinement. The injection of 0.2 kg/s takes place into the two cells with the centres (6.25, 2.5) and (6.25, -2.5) on the left of the domain.

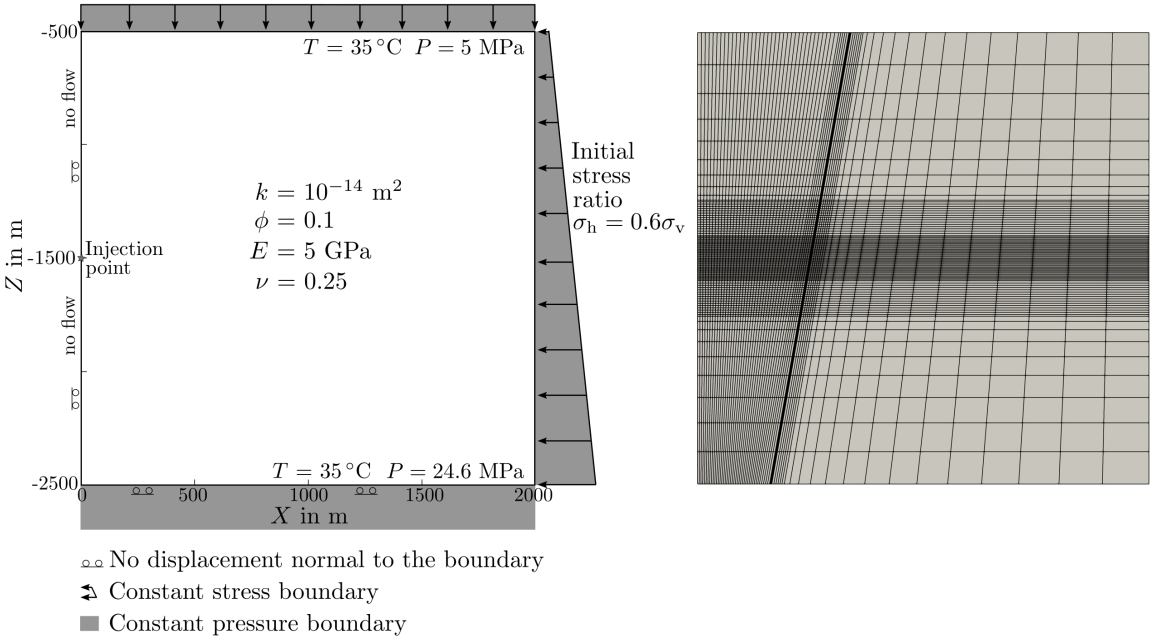

Figure 3.3: Set-up of the homogeneous one-phase test case (left) and domain discretisation (right).

The implementation of the different solution schemes in DuMu^{x} allows for an adaptive time stepping. Nonetheless, the time-steps were chosen to be the same for all schemes to achieve a better comparability. They are small at the beginning (starting with 8.64 seconds) and increase over the course of the simulation. For most cases, the time-step size is twice the previous one. Additional time steps are inserted to get simulation output for a specific time (usually multiples of a day).

3.6.2 Comparison with TOUGH-FLAC

The scenario is complex enough so the interaction of flow and geomechanics can be observed. At the same time, all features are well defined and easy to implement, so a comparison with other simulation codes is possible. Here, the simulation results obtained with DuMu^{x} will be compared to TOUGH-FLAC (a sequential combination of TOUGH2 multi-phase fluid and heat transport codes with the commercial FLAC3D geomechanical simulator as described in Rutqvist et al., 2002). As already mentioned, a fixed-stress approach using the cell-centred finite-volume method is used for the balance equation of the flow to match the discretisation of TOUGH2. For the geomechanics, both DuMu^{x} and FLAC3D use the finite-element method. The simulation output of TOUGH-FLAC was provided by Antonio Rinaldi from the ETH Zurich.

The first two plots of this scenario show the pressure evolution at the injection. In Figure 3.3a

the result of the whole simulation time of 1800 days is visible. The pressure increases rather fast, then slows down and reaches a plateau value once equilibrium of the injection and the outflow through the model boundaries is achieved. There is hardly any difference visible between the different datasets.
This changes when one focusses on the transient phase of the simulation: Figure 3.3b displays the pressure increase during the first 80 days. It becomes apparent that the different solution strategies indeed differ from each other: While the simulation with just one coupling step - or zero iterations following the definition in Subsection 3.4.2 - is in very good agreement with the results from TOUGH2 using the pore compressibility (see Equation 2.63-2.65), there is a notable difference to the results of a fixed-stress scheme that is iterated until no pressure change between the iterations occurs. The result of the latter most likely represents the physical behaviour better since the initial guess of the porosity from the pressure difference is corrected over the course of the iterations and becomes the more realistic porosity change resulting from the deformation. This will be explored in depth when the fixed-stress scheme is compared with the fully-coupled solution.

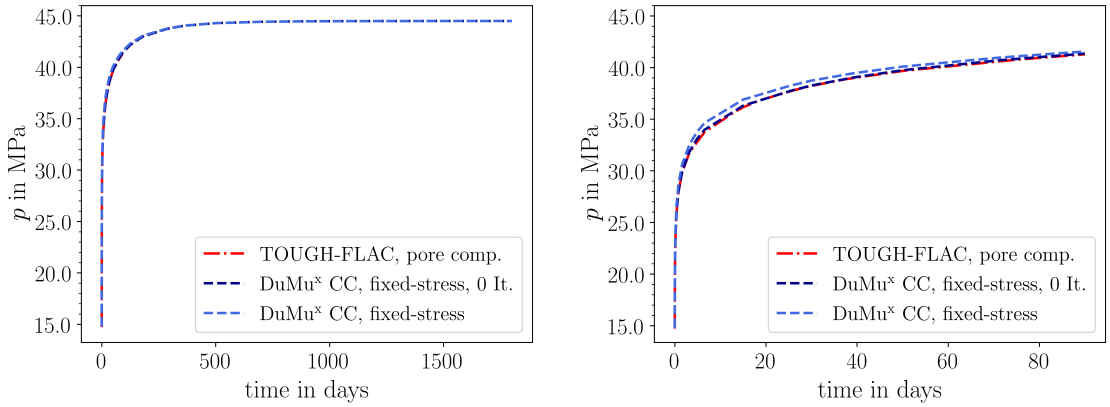

(a) Pressure of the full simulation.

(b) Details of the pressure increase.

Figure 3.3: Pressure evolution at the injection simulated using TOUGH-FLAC, and the cell-centred (CC) discretisation in DuMu^x for a fixed-stress scheme with just one coupling step (equal to zero iterations) and a fully-converged simulation.

The underestimation of the zero-iteration fixed-stress scheme and the pore compressibility approach, respectively, in comparison to the iterated scheme is not only visible in the transient pressure evolution, but also appears in the results of the geomechanics as seen in the plots for the displacement in x-direction (Figure 3.4a) and the volumetric strain (Figure 3.4b). Again, the results of the zero-iteration fixed-stress scheme in DuMu^{x}and FLAC3D are in very good agreement.

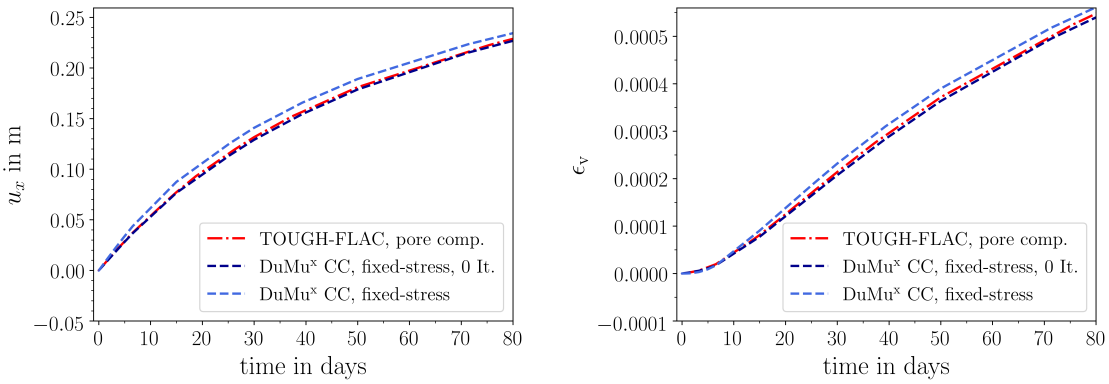

(a) Displacement in x-direction u_x at 500 m horizontal distance and 45 m below from the injection.

(b) Volumetric strain ϵ_v at 500 m horizontal distance 45 m below from the injection.

Figure 3.4: Comparison of selected geomechanical parameters.

In summary, the results of a zero-iteration fixed-stress scheme implemented in DuMu^x matched the ones obtained with TOUGH-FLAC using the pore compressibility very well. For the transient phase of the simulation, an underestimation of these schemes was observed relative to a fixed-stress scheme with iterations. The claim, that such an iterated fixed-stress scheme represents the more physical solution to a coupled flow and geomechanics problem will be further substantiated in the following by comparing it to the fully-coupled approach.

3.6.3 Comparison Fixed-stress - Fully-coupled

As the mass and momentum balance equation for the fluid flow in the fully-coupled approach is discretised with the box method, the corresponding fixed-stress implementation is used. This requires a slight adaption of the problem set-up, since the unknowns are located at different locations. Instead of the two cells with the centers (6.25, 2.5) and (6.25, -2.5), the nine nodes of the two elements are used for the injections. The total injection rate of 0.2 kg/s is kept the same.

Figure 3.5a and 3.5b show that the iterated fixed-stress scheme is identical with the fully coupled solution. Both for the pressure at the injection and at the fault, the two lines lie on top of each other, while again a notable deviation of the zero-iteration fixed-stress/pore compressibility scheme is observable. This reinforces the argument made previously that the iterated fixed-stress scheme serves as the reference solution and the pore compressibility scheme is a simplified and thus deviating representation of the flow-geomechanics coupling.

Figure 3.6 provides further insight into this deviation: Complementing the evolution over time at the two different locations in Figure 3.5a and 3.5b, here the spatial distribution of the

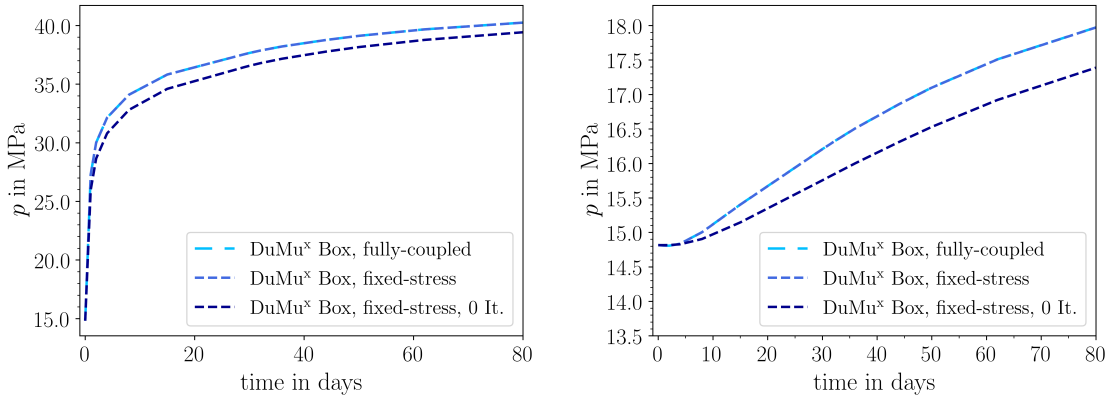

(a) Pressure evolution at the injection.

(b) Pressure evolution at the fault.

Figure 3.5: Evolution of the pressure p over time for different solution strategies.

deviation, that is introduced when no iterations are used, is shown. Four different points in time are depicted, namely after 1 day shortly after the simulation started (Figure 3.6a), at $t = 15$ days and $t = 90$ days during the pressure increase (Figure 3.6b and 3.6c) and finally for $t = 500$ days when equilibrium is reached (Figure 3.6d). It becomes apparent that the underestimation of the pressure evolution at the beginning is the highest around the injection (around 6 %), spreads over time with the pressure front and then decreases with the simulation converging to a steady state.

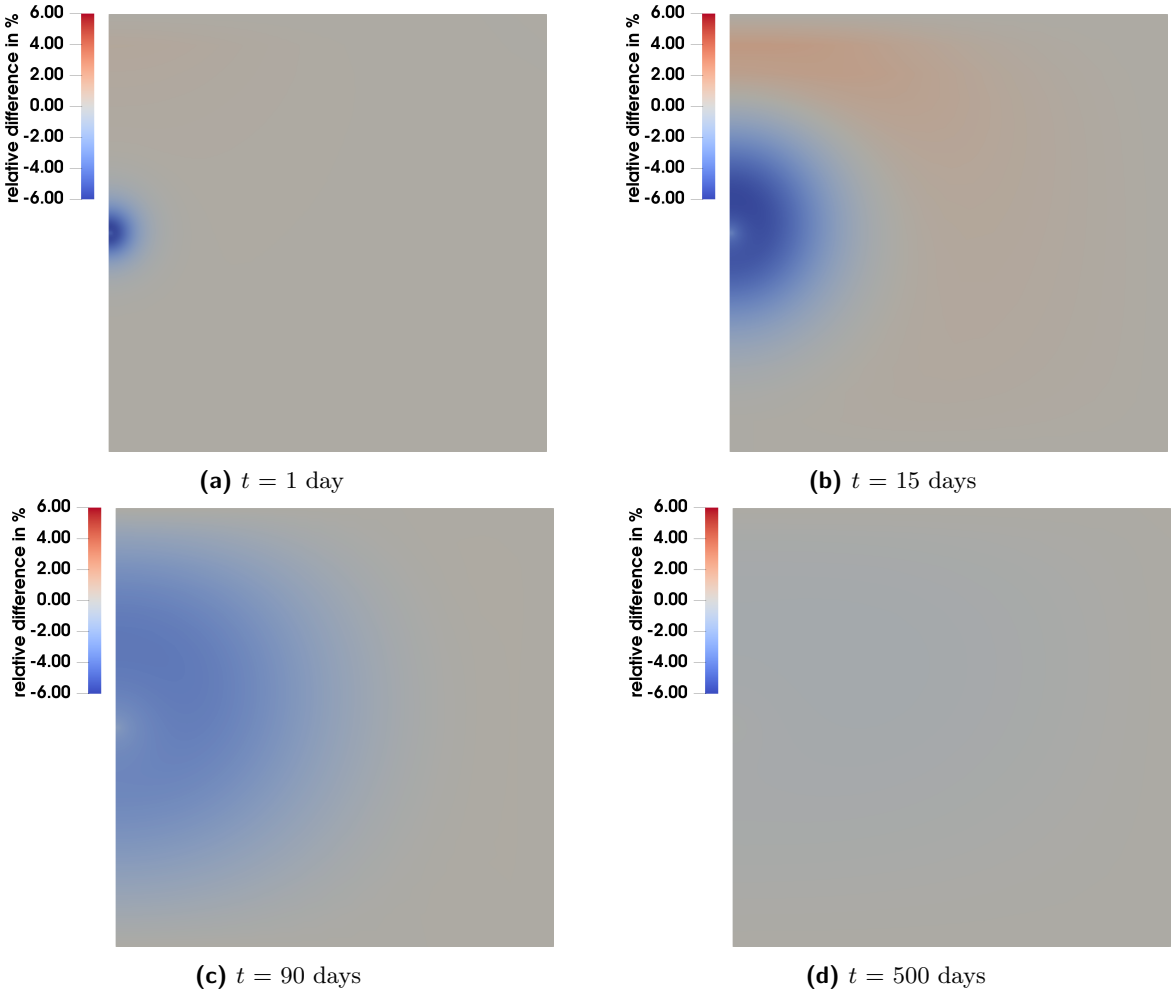

(a) $t = 1$ day

(b) $t = 15$ days

(c) $t = 90$ days

(d) $t = 500$ days

Figure 3.6: Deviation in percent of the zero-iteration fixed-stress scheme relative to the fully-iterate scheme at different points in time.

Plotting the pressure for each of the fixed-stress iterations illustrates how the underestimation decreases over the course of the iterations: Figure 3.7a shows the evolution of the pressure over the iterations for the first time-step. The zeroth iteration underestimates the pressure in comparison to the fully-coupled value. One could also describe this as an overestimation of porosity change calculated from just the pressure difference. As soon as this is corrected in the first iteration by the volumetric strain value obtained from the previous solution of the geomechanics, the estimate of the pressure value improves significantly. After the fourth iteration, the results become undistinguishable. Here, more iterations than necessary were performed to better illustrate the convergence against the fully-coupled result.

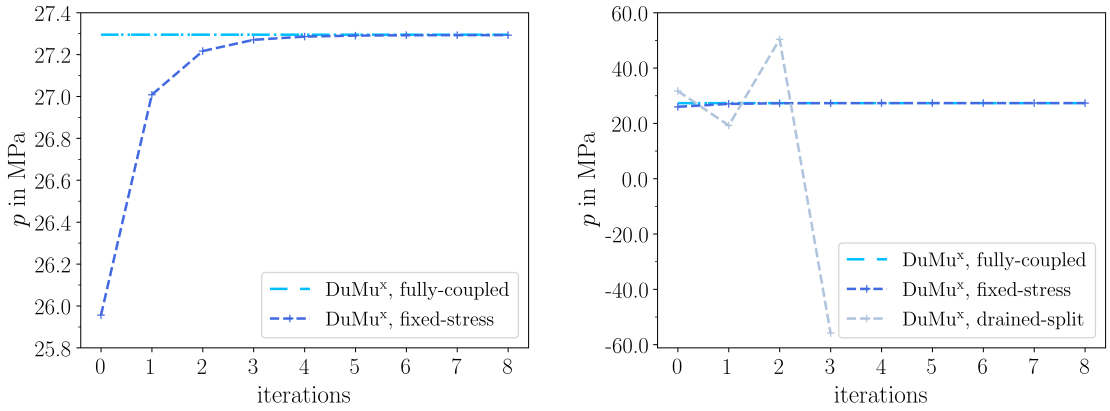

(a) Pressure over sequential iterations for fully-coupled and fixed-stress scheme.

(b) Pressure over sequential iterations for fully-coupled, fixed-stress and drained split scheme.

Figure 3.7: Evolution of the pressure p depending on the number of sequential iterations.

A variation of this plot shown in Figure 3.7b displays the results of the *drained-split* scheme where the flow problem is solved using the strain and stress fields of the previous geomechanics iteration and the pressure is kept constant during the geomechanical step. It becomes clear why Kim et al. (2011a) refer to this scheme as being, at best, conditionally stable.

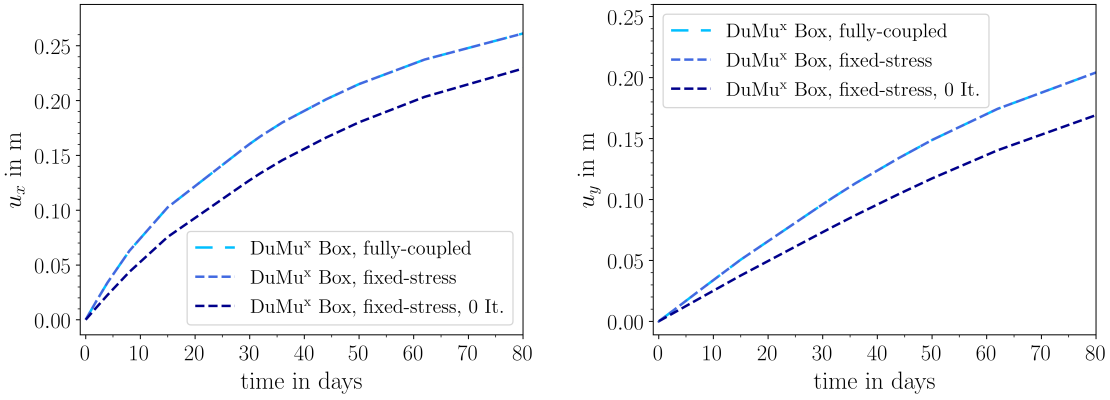

(a) u_x at 500 m horizontal distance from the injection.

(b) u_y at 500 m horizontal distance from the injection.

Figure 3.8: Comparison of the displacements.

The final plots of the comparison for the homogeneous one-phase test case display the two components of displacements (Figure 3.8). The displacement in x-direction u_x is identical for a fully-coupled and a iterated fixed-stress approach, which is shown exemplarily for a point in a distance of 500 m to the injection. Similar to the results observed for the cell-centred scheme, an underestimation of the displacement is observable during the transient phase of the simulation if a zero-iteration scheme is used. The same is true for u_y: The results for the

iterated fixed-stress scheme and the fully coupled implementation are indistinguishable and the zero-iteration fixed-stress produces lower values.

3.6.4 Conclusions

The results of the homogeneous one-phase test case enable a direct comparison of the results for geomechanics and flow calculated with DuMu^{x} with the results from TOUGH-FLAC. As the results match each other, this increases the confidence in the used models.
In addition, the test case simulated with the iterated fixed-stress and the fully-coupled scheme allows two more conclusions: First, the comparison confirms that two implemented approaches produce identical results for a sufficient number of fixed-stress iterations. And second, that the observed underestimation of the fixed-stress scheme with zero iterations is a result of the imperfect approximation of the porosity change by the pore compressibility and significantly improves for four iterations in this example.
The initial hypothesis that a fully-coupled approach is required for an accurate solution has to be extended by recognising the fixed-stress scheme with a sufficient number of iterations as a suitable alternative.
In the following, a test case with more complex physics will be presented to further test the applicability of the different solution strategies.

3.7 CO_2 injection numerical test case

3.7.1 Scenario description

The heterogeneous test case discussed in this section is inspired by a CO_2-injection scenario. The simulation set-up becomes more complex since layers of different properties and a fault is added (see Figure 3.9). The CO_2-injection is located in the centre of a sandstone reservoir with a permeability of $1 \cdot 10^{-13}$ m^2 and a thickness of 100 m. Above the target reservoir is a 150 m thick shale layer with permeability of $1 \cdot 10^{-19}$ m^2, which serves as a caprock. A layer of the same thickness and properties is located below the reservoir. A 1 km long fault zone inclined by an angle of 80° cuts through the reservoir and the shale layers. Its midpoint is located at a depth of 1500 m and at a horizontal distance of 500 m from the injection well. With a permeability of $1 \cdot 10^{-15}$ m^2, it is less permeable than the target reservoir but more permeable than the shale layers. The parameters assigned to the different layers are listed in Table 3.1.

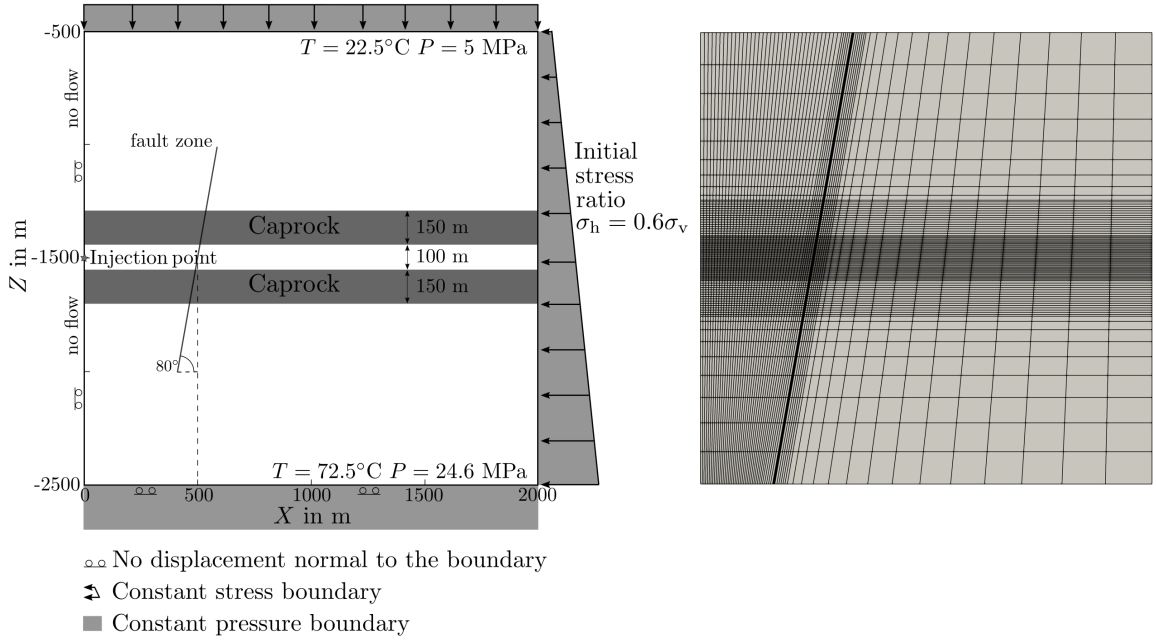

Figure 3.9: Set-up of the CO_2 scenario (left) and domain discretisation (right).

The constant temperature is replaced by a temperature increasing with depth from 22.5 °C to 72.5 °C. The values for the viscosity and the density are temperature-dependent, but the simulation itself is performed isothermally.

For the capillary pressure-saturation relationship and the relative permeability, the formulations by Van Genuchten (1980) (see Equation 2.8 and 2.13) are used.

The injection rate is lowered by a factor of 10 to 0.02 kg/s relative to the one of the homogeneous test case. The grid is the same (see Figure 3.9) and the box method is used for the discretisation of the two-phase flow equations.

Time-steps are again the same for all scenarios and increase over the course of the simulation. Similar scenario set-ups have been used in studies by Mazzoldi et al. (2012) and Rinaldi et al. (2014).

Table 3.1: Material properties of the CO_2-injection scenario.

Parameters	Shale layers	Fault zone	Reservoir
Porosity, ϕ (-)	0.01	0.1	0.1
Rock density, ϱ_s (kg/m^3)	2260	2260	2260
Permeability, k (m^2)	$1 \cdot 10^{-19}$	$1 \cdot 10^{-15}$	$1 \cdot 10^{-13}$
Young's modulus, E (GPa)	10	5	10
Poisson's ratio, ν (-)	0.25	0.25	0.25
Residual wetting saturation, S_{rw} (-)	0.20	0.20	0.20
Residual non-wetting saturation, S_{rn} (-)	0.05	0.05	0.05
Van Genuchten α_{VG} (-)	$5.025 \cdot 10^{-5}$	$5.025 \cdot 10^{-5}$	$5.025 \cdot 10^{-5}$
Van Genuchten m_{VG} (-)	0.457	0.457	0.457
Van Genuchten n_{VG} (-)	1.842	1.842	1.842

3.7.2 General results

In Figure 3.10a, the evolution of the wetting-phase pressure p_w over time is shown at the injection and in the fault. At both locations, the pressure rises, reaches a peak value at around 100 to 200 days and then decreases again. From the plot of the CO_2 saturation S_n over time in Figure 3.10b, it becomes visible that the CO_2 reaches the boundary between the reservoir and the overlying shale above the injection fairly quick (after around 15 days). After 155 days, it also arrives at the location where the fault cuts through the shale caprock at $x = 500$ m and a depth of -1450 m. After a very high initial increase, the saturation change becomes smaller and smaller over time at both locations. The maximum values reached at the end of the simulation after 1800 days are $S_n = 0.56$ above the injection and $S_n = 0.54$ in the fault.

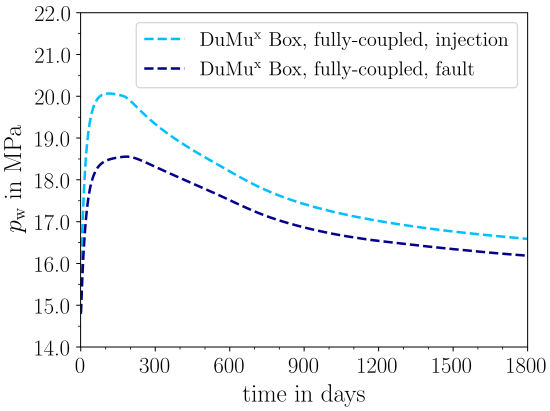

(a) wetting-phase pressure p_w at the injection point (x = 0 m, y = -1500 m) and within the fault at a horizontal distance of 500 m (x = 500 m, y = -1500 m.)

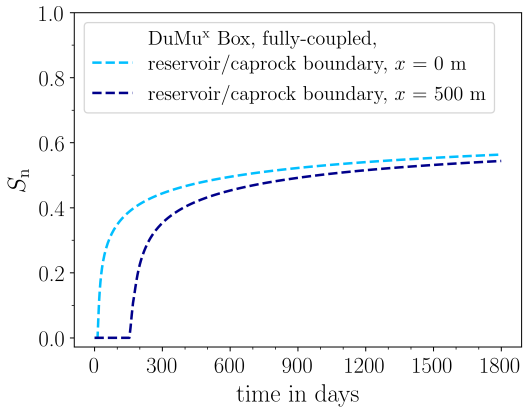

(b) CO_2-saturation S_n at the reservoir/caprock boundary above the injection (x = 0 m) and where reservoir, caprock and fault meet (x = 500 m.)

Figure 3.10: Evolution of p_w and S_n over time at different locations.

Figure 3.11 and Figure 3.12 further illustrate how the CO_2 saturation S_n and the wetting pressure p_w spread in the domain: The spatial distribution of both is shown for t = 1 day, t = 100 days, t = 200 days and t = 1800 days. To highlight the location of the fault and the shale layers, a grey filter with different opacities was added. The less permeable a cell is, the more opaque it is. After one day of injection, the CO_2 spreads around the injection point (see Figure 3.11a). Driven by buoyancy, a large portion of the CO_2 accumulates at the boundary between the reservoir and the overlying shale caprock and then moves laterally along the boundary (Figure 3.11c). When the CO_2 reaches the fault, it also rises through it (visible in Figure 3.12a and 3.12c).

Figure 3.11b, 3.11d, 3.12b and 3.12d show the corresponding pressure distribution in the domain. The CO_2 pressurises the reservoir section bounded by shale layers and the fault and also the fault itself. As already observed for the plots over time, the wetting pressure p_w reaches a peak value between 100 and 200 days and then decreases again.

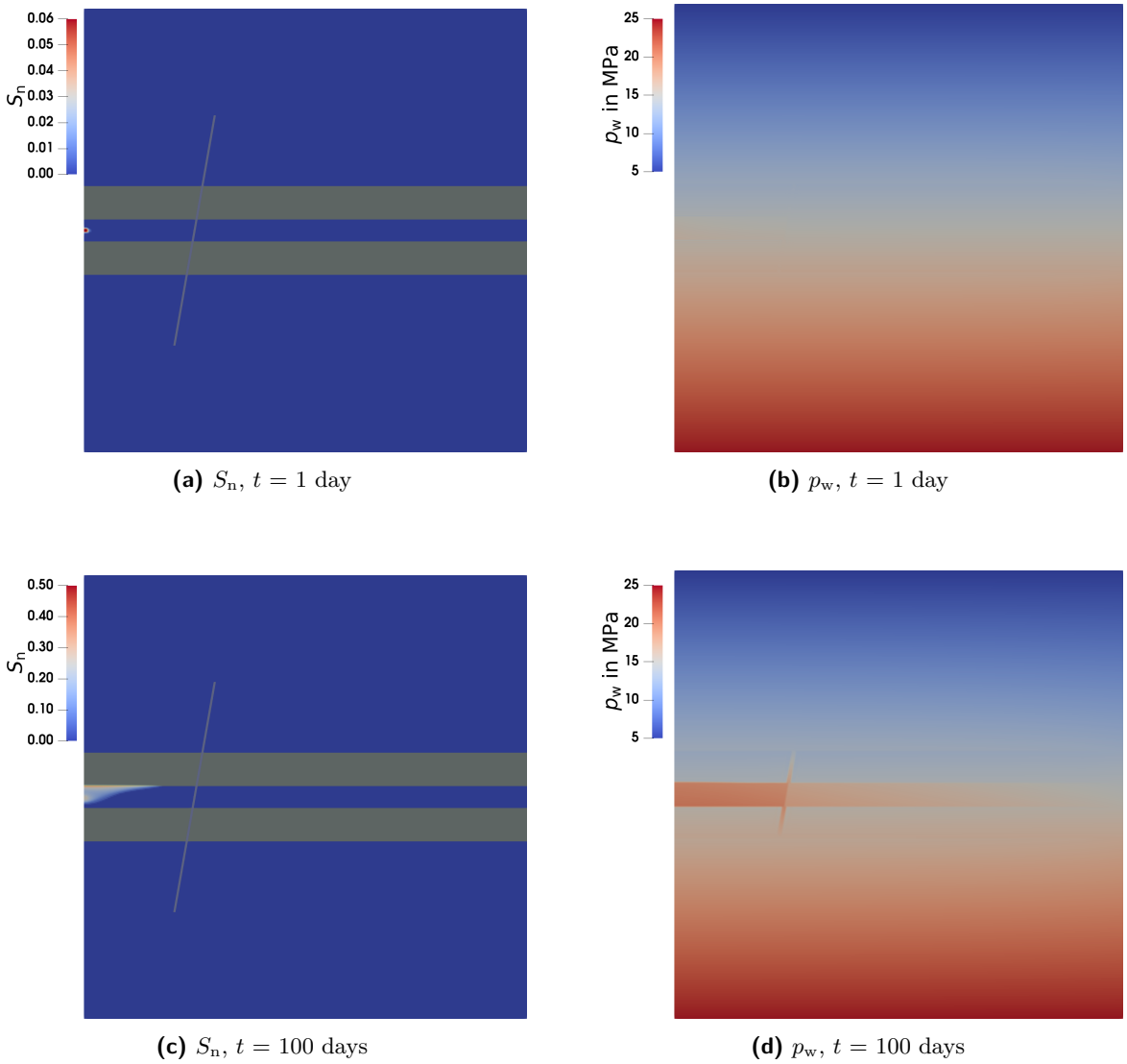

(a) S_n, $t = 1$ day

(b) p_w, $t = 1$ day

(c) S_n, $t = 100$ days

(d) p_w, $t = 100$ days

Figure 3.11: Spatial distribution of the CO_2 saturation S_n and the wetting pressure p_w for two points in time during the pressure build-up phase of the simulation. The image for the saturation distribution are overlain by a grey filter where a permeability of $1 \cdot 10^{-19}$ corresponds with an opacity of 1.0 and $k = 1 \cdot 10^{-13}$ with an opacity of 0.0.

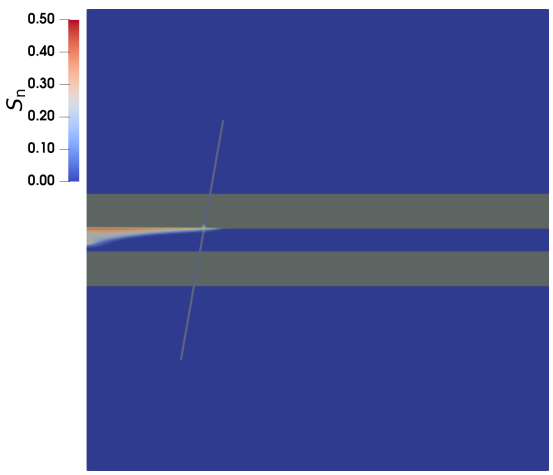

(a) S_n, $t = 200$ days

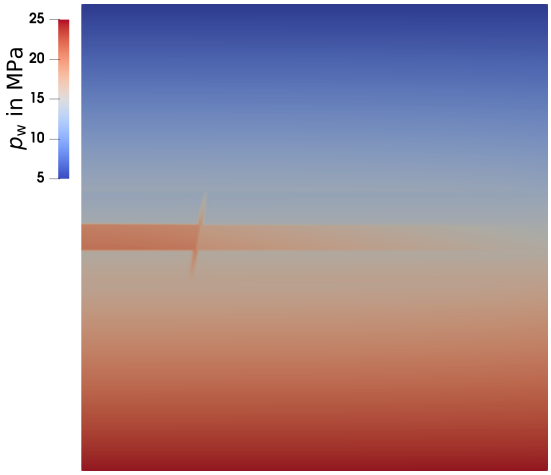

(b) p_w, $t = 200$ days

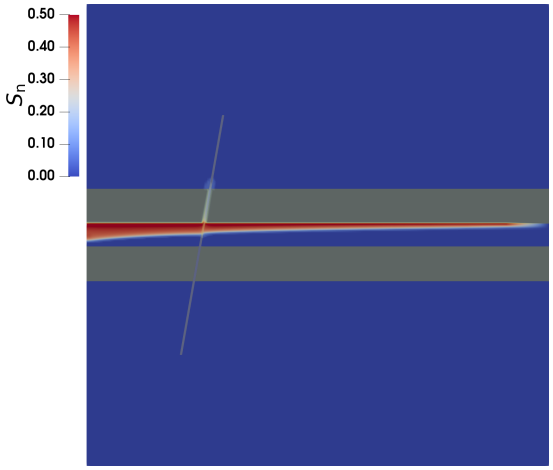

(c) S_n, $t = 1800$ days

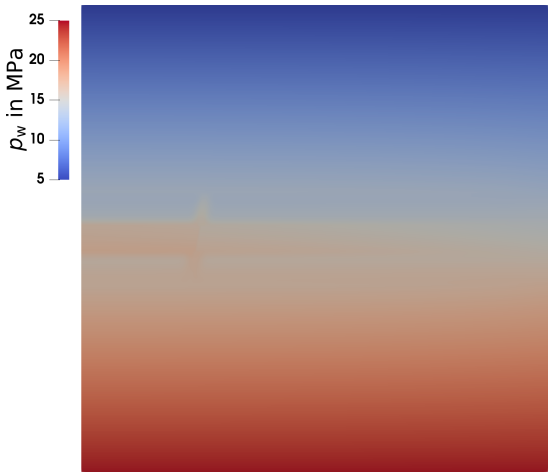

(d) p_w, $t = 1800$ days

Figure 3.12: Spatial distribution of the CO_2 saturation S_n and the wetting pressure p_w at two points in time during the pressure decrease of the simulation. The image for the saturation distribution is again overlain by a grey filter where a permeability of $1 \cdot 10^{-19}$ corresponds with an opacity of 1.0 and $k = 1 \cdot 10^{-13}$ with an opacity of 0.0.

The pressure peak and the following decrease is remarkably different from the behaviour observed for the homogeneous case. To distinguish between the different effects introduced by adding the layers and the fault and by introducing CO_2 as a second fluid phase, some variations of the scenarios were simulated.

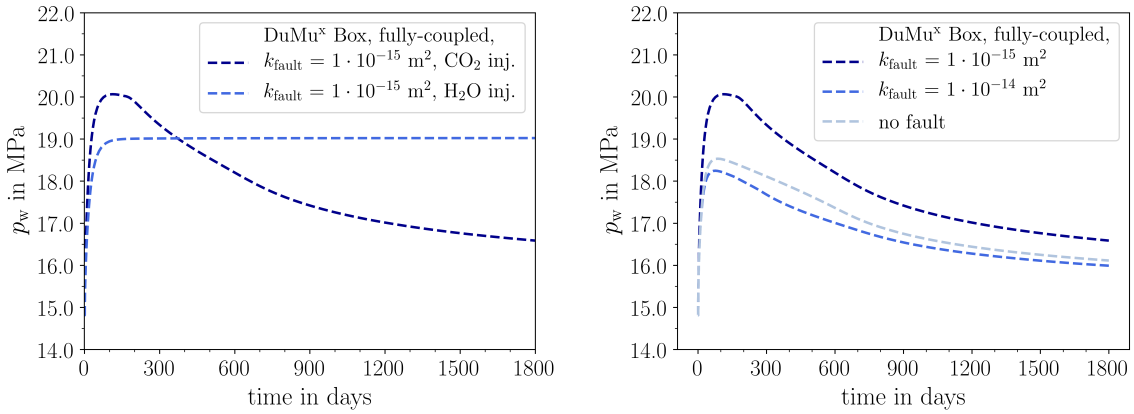

(a) p_w at the injection for a CO_2 and a water injection.

(b) p_w at the injection for two different fault zone permeabilities and no fault zone.

Figure 3.13: Pressure evolution for different scenario variations.

Figure 3.13a shows the pressure evolution over time for a water injection in comparison to the wetting-phase pressure of the CO_2 injection, while the rest of the simulation set-up was kept the same. Similar to the homogeneous case, the pressure rises and reaches a plateau value for the one-phase case. This indicates that the fault has a similar effect as the constant pressure boundary on the right side of the domain in the homogeneous example: Once steady state between the injection and the flow through the fault into the surrounding layers and the reservoir behind the fault is established, the pressure stays constant for the one-phase test case. The additional pressure increase and decrease on the contrary is a distinctive feature of the two-phase behaviour - or, to be more precise - is an effect of the relative permeability. For low non-wetting phase saturations, the relative permeability is also very low (or even zero for $S_n = 0$). This corresponds to a high resistance to CO_2 replacing water and thus the pressure increases, too. Over time, rising non-wetting phase saturations and the increasing lateral surface of the contact area between the phases reduce this resistance, which explains the pressure decrease in the later stage of the simulation.

To determine the effect of the fault on the system, two more scenario variations were performed, namely one with an increased fault permeability of $1 \cdot 10^{-14}$ m^2 and one without a fault. For the latter, the pressure evolution is determined only by the confining layer of shale and the constant pressure boundary on the right. This results in a less pronounced pressure peak (see Figure 3.13b). The pressure peak becomes even less distinct for the higher permeable fault,

so in comparison to the case without a fault, one can conclude that the fault's breaching of the caprock outweighs the barrier effect of the fault itself. This is plausible since the fault connects the central reservoir with the large permeable reservoir above and below the shale layers and thus explains the less pronounced pressure peak.

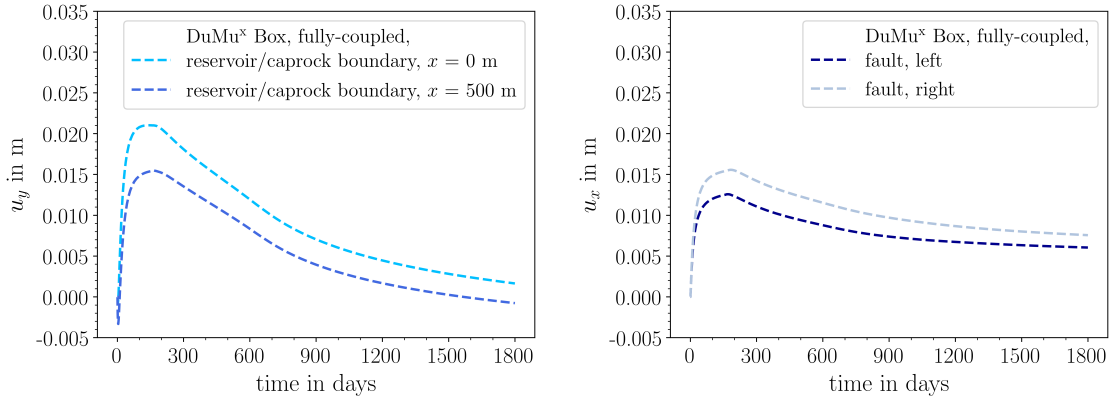

(a) Displacement in y-direction u_y at the reservoir/caprock boundary above the injection (x = 0 m) and where reservoir, caprock and fault meet (x = 500 m.)

(b) Displacement in x-direction u_x on the left and on the right edge of the fault zone within the caprock layer at a depth of 1332 m.

Figure 3.14: Comparison of the displacements.

The evolution of the displacement in y-direction at the reservoir/caprock boundary above the injection follows the pressure evolution over time (see Figure 3.14a). At first glance, this seems to be also true for u_y at the triple point of fault, caprock and reservoir (x = 500 m). On a closer look, one notices an initial downward movement of that point. This rather peculiar behaviour becomes clear through visualisation of the full deformation as shown in Figure 3.15a (exaggerated by a factor of 1000): The reservoir/caprock boundary is bent upward above the injection, but viewed as a whole is rather tilted like a see-saw, so points near the fault experience some initial downward movement. The more the reservoir is pressurised, the more all points of the reservoir/caprock boundary are pushed upwards (see Figure 3.15b). For completeness, it should also be mentioned that a small initial pressure drop is observable for points which are not immediately affected by the injection due to a numerical artefact. Even if no injection takes place, a horizontal change in pressure is observable, which is more pronounced the further left a point in the domain is located. It results from the pressure only being prescribed on the right hand side and small errors introduced by the inexact flux calculation over the non-orthogonal element faces in the domain. Nonetheless, this effect is negligible, especially in comparison to the influence of the injection. The displacement in x-direction in Figure 3.14b illustrates the deformation of the fault within the caprock: Two locations are depicted, one on the left and one on the right of the fault. It becomes evident that the pressurisation of the fault is also accompanied by an opening of fault as both edges

move away from each other.

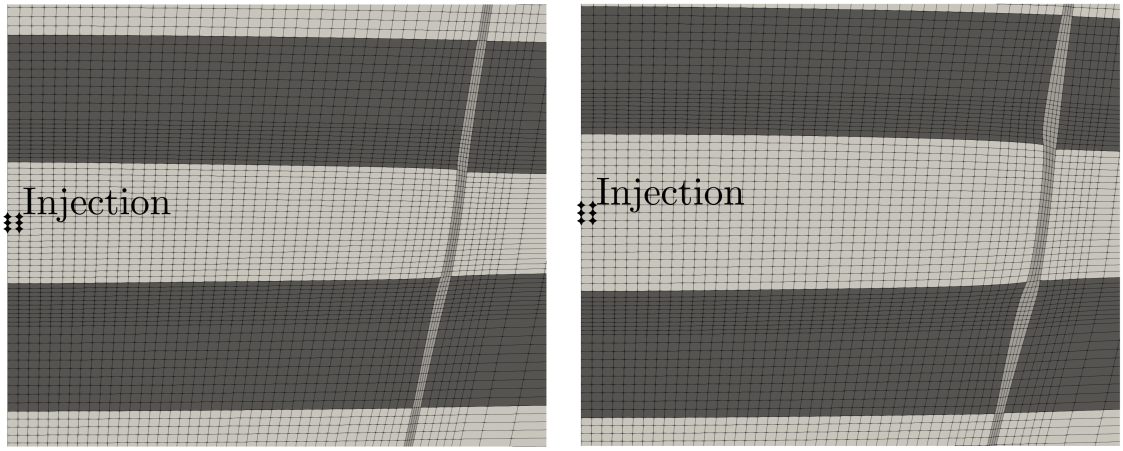

(a) $t = 7$ days **(b)** $t = 100$ days

Figure 3.15: Deformation of the cells around the injection exaggerated by a factor of 1000.

3.7.3 Fully-coupled and fixed-stress

The results presented up to this point were obtained using the fully-coupled approach. In the introduction, the question was raised how the fully-coupled approach and a fixed-stress scheme with iterations and without them (alias the pore compressibility scheme) would compare against each other for scenarios of relevance for practical applications. The results for the homogeneous example already made clear that the implementation of the fixed-stress schemes produces identical results as the fully-coupled approach if enough iterations are performed.

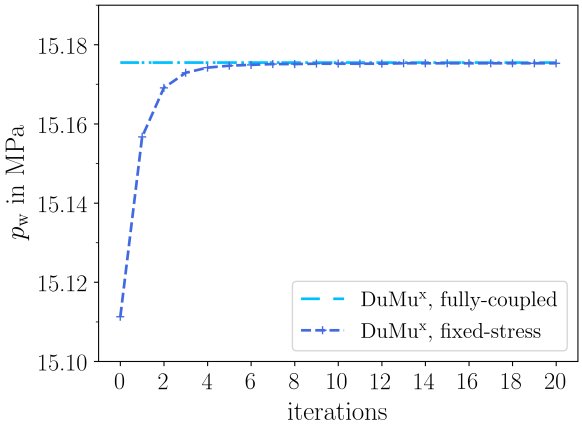

Figure 3.16: Pressure over sequential iterations for fully-coupled and fixed-stress scheme.

Figure 3.16 shows that this is also true for a more complex test case involving two fluid phases. Again, a higher number of iterations was specified for illustration purposes and one could argue that a less restrictive stopping criterion would achieve a similar accuracy. But if zero iterations are performed, the pressure at the injection is again underestimated for the first time-step.

From the homogeneous one-phase test case, the conclusion was drawn that the transient parts of the simulation are those where the results for the zero-iteration case and the fully-coupled scheme differ the most. Following this, one would expect that the differences are even more prominent for a scenario that includes layers with different hydraulic and geomechanical properties, a fault zone and two fluid phases.

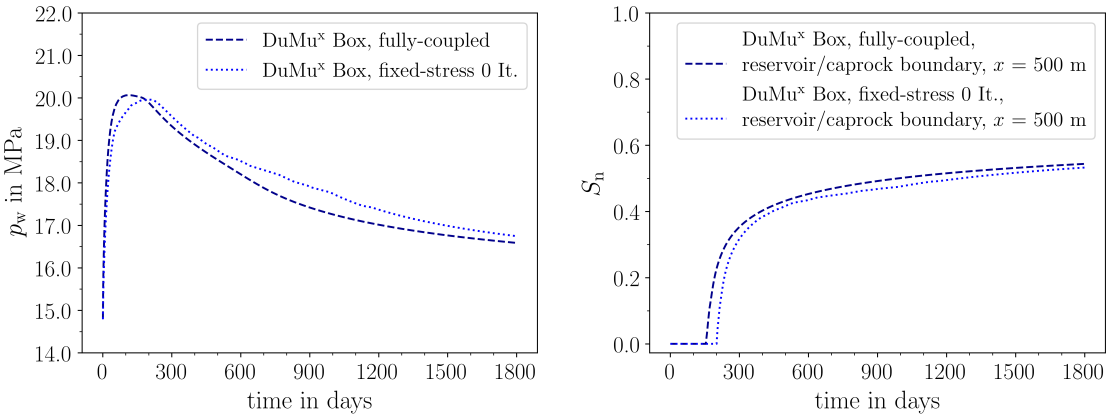

(a) p_w at the injection point (x = 0 m, y = -1500 m). **(b)** CO_2-saturation S_n where reservoir, caprock and fault meet (x = 500 m).

Figure 3.17: Comparison of the temporal evolution of p_w and S_n obtained using the fully-coupled and the fixed-stress scheme with zero iterations.

Indeed, the differences in pressure and saturation between the fully-coupled and the fixed-stress scheme with zero iterations are significant: Both the pressure increase and decrease show considerable derivations from the fully-coupled solution (Figure 3.17a). Comparing these pressure derivations in the order of the 0.1-1.0 MPa to the differences between the scenario variations of one to several MPa puts them into context: Not iterating has almost the same effect as whether a fault is detected or overlooked.

With respect to the way the CO_2 spreads, Figure 3.17b reveals that it arrives around 50 days later at the triple point of reservoir, caprock and fault when no iterations are performed.

In addition to the temporal evolution in Figure 3.17, the spatial distribution of the derivation between the fully-coupled and the zero-iteration fixed-stress scheme is shown in Figure 3.18. At t = 100 days, the relative differences in the wetting-phase pressure p_w are the highest in the vicinity of the reservoir/shale layer contact (see Figure 3.18a). The absolute differences in the non-wetting phase saturation S_n after 200 days displayed in Figure 3.18b are concentrated on

the CO_2-front. The maximum values of 0.20 are in the same order as the values for saturation.

(a) Relative difference in p_w for the zero-iteration fixed-stress scheme with respect to the fully coupled solution at $t = 100$ days.

(b) Absolute difference in the CO_2-saturation S_n for the zero-iteration fixed-stress scheme with respect to the fully coupled solution at $t = 200$ days. The shale layers are depicted in grey.

Figure 3.18: Comparison of the spatial distribution of p_w and S_n obtained using the fully-coupled and the fixed-stress scheme with zero iterations in an early stage of the simulation ($t = 100$ days for p_w, $t = 200$ days for S_n).

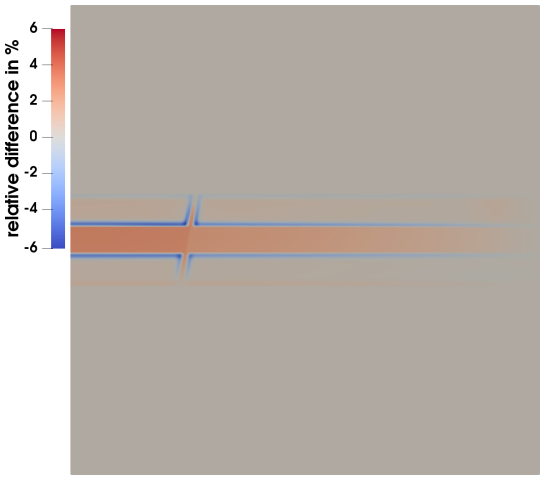

(a) Relative difference in p_w for the zero-iteration fixed-stress scheme with respect to the fully coupled solution at $t = 900$ days.

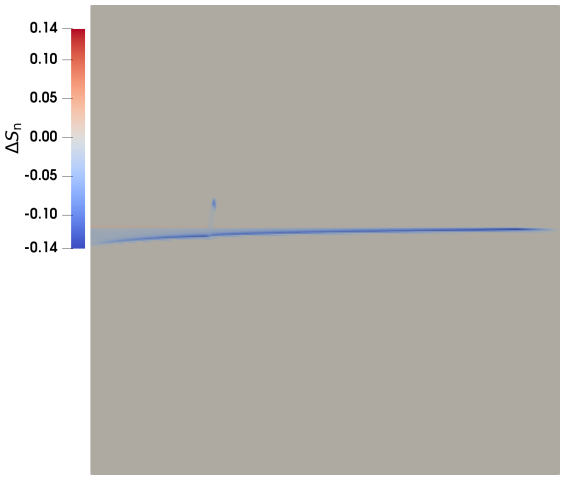

(b) Absolute difference in the CO_2-saturation S_n for the zero-iteration fixed-stress scheme with respect to the fully coupled solution at $t = 900$ days.

Figure 3.19: Comparison of the spatial distribution of p_w and S_n obtained using the fully-coupled and the fixed-stress scheme with zero iterations at $t = 900$ days.

Figure 3.19 shows the same set of charts for $t = 900$ days. The effects are similar to the ones described for the results at an earlier stage of the simulation: Not iterating causes deviations especially at the front between water and CO_2 and around the interfaces between caprock, reservoir and fault.

3.7.4 Conclusions

The homogeneous numerical test case successfully tested the results for plausibility by comparing them to the ones obtained using the TOUGH-FLAC software and thus increased the confidence in the models implemented in DuMu^x. It also proves the equivalence of the zero-iterations fixed-stress scheme and the approach using the pore compressibility and allows the conclusion, that errors made by using such a simplified representation of the flow-geomechanics interaction are especially relevant for the transient parts of the simulation.
A further comparison of the results from the more complex CO_2 scenario with results from TOUGH-FLAC was not conducted as a benchmark study for a CO_2 scenario including the both DuMu^{x}and TOUGH2 has already been performed by Class et al. (2009). Instead, the CO_2 scenario's analysis focusses on expanding the comparison of the different solution approaches by introducing additional effects as different layers, a fault zone and two fluid phases are included. This further tests the posed question of the best-suited approach to represent the coupled processes of flow and geomechanics in porous media. It turns out that the differences between a fixed-stress scheme without iterations (equivalent to a pore compressibility scheme) become more pronounced for this scenario as effects of the relative-permeability and the capillary pressure-saturation relationship in multi-phase systems increase the significance of the transient effects. Depending on the perspective one has on the extent of tolerable derivations, one could justifiably conclude that the fixed-stress scheme without iterations is not suited to model this scenario accurately.
In addition, it could be shown that over the course of the fixed-stress iterations, the scheme converges to the fully-coupled solution for this scenario, too. So including the fixed-stress scheme into the scope of the hypothesis is also valid for two phases.

3.8 Efficiency comparison

3.8.1 Theoretical considerations

The last paragraphs have covered the accuracy of the different solutions strategies in detail by comparing the results for different scenarios. But one is often forced to strike a balance between accuracy and computational costs, so a thorough investigation of the different approaches also has to take the computational effort to achieve these results into account.
The key difference between the approaches in this respect is the size of the linear systems, that ought to be solved. Golub and van Loan (2012) state that it should require $2 \cdot N \cdot p \cdot q$

floating-point operations per second to solve a linear system of N unknowns with a direct solver. p and q are upper and lower limits of the bandwidth. In our two-dimensional case the ideal bandwidth would be $\sqrt{n}$. Following this, the required operations O for a linear system of n unknowns should be proportional to 2 N^2 in an asymptotic consideration:

$$O = C \cdot N^2 \tag{3.42}$$

with C as the unknown proportionality constant, which includes the factor 2.
So ideally, one would expect that for a direct solver in a two-dimensional case, the computational cost of the fully-coupled scheme with twice the number of unknowns is four-fold compared to just solving for p_w and S_n using the fixed stress scheme. The same is true for solving just the geomechanics for the two components of the displacement. But since a coupling step requires to solve both flow and geomechanics, its cost is the sum of solving the flow and the geomechanics, so it is computation-wise half as expensive as the fully-coupled scheme. This means that in theory, one can perform two coupling steps (i.e. one iteration) until this advantage is used up. Taken into account the results provided for the convergence of the fixed-stress scheme over the iterations, one iteration can be hardly considered as sufficient in terms of accuracy.

3.8.2 Numerical test case

To test this for our implementation, a scenario where the grid can be easily refined was set up. This allows to measure the computational effort for different numbers of unknowns. The scenario consists of a 1 km $\times$ 1 km domain in a depth of 1 to 2 km. The lateral displacements are fixed on the bottom as well as on the left and right side. The pressure is fixed on both sides and on the top using a hydrostatic pressure distribution assuming a wetting-fluid density of 1059 kg/m^3. The initial stress on the top of the domain is calculated from the overlying rock formations, for which a density of 2650 kg/m^3 is assumed. The Young's modulus is 6 GPa and the Poisson ratio 0.2. The rock has a porosity of 0.2 and a permeability of $1 \cdot 10^{-14}$ m^2. All this can be found in Figure 3.20, too. The figure also shows the location of the injection point in the centre of the domain, where CO_2 at a rate of 0.0025 kg/s is injected.
To quantify the computational effort, the Callgrind profiling tool available in the Valgrind's tool suite was used to measure the number of instructions fetched (NoI).
Table 3.2 lists the instructions performed for one Newton update by a direct solver for the fully-coupled model in comparison to the number of instructions performed for solving the 2p- and the el-part of the fixed-stress scheme once. The table also specifies the elements of the discretisation and the number of unknowns for the two schemes. This allows to check

whether the proportionality between the computational effort and the square of the number of unknowns (Equation 3.42) can be observed.

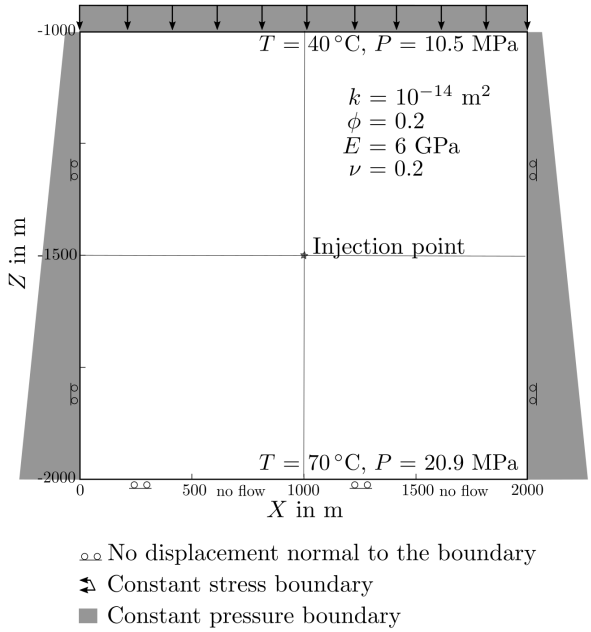

Figure 3.20: Setup of the test case for measuring the computational effort.

In Figure 3.21 the ratio of the fetched instructions and the square of the number of unknowns is plotted over the number of unknowns. The overhead dominates the instruction for small element numbers. The figure thus shows only the results for 16 x 16 elements and more. The given data points allow to infer that the ratio instructions/unknowns^2 converges to a constant value, just as proposed in Equation 3.42. Nonetheless, the 2p- and the el-part of the fixed-stress scheme have a similar convergence behaviour, while the one for the fully-coupled scheme differs from the two. Accordingly, the idealistic assumption of two fixed-stress iterations having the same computational cost as one fully-coupled Newton update step does not hold true here. Instead, the ratio between the number of instructions needed for the fully-coupled scheme NoI_{FC} and the sum of the respective number of instruction for the decoupled scheme $\text{NoI}_{\text{FS,2p}}$ and $\text{NoI}_{\text{FS,el}}$

$$r_{\text{FC/FS}} = \frac{\text{NoI}_{\text{FC}}}{\text{NoI}_{\text{FS,2p}} + \text{NoI}_{\text{FS,el}}} \tag{3.43}$$

is a measure for how much one saves in computational effort by using one coupling step of the fixed-stress scheme in comparison to the fully-coupled scheme. In Table 3.2, it is referred to as the speed-up factor and directly translates into the number of iteration one can perform before surpassing the computational effort of the fully coupled scheme. The previous numerical examples showed that at least 4-5 fixed-stress iterations are needed to achieve a

similar accuracy. With factors ranging between 1.42 and 4.66, there is hardly any gain in computational effort without sacrificing accuracy for the studied domain sizes.

Table 3.2: Instructions fetched by a direct solver (SuperLU) for different discretisations to solve one Newton update for the fully-coupled scheme (FC) and for one iteration of the fixed-stress approach (FS). FS(2p) and FS(el) denote the respective sequential sub-problems for flow and geomechanics.

discretisation	No. of unknowns		Instructions per Newton solve			Speed-up
(elements)	FC	FS (el & 2p)	FC	FS(2p)	FS(el)	factor
2 x 2	36	18	$6.78 \cdot 10^5$	$2.38 \cdot 10^5$	$2.37 \cdot 10^5$	1.42
4 x 4	100	50	$3.47 \cdot 10^6$	$8.05 \cdot 10^5$	$8.48 \cdot 10^5$	2.10
8 x 8	324	162	$1.60 \cdot 10^7$	$3.78 \cdot 10^6$	$4.01 \cdot 10^6$	2.05
16 x 16	1156	578	$9.95 \cdot 10^7$	$2.03 \cdot 10^7$	$2.13 \cdot 10^7$	2.40
32 x 32	4356	2178	$5.89 \cdot 10^8$	$1.20 \cdot 10^8$	$1.29 \cdot 10^8$	2.36
64 x 64	16900	8450	$4.24 \cdot 10^9$	$9.19 \cdot 10^8$	$9.98 \cdot 10^8$	2.21
128 x 128	66564	33282	$4.00 \cdot 10^{10}$	$5.09 \cdot 10^9$	$5.54 \cdot 10^9$	3.78
182 x 182	133956	66978	$1.16 \cdot 10^{10}$	$1.13 \cdot 10^{10}$	$1.36 \cdot 10^{10}$	4.66
256 x 256	264196	132098	$2.39 \cdot 10^{11}$	$2.90 \cdot 10^{10}$	$3.08 \cdot 10^{10}$	4.00
364 x 364	-	266450	-	$6.59 \cdot 10^{10}$	$7.31 \cdot 10^{10}$	-

The comparison here was solely based on the number of instructions per Newton step, so it is as independent as possible from effects introduced by the implementation. Nonetheless, it has to be noted that the fixed-stress scheme uses line search algorithm for the Newton scheme. This means that before the update suggested by the Newton method is applied, the algorithm checks whether the new update leads to a smaller residual in comparison to the previous Newton iteration. If this is not the case, the update is divided by constant factor until this condition is met. Without this modification, the Newton method for the fixed-stress scheme did not converge. In contrast, the fully-coupled model could handle the full update as suggested by the Newton algorithm. This has the effect that the fixed-stress approach needs more Newton iterations per time-step than the fully-coupled scheme, which further reduces the speed-up.

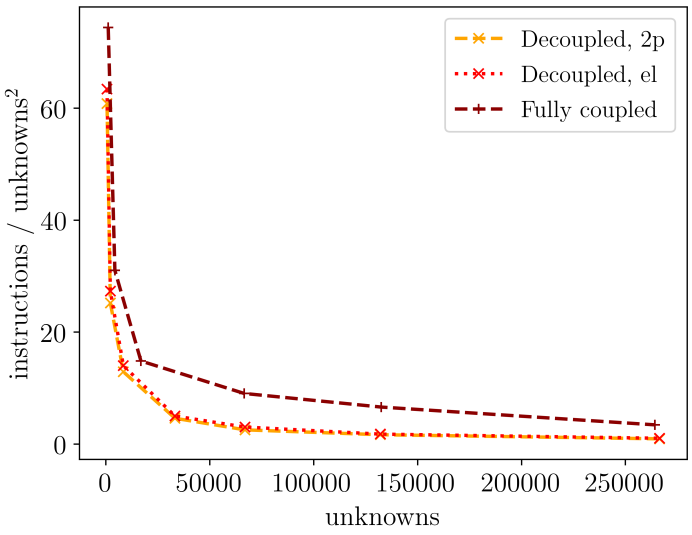

Figure 3.21: Measured ratio of numbers of instruction/unknowns^2 for different numbers of unknowns.

3.9 Conclusions

This chapter provides a broad review of different approaches to numerically solve problems for flow and geomechanics. In doing so, it bridges the gap between commonly used pragmatic sequential approaches such as the TOUGH-FLAC software coupling and iterative sequential approaches such as the fixed-stress scheme (Kim et al., 2011a) that derive the decoupling of the balance equations for flow and geomechanics in a mathematically thorough way.
In detail, a homogeneous numerical test case provided proof, that the implemented fixed-stress scheme in DuMu$^{\text{x}}$ produces equivalent results as TOUGH-FLAC, which uses the pore compressibility, when one solves flow and geomechanics only once. Oberkampf and Trucano (2002) define model verification as the substantiation that a computerized model represents a conceptual model within specified limits of accuracy.
The fact that the implementation of the same conceptual model in DuMu$^{\text{x}}$ and TOUGH-FLAC produces similar results thus provides this verification. It could also be shown that using the fixed-stress in its original form as an iterative sequential scheme produces identical results as a fully-coupled scheme. The results of this true representation of the flow-geomechanics coupling are different from the ones obtained using the pore compressibility and the zero-iteration fixed-stress scheme in the transient phase of the simulation. So the simplicity of the latter schemes comes at the cost of accuracy. This effect becomes even more prominent for a more complex numerical test case involving different layers, a fault zone and a second fluid phase in the form a CO_2 injection. The hypothesis in the introduction boldly stated that efficient and accurate simulations of coupled flow and geomechanics can only be performed

using the fully-coupled model. Regarding accuracy, this has to be expanded by the iterative sequential fixed-stress scheme, which produces results of the same quality as the fully-coupled approach. Whether the pore compressibility and the zero-iteration fixed-stress scheme are accurate *enough* lies in the eye of the beholder. One could argue that the uncertainty in the geologic parameters (e.g. permeability, porosity, elastic constants etc.) dominates over the error introduced by solving flow and geomechanics only once. While this might be true in many cases, the CO_2 injection scenario provided the point that pressure differences between the approaches were at times in the same order as the geologic uncertainty (cf. Walter et al., 2012), in this case shown by means of fault, existing or not. In addition, the following chapter on fault reactivation provides evidence that a difference in pressure of 1 MPa might be small relative to the total pressure of several tens of Megapascals, but could be decisive for the magnitude of the possible earthquake.

The assumption that splitting up the Jacobian results in a decreased computational effort in comparison to solving for all unknowns at same time was confirmed by measuring the number of instructions a direct solver performs during a Newton step. But as several iterations are required for the fixed-stress scheme to achieve similar accuracy as the fully-coupled scheme, this gain is mostly used up. While not realised in this work, in theory replacing the direct solver by an iterative solver such as the algebraic multigrid (AMG, Stüben, 1999) should further reduce this gain, as the computational effort per degree of freedom becomes constant, or, in other words, the required operations to solve the linear system then increases only linearly with the number of unknowns.

At this point, one has to mention that in-between the pore compressibility scheme and the iterated fixed-stress scheme, hybrid schemes exist. Instead of not feeding the geomechanical results back into the flow part in any way, one could update for instance porosity and permeability of the next time-step using the result of the geomechanics from the previous one. Nonetheless, these approaches are possibly the worst of both worlds: Less efficient and still not accurate enough.

All things considered, the accuracy of the fully-coupled approach cannot be achieved efficiently with any other scheme. Schemes requiring less computational effort exist, but come at the cost of reduced accuracy. Furthermore, implementing an algebraic multigrid solver (Stüben, 1999)) or applying the fixed-stress as a pre-conditioner as suggested by (White and Borja, 2011) could increase the efficiency of the fully-coupled model even more.

4 Fault reactivation

The previous chapters have covered the combined modelling of multi-phase flow and geomechanics. The focus of this chapter will be on fault reactivation.

As outlined in Subsection 2.3.6, shear failure occurs when the shear stress τ surpasses the shear strength τ_{s}, which can be determined from $\tau_{\mathrm{s}} = (\sigma - p)\,\mu_{\mathrm{frict}} + c$. The criterion can be reached and exceeded if the shear stress τ is increased, if the normal stress σ is reduced or if the pore pressure p is raised. This is relevant as shear failure on a fault can be the starting point for an earthquake.

While the majority of all earthquakes happen naturally, some have been linked to human activities, especially in regions were earthquakes are unusual. Following the definition of Ellsworth (2013), such earthquakes will be labelled *induced* without discriminating between earthquakes that primarily release stresses caused by human activities and earthquakes that release naturally existing stresses but are triggered by anthropogenic activities. In his paper, Ellsworth (2013) reviews injection-induced seismicity and concludes that only earthquakes linked to long-term and high volume injections reach moment magnitudes (M_w) that could seriously damage buildings. Such injection schemes are common for deep waste-water injections. The most prominent examples are the M_{w} 5.7 November 6, 2011, central Oklahoma earthquake (Keranen et al., 2013) and the M_{w} 4.9 May 17, 2012, east Texas earthquake (Frohlich et al., 2014). In these cases, the respective epicenters were located close to the waste-water injection wells, but this is not necessarily always the case. In 2013, a long-term, high-volume salt water injection in the Paradox Valley, Colorado, lead to a M_{w} 3.9 earthquake 8 km away from the well, 15 years after the initial seismic response was observed (Ellsworth, 2013). This example illustrates that a detailed understanding of the pore pressure and stress evolution in time and space is essential to avoid the risk of unexpected seismicity. In this sense, Ellsworth (2013) argue that legislation should require to report characteristic data such as volume, peak and mean injection pressures and the measurement of pre-injection formation pressure.

In contrast to shear failure induced by waste-water injections, the pore pressure is increased during hydraulic fracturing operations with the intention to induce tensile failure due to surpassing the least principal stress σ_3 (see Subsection 2.3.6 Equation 2.93). Nonetheless, the operation can sometimes cause shear failure, too. Although intended, the induced seismicity is characterised by low magnitudes (Ellsworth, 2013). Nonetheless, small felt earthquakes

proved to be critical for the public acceptance of hydraulic fracturing projects (De Rijke, 2013; Williams et al., 2017). The development of a geothermal system under the city of Basel, Switzerland, can be taken as a deterrent example in this respect: Four M_w 3 events, including the M_w 3.4 mainshock of December 8, 2006 (Deichmann and Giardini, 2009), ultimately lead to the termination of the project.
Altogether, these events and findings highlight the need to expand existing model concepts capable of modelling coupled multi-phase flow and poro-mechanics towards the simulation of fault reactivation. As stated in the introduction, the hypothesis that fault reactivation can be modelled by using the stress-drop as the characteristic parameter will be tested. Such an approach was presented in Beck et al. (2016) and the following sections will be based on this paper and subsequent developments.

4.1 Modelling concepts

Different approaches for modelling fault reactivation have been developed: Phase-field models represent a fault interface by describing the transition from broken to intact rock diffusely with an order parameter (e.g. Mikelic et al., 2015). Other approaches include faults as discrete surfaces using tail-interface (Ferronato et al., 2008) or zero-thickness elements (Jha and Juanes, 2014; Segura and Carol, 2008). Accounting for the fact that fault zones are complex features consisting of a fault core and a damage zone, Rutqvist et al. (2013) choose to model the fault not as a surface but as a fault zone instead, using a *ubiquitous joint model*. A comparison between different fault modelling approaches by Cappa and Rutqvist (2011) revealed that both a mechanical interface and finite-thickness solid elements produce similar results. Thus, the latter approach using finite thickness elements is chosen for representing faults, as this fits well into the existing implementation and is also applicable to a variety of fault architectures ranging from single surfaces to complex fault zones (Cappa and Rutqvist, 2011).
In a similar fashion, the description of the relevant physics during a seismic event varies: It remains under discussion, whether the coefficient of friction μ_{frict} is a function of the slip rate and a state variable (accounting average maturity of contact asperities) such as used by Jha and Juanes (2014) or the slip weakening is rate-independent (e.g. Garagash and Germanovich, 2012) and can be modelled by transferring no normal and shear stresses (e.g. Ferronato et al., 2008) or by a sudden reduction of the coefficient of friction (e.g. Cappa and Rutqvist, 2011; Rutqvist et al., 2013).
We propose a different approach based on energetic considerations: During an earthquake, previously built-up stress is released and transformed into seismic wave energy, thermal energy resulting from friction on the fault plane and energy required to cause fracture (Kanamori,

2001). Thus, the shear stress on the fault plane is reduced. Following this, we can define the stress-drop $\Delta\sigma_{\text{failure}}$, that denotes the difference in stress before and after a slip event. Generally, this $\Delta\sigma_{\text{failure}}$ is considered to range from 0.1 - 1 MPa. Such a confined range of values for the stress-drop is not only assumed for large earthquakes (Aki, 1972; Thatcher and Hanks, 1973; Kanamori and Anderson, 1975) but observational data indicates that this is also true for small events (Abercrombie and Leary, 1993). This leads to a new conceptual idea for modelling shear failure on an existing fault: If the pressure margin p_{sm} for shear failure is surpassed, slip on the fault reduces the stress by a certain value. For simplicity, this might be assumed to be constant. The energies, into which the elastic energy is transformed, are either dissipated or negligible for the stress redistribution and thus they are considered as not relevant for the phenomena described by our model. Accordingly, it is proposed to model shear failure simply as a sink of elastic energy.

The onset of shear failure is defined by the respective criterion (Equation 2.89, 2.87) and will happen on a specific plane and almost instantly. To account for an instantaneous event, this is approximated by reducing the time-step size to a very small values, e.g. 0.01 seconds. The plane can be either be a predefined fault plane or alternatively determined from the friction angle using the worst case assumption (Equation 2.92). Equation 2.76 allows to transform the stress tensor $\boldsymbol{\sigma}$, which is formulated in the model with respect to Cartesian coordinates, into the stress state $\boldsymbol{\sigma}_{\text{fault}}$ in the direction of the fault plane:

$$\begin{pmatrix} \sigma_{x'} & \tau_{x'y'} \\ \tau_{x'y'} & \sigma_{y'} \end{pmatrix} = \begin{pmatrix} \cos\theta & \sin\theta \\ -\sin\theta & \cos\theta \end{pmatrix} \begin{pmatrix} \sigma_x & \tau_{xy} \\ \tau_{xy} & \sigma_y \end{pmatrix} \begin{pmatrix} \cos\theta & -\sin\theta \\ \sin\theta & \cos\theta \end{pmatrix}. \qquad \text{(2.76 revisited)}$$

Shear failure and the corresponding reduction in shear stress happens on these planes, so a predefined stress-drop value $\Delta\tau$ is subtracted from the shear stress:

$$\boldsymbol{\sigma}_{\text{fault, reduced}} = \begin{pmatrix} \sigma_{x'} & \tau_{x'y'} - \Delta\tau \\ \tau_{x'y'} - \Delta\tau & \sigma_{y'} \end{pmatrix} \tag{4.1}$$

The reduced stress tensor is then rotated back into Cartesian coordinates and replaces the original stress tensor. One could also think of this as a weakening of the shear modulus, as the element can carry less shear stress now. This results in a new deformation state, which is calculated using linear elasticity. Beck et al. (2016) put this weakening in the context of visco-elastic behaviour. While this can be helpful in describing the phenomenological effect of the stress-drop, testing experience has shown that the visco-elastic concept can also be limiting. This will be discussed for one of the test cases presented in the following.

Using a reduction in the excess shear stress to represent failure is a concept that is shared with recent approaches by Berge et al. (2017), Ucar et al. (2017) and Gómez Castro et al. (2017). These approaches all use linear elasticity, too, to calculate the deformation during failure.

When the shear failure criterion is surpassed, the shear stress is reduced until equilibrium is reached. That means that the reduction is equal to the amount of the excess shear stress. This is different from the approach presented here, where the constant stress-drop determines the reduction in shear stress. The difference comes down to the question whether one believes it is more realistic that fault reactivation stops as soon as equilibrium is reached or whether it reaches a stable state beyond the equilibrium after the stress dropped by a certain value.
The other notable difference is that the approach presented here describes failure as a subsequent process: Failure starts where the fault criterion is surpassed and the stress-drop is applied during the 0.01 seconds mentioned above. If this leads to further shear failure, the process is repeated at these locations. Alternatively, one could determine the extent of the fracture within one time-step iteratively or by formulating a minimisation problem as used in the works of Berge et al. (2017), Ucar et al. (2017) and Gómez Castro et al. (2017). In contrast to the question whether a constant stress drop or the equilibrium state determines the end of the fault reactivation, this variation of failure as an instantaneous and quasi-instantaneous process should not produce big differences.

4.2 Lab-scale numerical test cases

4.2.1 Homogeneous rock sample

The first scenario is inspired by the triaxial test case described in Subsection 2.2.4. A square rock sample with the dimension of 1 m x 1 m is compressed in the y-direction until shear failure occurs while being allowed to move freely in x-direction. The sample has homogeneous elastic properties (E= 1.0 GPa, $\nu = 0.2$). The example is intended to illustrate the mechanical behaviour during shear failure. For an easier interpretation, any hydraulic feedback onto the geomechanics is switched off by fixing the porosity to a constant value. So the pressure stays constant during the simulation, although the scenario uses the multi-phase flow and geomechanical model.
During the simulation, the increasing compression in the y-direction leads to higher normal stresses in y-direction, but does not induce any shear stresses in the x-y-direction. This means that the orientation of maximum principal stress σ_1 coincides with the y-axis and the one of the minimum principal stress σ_2 with the x-axis and both orientations stay constant. As the worst case assumption is used here, the friction angle of 10° gives an angle of 55° ($= 1/2 \cdot (90° + 10°)$, see Equation 2.92) for the failure plane respect to the y-axis (or σ_1, respectively).
Because of the assigned deformation rate at the top of $1.0 \cdot 10^{-6}$ m/s, the stresses on the fault plane increase and so does the potential for shear failure. At 4700 seconds, the shear

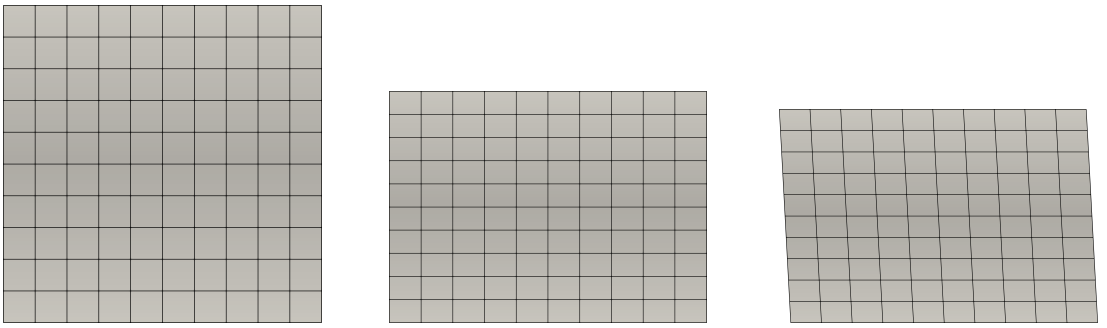

(a) Initial conditions ($t = 0$ s) **(b)** Before failure ($t = 4700$ s) **(c)** After failure ($t = 4700.01$ s)

Figure 4.1: Compression of a homogeneous rock sample: The deformation, multiplied by a factor of 50, is shown at initial conditions (a), before (b) and after shear failure (c) occurs at 4700 s.

failure criterion is surpassed. This happens for all elements at the same time as a result of the homogeneous boundary conditions and material parameters. The prescribed reduction of 1 MPa stress-drop shears the whole model domain (see Figure 4.1c) as each element is offset by small, similar-oriented faults.
While within itself plausible, it seems obvious that such a behaviour can be hardly observed for a realistic rock sample. This can be attributed to the fact that such a rock sample would contain impurities that would cause a locally confined failure nucleation.

4.2.2 Heterogeneous rock sample with a fault

This leads to our next scenario: Instead of homogeneous properties, the rock sample now contains a fault inclined by 55° with a higher Young's modulus of 5.0 GPa. The fault's Poisson ratio is 0.2. The properties of the surrounding matrix and the deformation rate stay the same. Again, the porosity is constant and the sample can move freely in x-direction. Similar to the homogeneous test case, Dirichlet boundary conditions fix the displacement in y-direction to zero at the bottom and the prescribed deformation rate of $1.0 \cdot 10^{-6}$ m/s at the top. Whether the grid has to factor in the fault's orientation, which would in turn require the fault's orientation to be known *a priori*, is tested: An equi-dimensional Cartesian grid is used, so the fault has to be represented by step-like material properties (see Figure 4.2a). As the fault is stiffer, the stress concentrates on the fault elements. As a result of the step-wise elements and the influence of the boundary conditions, the stress also varies within the fault. The fixed displacement at the top and bottom leads to the failure of the two elements at the fault tips (see Figure 4.2b) at $t = 1500$ seconds. As the stress-drop reduces the ability of these ruptured elements to carry the applied load, other elements of the fault are pushed towards failure.

Because of this stress redistribution and the continued compression, the rupture spreads from the tips towards the center (see Figure 4.2c and 4.2d). After $t = 1900.04$ seconds of simulation time, the central elements of the fault fail before their neighbours (see Figure 4.2e and 4.2f), which can be attributed to the stress redistribution within the step-like element of the fault. In summary, the rock sample experiences successive shear failure along the fault. When the fault has fully ruptured, the simulation stops.

4.2.3 Conclusions

The two examples illustrate the general capabilities of the approach and allow to check whether it produces plausible results. When elements surpass the shear failure criterion, their failure is represented by a stress-drop on the fault plane. This leads to a slip, similar to the effect a reduced friction angle would have. For a rather simple test case in the first scenario, the model produced a result that matches what one would expect from shear failure as a result of compression. The second example further tested the approach for plausibility: The stress concentrates on the fault within the sample, which then slips and offsets the sample. This even works for a fault that is represented rather crude with step-wise elements.
As pointed out in the introduction to this chapter, the aim of the approach is to model fault reactivation due to injections in the subsurface. The two examples offer little insight in this respect and one could even question whether the concept of finite-thickness elements for representing complex fault geometries is applicable to the scale of the presented test cases. But the intention of these examples was never to provide quantitative predictions on the laboratory scale. Nonetheless, the obtained results for these test cases are consistent and plausible and thus allow to confidently apply the approach to field-scale scenarios. In the following, we will present such a scenario of relevance for the previously mentioned applications and analyse the interaction of flow and geomechanics.

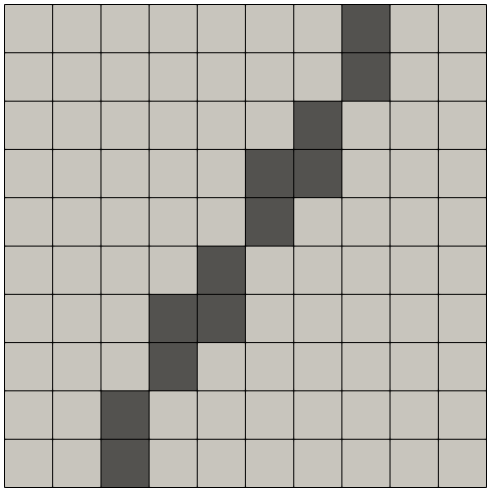

(a) Elastic properties of the rock sample:
$E_{\text{matrix}} = 1.0$ GPa, $\nu_{\text{matrix}} = 0.2$, (light grey)
$E_{\text{fault}} = 5.0$ GPa, $\nu_{\text{fault}} = 0.2$, (dark grey)

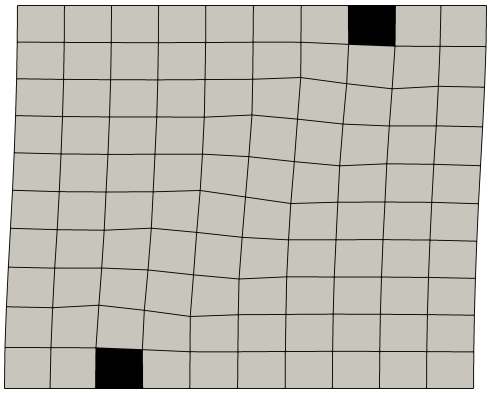

(b) Deformation, multiplied by a factor of 100, at the onset of failure at $t = 1500.01$ s. The failed elements are displayed in black.

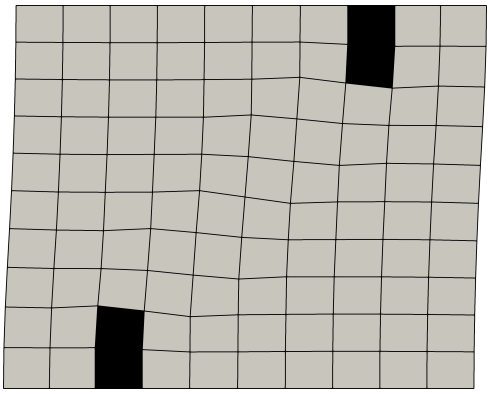

(c) Deformation, multiplied by a factor of 100, and failed elements (black) at $t = 1500.02$ s.

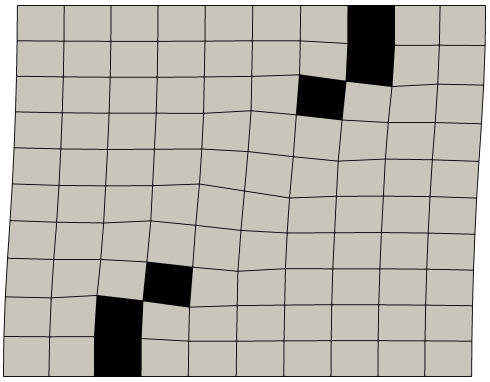

(d) Deformation, multiplied by a factor of 100, and failed elements (black) at $t = 1700.03$ s.

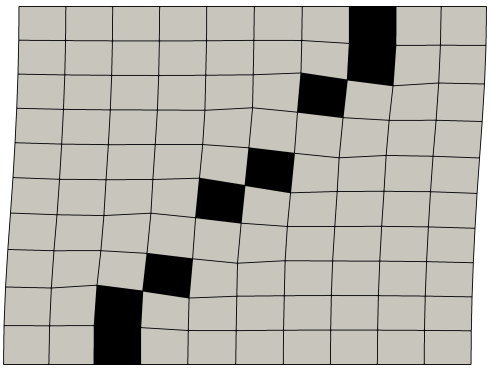

(e) Deformation, multiplied by a factor of 100, and failed elements (black) at $t = 1900.04$ s.

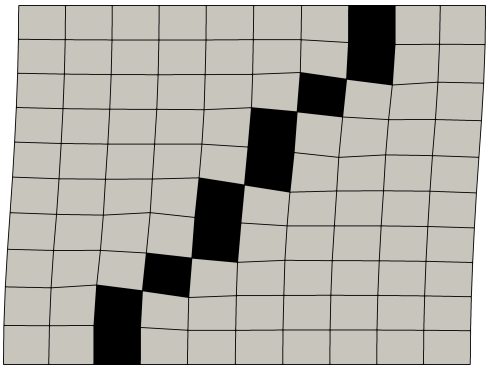

(f) Deformation, multiplied by a factor of 100, and failed elements (black) at $t = 1900.05$ s.

Figure 4.2: Compression of a heterogeneous rock sample.

4.3 Field-scale numerical test cases

4.3.1 Scenario description

In this section, the potential of injection-induced fault reactivation in the context of shale-gas hydraulic fracturing operations will be examined. The set-up is inspired by a scenario presented in Rutqvist et al. (2013).

A domain of 2 km × 2 km in size is used, which is located at a depth of 500 m to 2500 m. It comprises a shale formation and a fault of 1 km length, which cuts through the shale formation with a dip angle of 80°. The domain is discretised as illustrated by Figure 4.3. In contrast to the test case presented in Subsection 4.2.2, the grid follows the orientation of the fault. Similar to the scenario by Rutqvist et al. (2013), the initial pressure distribution in the system results from a hydrostatic pressure gradient (9.81 MPa/km) and an atmospheric pressure of 0.1 MPa at the surface. Except for the left boundary with Neumann no-flow conditions, the pressure at all other boundaries stays constant during the simulation. An initial temperature increase with depth from 22.5 °C to 72.5 °C is assigned. The values for the viscosity and the density are temperature-dependent, but the simulation itself is performed isothermally. For the right and the top boundary, the stress normal to those boundaries is set to a constant value, while for the left and bottom boundary, zero normal displacement is imposed (see Figure 4.3).

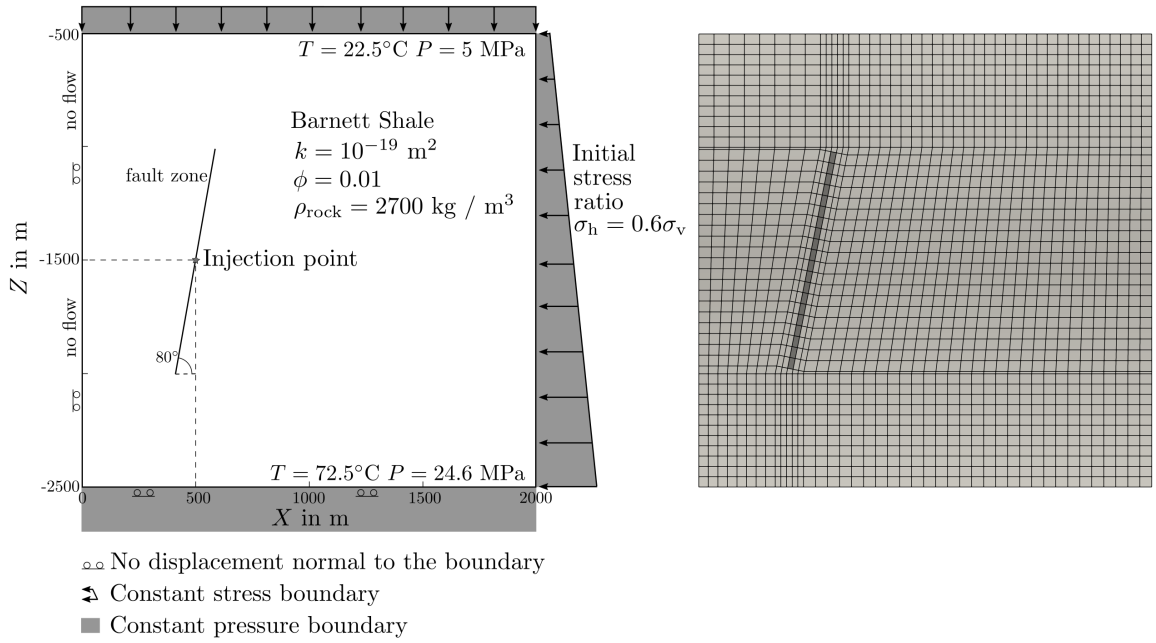

Figure 4.3: Set-up of the hydraulic fracturing scenario after Rutqvist et al. (2013) (left) and domain discretisation (right).

For the in situ stress field, the vertical stress is assumed to be the maximum principal stress corresponding with the significant depth of the domain, and the minimum principal stress is oriented horizontally and parallel to the injection well. The vertical stress gradient is calculated from the overburden density of 2700 kg/m^3 based on the assumed density of all formations overlying the shale formation. A horizontal-over-vertical stress ratio of $R = \sigma_\mathrm{h}/\sigma_\mathrm{v} = 0.6$ is used consistent with observations by Cipolla et al. (2010).
The material properties are listed in Table 4.1 and will be quickly summarised in the following: For the rock formations in the domain, a Young's modulus of 30 GPa and a Poisson ratio of 0.2 is chosen. These values are derived from laboratory measurements of the Barnett Shale from Tutuncu et al. (2010). The fault itself comprises of the elements marked in dark grey in Figure 4.3. Its Young's modulus is set to a significantly lower value of 5 GPa and zero cohesion was assigned. For the fault's coefficient of friction, the value of 0.6 assumed by Rutqvist et al. (2013) is taken. For the rock matrix, an initial porosity of 0.01 and a permeability $1 \cdot 10^{-19}$ m^2 is used. The fault's permeability is $1 \cdot 10^{-16}$ m^2 and has the same porosity.

Table 4.1: Material properties of the hydraulic fracturing scenario.

Parameters	Shale	Fault
Porosity, ϕ (-)	0.01	0.01
Rock density, ϱ_s (kg/m^3)	2700	2700
Permeability, k (m^2)	$1 \cdot 10^{-19}$	$5 \cdot 10^{-13}$
Young's modulus, E (GPa)	30	5
Poisson's ratio, ν (-)	0.20	0.25
Biot's coefficient α (-)	1	1
Cohesion (MPa)	-	0
Coefficient of friction, μ_frict (-)	-	0.6
stress-drop, $\Delta\sigma$ (MPa)	-	1.0

To simulate the effect of the hydraulic fracturing operations, water is injected into the fault at rate of 0.0033 kg/m^3/s at 1475 m depth. When shear failure occurs, the injection is stopped. The injection rate lies well within the range of plausible injection rates: As an example, Myers (2012) used a rate of 0.04 kg/m^3/s for modelling contaminant pathways while the original fault reactivation test case of Rutqvist et al. (2013) injected at rates between 1.0 - 3.5 $\cdot 10^{-3}$ kg/m^3/s.

4.3.2 Results

The pressure increase over time is shown in Figure 4.4a. After 0.75 h, fault reactivation occurs and the injection is switched off. In Figure 4.4b, the stress evolution on the fault is plotted: The increased pressure significantly reduces the effective stress σ' on the fault. For shear stress τ_{fault} on the fault, no change in shear stress τ is observable during the injection.

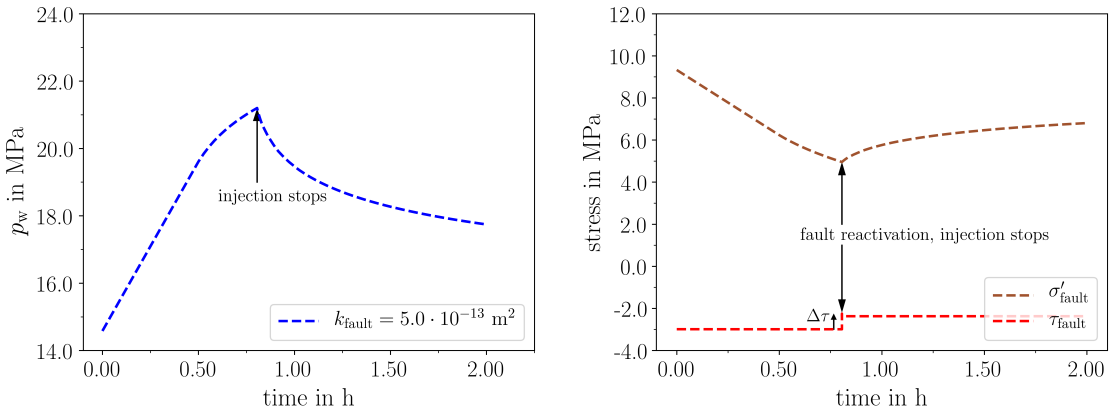

(a) Pressure over time.

(b) Stress over time.

Figure 4.4: Pressure and stress evolution over time at the injections cell in the fault in 1475 m depth for a fault permeability $k_{\text{fault}} = 5.0 \cdot 10^{-13}$ m^2.

The momentum balance equation is formulated in terms of the change in stress with respect to the initial state. A modification of the shear modulus as proposed in Beck et al. (2016) could only modify this additional stress and reduce it in the most extreme case to zero. But as no change in shear stress τ is observable (see Figure 4.4b), the concept of weakening of the shear modulus is not applicable. Instead, the prescribed stress-drop $\Delta\tau$ of 1.0 MPa is applied here directly to the total stresses (which include the dominating initial stresses for this scenario) as a sink in shear stress when shear failure occurs and the fault is reactivated. In the following, the processes leading to shear failure on the fault and what happens during the reactivation of the fault will be analysed in detail.

Figure 4.5a displays the pressure distribution along the fault at $t = 0$ s and at $t = 2900$ s. The initial pressure distribution shows an increase with depth. With time, the pressure peak resulting from the injection is superimposing this distribution. This is clearly visible for pressure curve plotted after 2900 s of injection.

As described in the beginning of this section, an increase in shear stress, a reduction of the normal stress or a higher pore pressure could lead to shear failure. The observed pressure increase and the respective reduction in effective normal stress on the fault causes exactly that: After 2900 s of injection, the critical pressure for shear failure p_{shear} reaches and surpasses

zero for the injection element (see Figure 4.5b), so shear failure occurs.

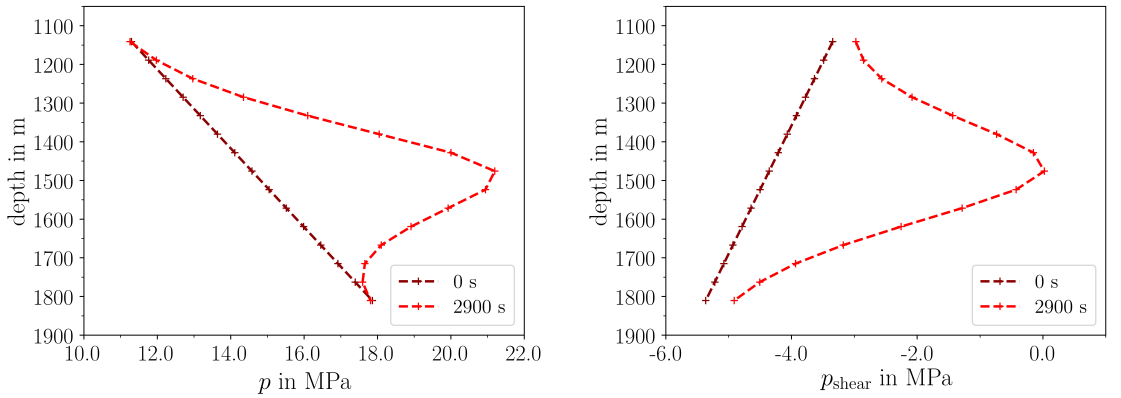

(a) Pressure distribution along the fault.

(b) Pressure margin for shear failure along the fault.

Figure 4.5: Pressure p and pressure margin p_{shear} for shear failure along fault at $t = 0$ s and at $t = 2900$ s.

In Figure 4.6, the stress-drop and the following stress redistribution along the fault is shown in detail. The shear stress in direction of the fault increases with depth as a result of the prescribed boundary conditions. The figure displays the distribution after 2900 s of injection when the criterion for shear failure is surpassed. This distribution is very similar to the initial distribution of the shear stress, as it does not change over time, a fact that was already covered in the description of Figure 4.4b.

There is no indication for the onset of shear failure in the shear stress distribution, as this is solely caused by the reduction in the effective normal stress described previously. The element at a depth of 1475 m then fails and the constant stress-drop $\Delta\tau$ of 1.0 MPa is applied. Due to the reduction, the shear stresses are redistributed (see curve for 2900.01 s). Especially the elements above and below the failed element experience an increase in shear stress. Despite of the increased shear stress, the element below is able to resist shear failure due to a higher normal stress resulting from the larger depth. In contrast, the element above the failed element is subjected to less normal stress and its shear failure criterion is surpassed. Consequently, the shear stress is also reduced for this element (see curve for 2900.02 s). After that, no further element surpasses the shear failure criterion and thus the fault reactivation comes to a halt.

In comparison the previously mentioned approach by Gómez Castro et al. (2017), at the detection of the first failing element, a system of equations is solved that checks by means of stresses calculated as a response to a unit force whether failure of further elements is triggered. This is repeated until equilibrium is reached. As explained in Section 4.1, this is different, as a stress-drop is used here instead, and similar, as the instantaneous and the quasi-instantaneous approach with 0.01 seconds should correspond with each other.

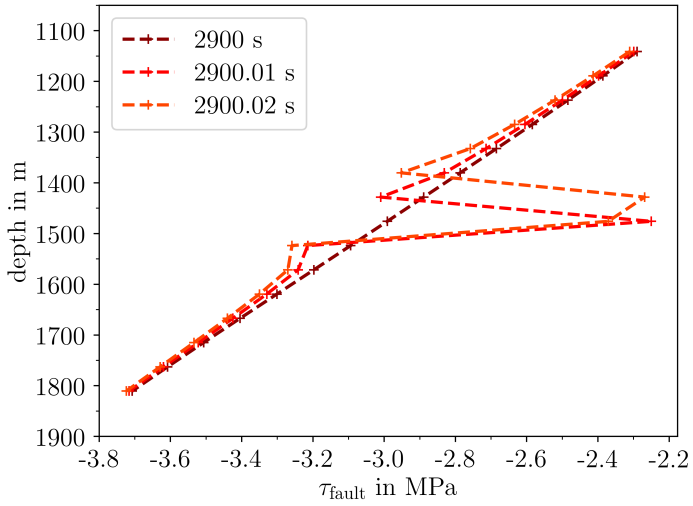

Figure 4.6: Shear stress changes within the fault during fault reactivation.

The resulting deformation state of the fault, exaggerated by a factor of 1000, is illustrated by Figure 4.7: Prior to the fault reactivation, the fault widened as a result of the pressure increase (see Figure 4.7a). After the fault reactivation, relative movement along the fault is visible: The left part has moved downward while the right part has moved up (see Figure 4.7b) and the failed elements (marked in dark grey) have been sheared.

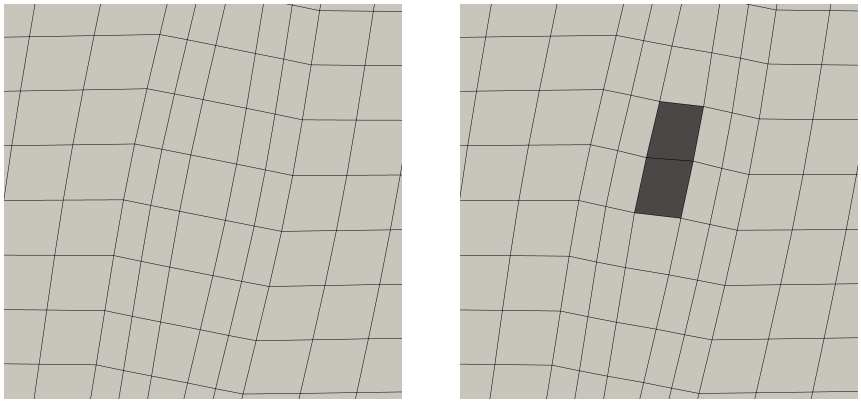

(a) Before fault reactivation. **(b)** After fault reactivation.

Figure 4.7: Deformation state around the injection, exaggerated by a factor of 1000.

To study this deformation in more detail, the displacement vector was rotated into the direction of the fault. Furthermore, the difference in displacement $\Delta u_{y'}$ in the y'-direction on the fault with respect to the displacement prior to fault reactivation was calculated. In Figure 4.8, these values are displayed in red colours for the nodes on the left side of the fault and in blue colours for nodes on the right side of the fault. This allows an analysis of the temporal evolution of the displacement: The already mentioned downward movement of the left and

the upward movement of the right side with respect to the displacement state at $t = 2900$ s before the fault was reactivated is clearly visible.
In nature, some portion of the fault slips while the remaining part, which did not fail, compensates the slip elastically. This effect can also be observed in our model: When the stress-drop was applied to the failing elements, these elements experienced an increased deformation in y'-direction, which also deformed the nearest neighbours to some extent. With increased distance, this effect becomes less pronounced.

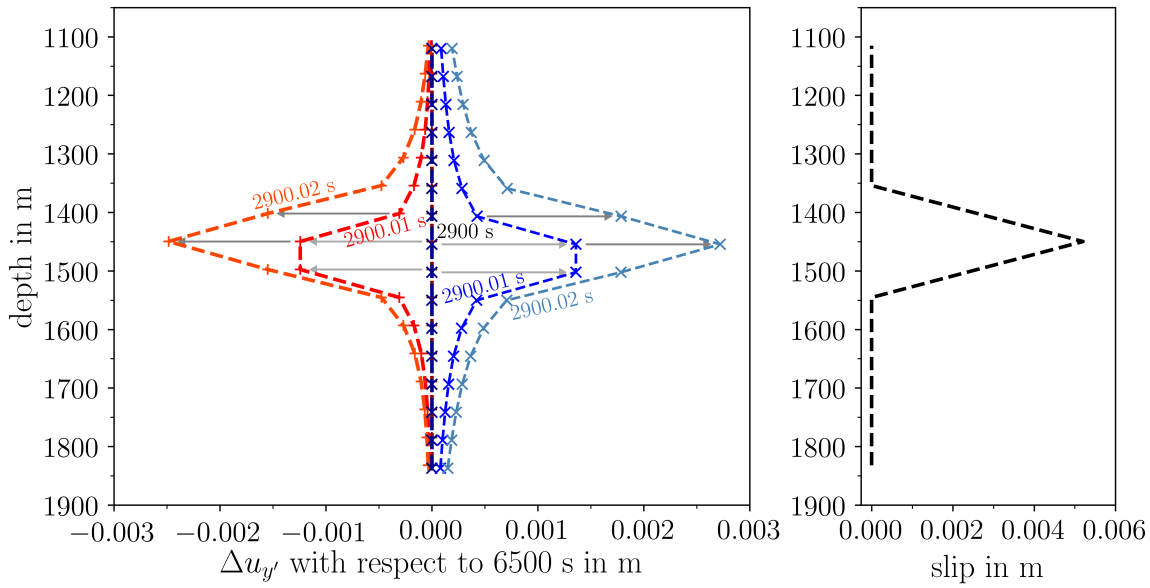

Figure 4.8: Difference in displacement $\Delta u_{y'}$ in the y'-direction on the fault with respect to the displacement prior to fault reactivation (left). For failed elements, the slip is calculated from difference between the displacement on the right and on the left side (grey arrows on the left, plot on the right).

To estimate the strength of the induced seismicity, the relative displacement of previously adjacent points on the fault surface - also referred to as the slip - has to be determined. The fault was not modelled as a surface but as a fault zone instead, which brings up the question of how to calculate the slip in this case. For failed elements, it is assumed that they displaced along ubiquitous joints within the fault zone. So the difference between the displacement on the right and on the left side can be taken as a measure of the slip on those joints. For non-failed elements in contrast, elastic deformation instead of an offset is assumed. Following this, the displacements of the nodes of a failed element are taken into account to calculate the slip for the presented scenario. The contributions of the nodes belonging to the two failing cells at $t = 2900.01$ s and $t = 2900.02$ s are marked with grey arrows in Figure 4.8 and are summed up to the slip.

Kanamori and Brodsky (2004) provide a convenient measure for the size of an earthquake: First, one determines the seismic moment M_0

$$M_0 = G\,A\,s \tag{4.2}$$

from the shear modulus G, the mean slip s and the rupture area A. The moment magnitude M can then be determined using

$$M = (\log_{10} M_0 - 9.1)/1.5. \tag{4.3}$$

Following Rutqvist et al. (2013), the area A is calculated from the rupture length using the assumption of a circular rupture patch. A rupture length of 200 m, a shear modulus of 2.0 GPa and a mean slip of 0.0026 m then gives a moment magnitude $M = 1.41$.

4.3.3 Effect of the permeability

The mechanism that leads to fault reactivation in the scenario is the pressure increase and corresponding reduction in normal stress. The permeability of the fault will highly affect the shape of the pressure peak. Thus, two sub-scenarios, one with a higher and another with a lower fault permeability, namely $k_{\text{fault}} = 1.0 \cdot 10^{-13}$ m^2 and $k_{\text{fault}} = 1.0 \cdot 10^{-12}$ m^2, will be presented in what follows.
Figure 4.9 displays the pressure evolution over time for these scenarios in comparison to the already presented case with $k_{\text{fault}} = 5.0 \cdot 10^{-13}$. Again, the injection is switched off when shear failure starts. This happens at different times for the scenarios: For the low permeability case, the criterion for shear failure is surpassed after only 1600 s of injection, while the injection phase lasts for 4100 s seconds for the high permeability case. This is related to the permeability controlling the pressure increase in the fault. The less permeable the fault is, the faster the pressure increases.

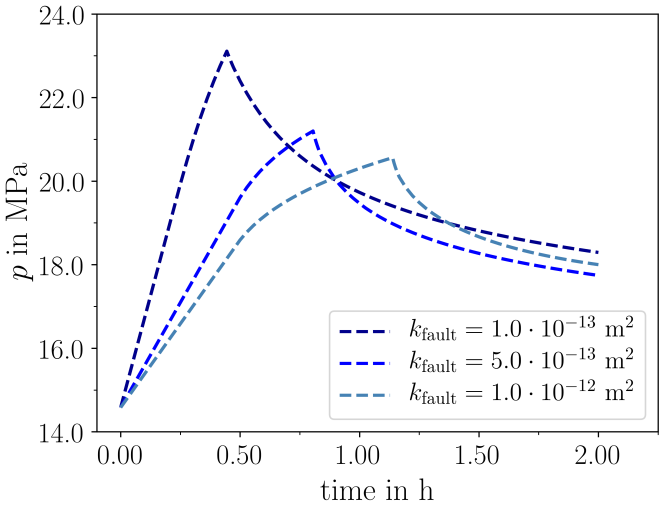

Figure 4.9: Pressure evolution over time for different fault permeabilities.

The permeability also influences the pressure distribution in the fault and thus the pressure margin for shear failure, which is shown in Figure 4.10a and 4.10b. Lower permeabilities lead to higher pressure gradients. As a result, the injection pressurises only the central section of the fault for the low permeability case, while the injection raised the pressure significantly over the whole length of the fault for the high permeability case.

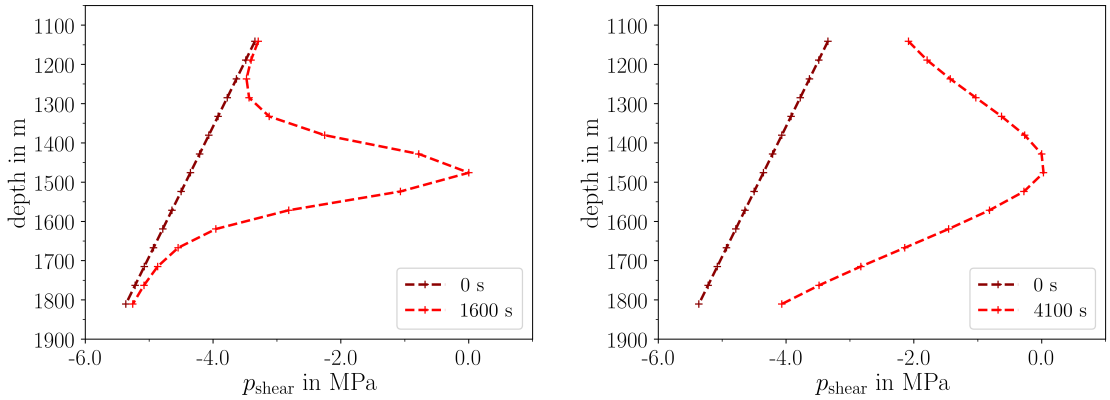

(a) Distribution of the pressure margin for shear failure along the fault for a permeability of $k_{\text{fault}} = 1.0 \cdot 10^{-13}$ m^2 .

(b) Distribution of the pressure margin for shear failure along the fault for a permeability of $k_{\text{fault}} = 1.0 \cdot 10^{-12}$ m^2.

Figure 4.10: Pressure and stress evolution over time at the injections cell (coordinates of the cell center: 505, 1475).

In comparison with the previously presented test case, this produces a different fault reactivation pattern: For the low permeability scenario, only the injection cell fails and an average slip of

0.0016 m is produced (see Figure 4.11a). For the high permeability scenario however, four elements fail, which results in 0.0032 m of averaged slip. Thus, the corresponding earthquake magnitudes vary from 1.10 to 1.70 (calculated using the previously made assumptions).

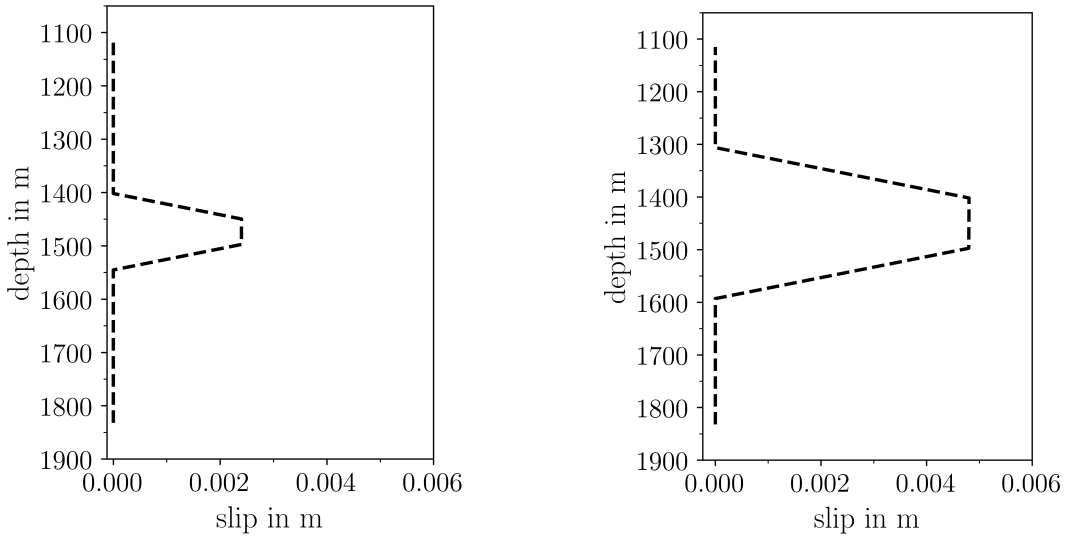

(a) Fault permeability $k_{\text{fault}} = 1.0 \cdot 10^{-13}$ m^2.

(b) Fault permeability $k_{\text{fault}} = 1.0 \cdot 10^{-12}$ m^2.

Figure 4.11: Slip after fault reactivation for varying permeabilities.

4.3.4 Conclusions

The developed approach was used to model a field-scale test case. This allows to demonstrate the applicability of the approach to a scenario of relevance for real-life applications. Unfortunately, a direct comparison of the results presented here with the ones published in Rutqvist et al. (2013) could not be realized as the latter where obtained by using a sequential coupling of TOUGH2 and FLAC3D with just one coupling step. As discussed extensively in Chapter 3, this does not represent the interaction between flow and geomechanics as accurate as a fully-coupled scheme or an iterated sequential scheme such as the fixed-stress scheme. This in turn will affect the onset of shear failure and prevents a direct comparison of parameters characteristic for the fault reactivation.

Nonetheless, the scenario allows insight into the relevant processes that lead to fault reactivation and how strong seismicity could potentially be avoided. One important finding in this context is that the reduction in normal stresses as result of the pressure increase is the key process that leads to shear failure for the presented scenario. Obviously, this is related to the shear stress distribution, which was already present before the injection started. But reactivation of already critically stressed faults by injecting fluids should not be dismissed as

an unrealistic and artificial scenario: A report on the observed seismicity in the area of the Horn River Basin in British Columbia, Canada by the BC Oil and Gas Commission covers the series of 38 seismic events in range of magnitude 2.2 to 3.8 on the Richter scale between 2009 and 2011. It comes to the conclusion that the events "were caused by fluid injection during hydraulic fracturing in proximity to pre-existing faults" (British Columbia Oil and Gas Commission, 2012), a description that sounds remarkably similar to what happened in our test case.

The variation of the fault's permeability offers another notable finding: Despite the slower pressure increase and a lower maximum pressure, injecting into a higher permeable fault is actually worse in terms of the resulting seismicity. This supports the claim of Ellsworth (2013) (mentioned in the introduction of this chapter) to improve the reporting of hydraulic data, as for instance a simple threshold value for the maximum pressure would not allow a detection of the imminent potential of fault reactivation in such a case.

5 Summary

As pointed out in the introduction, the interaction of flow and geomechanics in porous media is relevant for several applications that inject fluids into the subsurface, for example for the disposal of waste-water, for hydraulic fracturing and for CO_2 injections. In this context, this work presents volume-based conceptual approaches for the analysis of coupled hydraulic and geomechanical processes.
The individual physical concepts to describe flow in porous media and rock mechanics are described in the second chapter and can be linked using the theory of poroelasticity. This framework takes the contributions of the solid, the fluid and the pore space to the hydraulic and geomechanical processes into account by defining effective parameters such as the effective stress, the effective porosity, the effective permeability and the effective pressure. Furthermore, the Mohr circle and the Mohr–Coulomb failure criterion allow an evaluation of how prone a system is to failure.

The chapter on modelling flow and geomechanics outlined how the physical concepts can be incorporated to formulate balance equations for flow and geomechanics. The resulting partial differential equations were transformed into their discretised form to tackle them numerically. Different solution strategies can be then employed to solve these discretised balance equations. The following key questions were identified: Is it advantageous in terms of accuracy and efficiency to solve the coupled system all at once in a fully-coupled manner? And, if one decides to do the contrary, namely splitting the coupled system and solving flow and geomechanics one after another, i.e. sequentially, how is this split to be realised and what is a suitable way to transfer information between the parts? Does one need to perform several iterations of the sequential solutions?
In this sense, a fully-coupled approach, a pragmatic sequential approach without iterations conceptually similar to a scheme realised in the TOUGH-FLAC software and a sophisticated iterative sequential approach – the fixed stress scheme – are implemented within the open-source software DuMu$^{\text{x}}$. This allows to study the questions posed above and to test the hypothesis formulated in the introduction of this work that the fully-coupled approach is the only approach that combines accuracy and efficiency.

The following chapter further expands the scope of this thesis to the reactivation of faults and resulting earthquakes. Recently, earthquakes have occurred in unusual locations and have been linked to fluid injections, thus a better understanding of the interacting hydraulic and geomechanical processes that could lead to such earthquakes is key to avoid them in the first place. This work contributes to that by proposing a new volume-based approach to model the shear failure process in a fault zone. This involves two aspects: The way the fault zone is discretised and how the failure process is modelled. Regarding the latter, it is undisputed that during an earthquake, previously stored shear stress is released. There is also evidence that the reduction in shear stress – the stress drop – is bounded and does not depend on the scale of the earthquake. Thus, the proposed approach uses the stress drop as a characteristic parameter to model the reactivation of the fault. With respect to the discretisation, a volume-based representation is given preference over a representation as a surface. The corresponding hypothesis formulated in the introduction has been tested by discussing in which respect the approach is similar or not to other existing concepts. Several numerical test cases also test the hypothesis for plausibility and allow insights into the mechanisms that lead to shear failure in the fault zone.

5.1 Conclusions and Outlook

Modelling flow and geomechanics in porous media Solving the flow and then the mechanics once for each time-step and approximating the porosity change within the flow problem by the pore compressibility gives an efficient and easily implementable scheme. The results for the different implementations of this conceptual model in DuMu^{x} and TOUGH-FLAC match each other for the presented numerical test case, which serves as a model verification in the sense of Oberkampf and Trucano (2002).

This scheme can be expanded by the fixed-stress split, which allows to transform the approach into an iterative sequential scheme. In addition, one can show that a fixed-stress scheme with zero iterations is identical to pore compressibility implementation described above. Applying this zero-iteration fixed-stress scheme and the iterated one to different numerical test cases also simulated with the fully-coupled approach revealed that several iterations are needed for the iterated fixed-stress scheme to converge to the fully-coupled solution. Performing only one coupling-step – alias the zero-iteration fixed-stress scheme – leads to considerable deviations relative to the fully-coupled solution as transient effects are not captured accurately.

A comparison of the computational effort of the direct linear solver for each scheme showed that the advantage of the sequential scheme by solving two smaller linear systems of equations instead of a large one in the fully-coupled case is used up by the fact, that several iterations need to be performed to achieve the same accuracy. In this sense, the hypothesis stated

in the introduction, namely that efficient simulations of coupled flow and geomechanics without sacrificing accuracy require to solve the balance equations in a fully-coupled way, is corroborated. Which model is truly best suited is hard to answer unambiguously. Nonetheless, depending on one's need for accuracy, using the zero-iteration fixed-stress scheme might be sufficient. Since the gain in accuracy with just one iteration is considerable, running the fixed-stress scheme with one iteration could be a good compromise.
Future work could focus on improving the existing solution strategies. By replacing the direct solver with an iterative solver such as the algebraic multigrid (Stüben, 1999), the sequential scheme's advantage by solving a smaller system of linear equations would vanish in theory. Applying the fixed-stress as a pre-conditioner as proposed by White and Borja (2011) could increase the efficiency of the fully-coupled approach even more.
Both et al. (2018) applied the fixed-stress scheme to a sequential scheme coupling linear elasticity and flow in unsaturated porous media modelled by the Richards equation. As they encountered difficulties when using Newton's method, they propose to use the L-scheme for the Richards equation, which can be described as a standard Picard iteration with additional diagonal stabilisation, resulting in an efficient and robust decoupling of the equations for geomechanics and flow. The same group also developed an optimized tuning parameter, which depends on all mechanical parameters and replaces the classically used drained bulk modulus in the fixed-stress scheme Both et al. (2017). These are promising new developments that could be incorporated into the existing approaches.

Fault reactivation The hypothesis, that the process of fault reactivation can be represented in a meaningful way by the stress drop as the characteristic parameter is backed up by that fact that observations indicate a stress drop confined to a small range for earthquakes of various sizes (Aki, 1972; Thatcher and Hanks, 1973; Kanamori and Anderson, 1975; Abercrombie and Leary, 1993). Incorporating this into the existing fully-coupled approach for flow and geomechanics produces consistent and plausible results and allows for a detailed analysis of the processes leading to fault reactivation. A key finding in that respect is that the fault's permeability strongly affects the final rupture length and thus the seismic magnitude: Expectedly, the pressure increase is less pronounced the higher the fault zone's permeability is for the presented numerical test case. But this could lull an operator into a false sense of security, since for a higher permeability a larger portion of the fault is pressurised and prone to rupture, leading to a larger earthquake.
The scenario was inspired by a set-up published by Rutqvist et al. (2013). A comparison with their results could not be realized since they were obtained using a sequential coupling of TOUGH2 and FLAC3D with zero iterations and thus different from the fully-coupled approach. Modularising the fault reactivation implementation to make also available for the sequential

scheme would be desirable. Equally as promising would be a comparison with other recent approaches by Berge et al. (2017), Ucar et al. (2017) and Gómez Castro et al. (2017), which share the concept of using a reduction in the excess shear stress to represent failure. For these models, the shear stress is decreased until equilibrium is reached and not by a constant value as in our proposed approach. Nonetheless, the implementation in DuMu^{x} certainly allows to adapt the model conceptionally in this regard to enable a comparison and possibly a verification of the implementations.

Bibliography

R. Abercrombie and P. Leary. Source parameters of small earthquakes recorded at 2.5 km depth, Cajon Pass, southern California: Implications for earthquake scaling. *Geophysical Research Letters*, 20(14):1511–1514, 1993. doi:10.1029/93GL00367.

S. Ackermann, M. Beck, B. Becker, H. Class, T. Fetzer, B. Flemisch, D. Gläser, C. Grüninger, K. Heck, R. Helmig, J. Hommel, A. Kissinger, T. Koch, M. Schneider, G. Seitz, and K. Weishaupt. Dumux 2.11.0. Mar. 2017. doi:10.5281/zenodo.439488.

U. E. I. Administration. Haynesville surpasses Barnett as the nations leading shale play, 2011. URL https://www.eia.gov/todayinenergy/detail.php?id=570. Online; accessed January 29, 2019.

K. Aki. Earthquake mechanism. *Tectonophysics*, 13(1):423 – 446, 1972. ISSN 0040-1951. doi:10.1016/0040-1951(72)90032-7.

M. Alkämper, A. Dedner, R. Klöfkorn, and M. Nolte. The DUNE-ALUGrid Module. *Archive of Numerical Software*, 4(1):1–28, 2016. ISSN 2197-8263. doi:10.11588/ans.2016.1.23252.

P. Bastian, M. Blatt, A. Dedner, C. Engwer, R. Klöfkorn, R. Kornhuber, M. Ohlberger, and O. Sander. A generic grid interface for parallel and adaptive scientific computing. Part II: implementation and tests in DUNE. *Computing*, 82(2):121–138, Jul 2008a. ISSN 1436-5057. doi:10.1007/s00607-008-0004-9.

P. Bastian, M. Blatt, A. Dedner, C. Engwer, R. Klöfkorn, M. Ohlberger, and O. Sander. A generic grid interface for parallel and adaptive scientific computing. Part I: abstract framework. *Computing*, 82(2):103–119, Jul 2008b. ISSN 1436-5057. doi:10.1007/s00607-008-0003-x.

J. Bear. *Dynamics of Fluids in Porous Media*. Dover Civil and Mechanical Engineering Series. Dover Publications, 1988. ISBN 9780486656755.

M. Beck, G. Seitz, and H. Class. Volume-Based Modelling of Fault Reactivation in Porous Media Using a Visco-Elastic Proxy Model. *Transport in Porous Media*, 114(2):505–524, Sep 2016. ISSN 1573-1634. doi:10.1007/s11242-016-0663-5.

R. L. Berge, I. Berre, and E. Keilegavlen. Reactivation of fractures in subsurface reservoirs-a numerical approach using a static-dynamic friction model. *arXiv preprint arXiv:1712.06032*, 2017.

J. T. Birkholzer, Q. Zhou, and C.-F. Tsang. Large-scale impact of CO_2 storage in deep saline aquifers: A sensitivity study on pressure response in stratified systems. *International Journal of Greenhouse Gas Control*, 3(2):181 – 194, 2009. ISSN 1750-5836. doi:10.1016/j.ijggc.2008.08.002.

L. Blanco-Martín, J. Rutqvist, and J. T. Birkholzer. Extension of tough-flac to the finite strain framework. *Computers & Geosciences*, 108:64 – 71, 2017. ISSN 0098-3004. doi:10.1016/j.cageo.2016.10.015. TOUGH Symposium 2015: recent enhancements to the TOUGH family of codes and coupled flow and geomechanics processes modeling.

M. Blatt and P. Bastian. The Iterative Solver Template Library. In B. Kågström, E. Elmroth, J. Dongarra, and J. Waśniewski, editors, *Applied Parallel Computing. State of the Art in Scientific Computing*, pages 666–675, Berlin, Heidelberg, 2007. Springer Berlin Heidelberg. ISBN 978-3-540-75755-9.

M. Blatt, A. Burchardt, A. Dedner, C. Engwer, J. Fahlke, B. Flemisch, C. Gersbacher, C. Gräser, F. Gruber, C. Grüninger, D. Kempf, R. Klöfkorn, T. Malkmus, S. Müthing, M. Nolte, M. Piatkowski, and O. Sander. The Distributed and Unified Numerics Environment, Version 2.4. *Archive of Numerical Software*, 4(100):13–29, 2016. ISSN 2197-8263. doi:10.11588/ans.2016.100.26526.

J. W. Both, M. Borregales, J. M. Nordbotten, K. Kumar, and F. A. Radu. Robust fixed stress splitting for Biot's equations in heterogeneous media. *Applied Mathematics Letters*, 68:101 – 108, 2017. ISSN 0893-9659. doi:10.1016/j.aml.2016.12.019.

J. W. Both, K. Kumar, J. M. Nordbotten, and F. A. Radu. Anderson accelerated fixed-stress splitting schemes for consolidation of unsaturated porous media. *Computers & Mathematics with Applications*, 2018. ISSN 0898-1221. doi:10.1016/j.camwa.2018.07.033.

C. Bousige, C. M. Ghimbeu, C. Vix-Guterl, A. E. Pomerantz, A. Suleimenova, G. Vaughan, G. Garbarino, M. Feygenson, C. Wildgruber, F.-J. Ulm, et al. Realistic molecular model of kerogen's nanostructure. *Nature materials*, 15(5):576–582, 2016. doi:10.1038/nmat4541.

British Columbia Oil and Gas Commission. *Investigation of observed seismicity in the Horn River Basin*. British Columbia Oil and Gas Commission, 2012.

R. H. Brooks and A. T. Corey. Hydraulic Properties of Porous Media. *Hydrology Papers, Colorado State University*, (March), 1964.

F. Cappa and J. Rutqvist. Modeling of coupled deformation and permeability evolution during fault reactivation induced by deep underground injection of CO_2. *International Journal of Greenhouse Gas Control*, 5(2):336 – 346, 2011. ISSN 1750-5836. doi:https://doi.org/10.1016/j.ijggc.2010.08.005.

P. C. Carman. Fluid flow through granular beds. *Transactions, Institution of Chemical Engineers*, 15:150–166, 1937.

M. A. Celia and P. Binning. A mass conservative numerical solution for two-phase flow in porous media with application to unsaturated flow. *Water Resources Research*, 28(10): 2819–2828, 1992. doi:10.1029/92WR01488.

G. R. Chalmers, R. M. Bustin, and I. M. Power. Characterization of gas shale pore systems by porosimetry, pycnometry, surface area, and field emission scanning electron microscopy/transmission electron microscopy image analyses: Examples from the Barnett, Woodford, Haynesville, Marcellus, and Doig units. *AAPG bulletin*, 96(6):1099–1119, 2012.

C. Chang, M. D. Zoback, and A. Khaksar. Empirical relations between rock strength and physical properties in sedimentary rocks. *Journal of Petroleum Science and Engineering*, 51 (3):223 – 237, 2006. ISSN 0920-4105. doi:https://doi.org/10.1016/j.petrol.2006.01.003.

Z. Chen, G. Huan, and Y. Ma. *Computational Methods for Multiphase Flows in Porous Media*. Society for Industrial and Applied Mathematics, 2006. doi:10.1137/1.9780898718942.

P. Churcher, P. French, J. Shaw, L. Schramm, et al. Rock properties of Berea Sandstone, Baker Dolomite, and Indiana Limestone. In *SPE International Symposium on Oilfield Chemistry*. Society of Petroleum Engineers, 1991. doi:10.2118/21044-MS.

C. L. Cipolla, E. P. Lolon, J. C. Erdle, B. Rubin, et al. Reservoir modeling in shale-gas reservoirs. *SPE reservoir evaluation & engineering*, 13(04):638–653, 2010. doi:10.2118/125530-MS.

H. Class. *Theorie und numerische Modellierung nichtisothermer Mehrphasenprozesse in NAPL-kontaminierten porösen Medien*. PhD thesis, Universität Stuttgart, Holzgartenstr. 16, 70174 Stuttgart, 2001. URL https://elib.uni-stuttgart.de/handle/11682/240.

H. Class, A. Ebigbo, R. Helmig, J. M. Dahle, Helge K.and Nordbotten, M. A. Celia, P. Audigane, M. Darcis, J. Ennis-King, Y. Fan, B. Flemisch, S. E. Gasda, M. Jin, S. Krug, D. Labregere, A. Naderi Beni, R. J. Pawar, A. Sbai, S. G. Thomas, L. Trenty, and L. Wei. A benchmark study on problems related to CO_2 storage in geologic formations. *Computational Geosciences*, 13(4):409, Jul 2009. ISSN 1573-1499. doi:10.1007/s10596-009-9146-x.

M. Y. Darcis. *Coupling models of different complexity for the simulation of CO_2 storage in deep saline aquifers*. PhD thesis, Universität Stuttgart, Holzgartenstr. 16, 70174 Stuttgart, 2013. URL http://elib.uni-stuttgart.de/opus/volltexte/2013/8141.

J. Davies and D. Davies. Stress-dependent permeability: characterization and modeling. In *SPE Annual Technical Conference and Exhibition, 3-6 October, Houston, Texas*. Society of Petroleum Engineers, 1999. doi:10.2118/56813-MS.

K. de Rijke. Hydraulically fractured: Unconventional gas and anthropology. *Anthropology Today*, 29(2):13–17, 2013. doi:10.1111/1467-8322.12017.

N. Deichmann and D. Giardini. Earthquakes Induced by the Stimulation of an Enhanced Geothermal System below Basel (Switzerland). *Seismological Research Letters*, 80(5):784, 2009. doi:10.1785/gssrl.80.5.784.

E. Detouray and A. H.-D. Cheng. Fundamentals of Poroelasticity. In C. Fairhurst, editor, *Analysis and Design Methods*, pages 113 – 171. Pergamon, Oxford, 1993. ISBN 978-0-08-040615-2. doi:https://doi.org/10.1016/B978-0-08-040615-2.50011-3.

C. G. Dyke and L. Dobereiner. Evaluating the strength and deformability of sandstones. *Quarterly Journal of Engineering Geology and Hydrogeology*, 24(1):123, 1991. doi:10.1144/GSL.QJEG.1991.024.01.13.

W. L. Ellsworth. Injection-Induced earthquakes. *Science*, 341(6142), 2013. ISSN 0036-8075. doi:10.1126/science.1225942.

M. Ferronato, G. Gambolati, C. Janna, and P. Teatini. Numerical modelling of regional faults in land subsidence prediction above gas/oil reservoirs. *International Journal for Numerical and Analytical Methods in Geomechanics*, 32(6):633–657, 2008. doi:10.1002/nag.640.

T. Fetzer, B. Becker, B. Flemisch, D. Gläser, K. Heck, T. Koch, M. Schneider, S. Scholz, and K. Weishaupt. Dumux 2.12.0. Dec. 2017. doi:10.5281/zenodo.1115500.

B. Flemisch, M. Darcis, K. Erbertseder, B. Faigle, A. Lauser, K. Mosthaf, S. Müthing, P. Nuske, A. Tatomir, M. Wolff, and R. Helmig. DuMux: DUNE for multi-{phase,component,scale,physics,...} flow and transport in porous media. *Advances in Water Resources*, 34(9):1102 – 1112, 2011. ISSN 0309-1708. doi:10.1016/j.advwatres.2011.03.007.

P. Forsyth. A control volume finite element approach to napl groundwater contamination. *SIAM Journal on Scientific and Statistical Computing*, 12(5):1029–1057, 1991. doi:10.1137/0912055. URL https://doi.org/10.1137/0912055.

C. Frohlich, W. Ellsworth, W. A. Brown, M. Brunt, J. Luetgert, T. MacDonald, and S. Walter. The 17 May 2012 M4.8 earthquake near Timpson, East Texas: An event possibly triggered by fluid injection. *Journal of Geophysical Research: Solid Earth*, 119(1):581–593, 2014. doi:10.1002/2013JB010755. URL https://agupubs.onlinelibrary.wiley.com/doi/abs/10.1002/2013JB010755.

D. I. Garagash and L. N. Germanovich. Nucleation and arrest of dynamic slip on a pressurized fault. *Journal of Geophysical Research: Solid Earth (1978–2012)*, 117(B10), 2012.

G. H. Golub and C. F. van Loan. *Matrix computations*, volume 3. JHU Press, 2012.

B. M. Gómez Castro, S. De Simone, and J. Carrera. A new method to simulate shear and tensile failure due to hydraulic fracturing operations. In *EGU General Assembly Conference Abstracts*, volume 19 of *EGU General Assembly Conference Abstracts*, page 8657, apr 2017.

K. B. Gregory, R. D. Vidic, and D. A. Dzombak. Water Management Challenges Associated with the Production of Shale Gas by Hydraulic Fracturing. *Elements*, 7(3):181, 2011. doi:10.2113/gselements.7.3.181. URL http://dx.doi.org/10.2113/gselements.7.3.181.

J. Grotzinger and T. H. Jordan. *Understanding Earth*. W. H. Freeman, 2010. ISBN 9781429219518. URL https://books.google.de/books?id=aT-sB8JC5O0C.

G. Han and M. B. Dusseault. Description of fluid flow around a wellbore with stress-dependent porosity and permeability. *Journal of Petroleum science and engineering*, 40(1):1–16, 2003.

D. J. Hart and H. F. Wang. Laboratory measurements of a complete set of poroelastic moduli for Berea Sandstone and Indiana Limestone. *Journal of Geophysical Research: Solid Earth*, 100(B9):17741–17751, 1995.

R. Helmig. *Multiphase flow and transport processes in the subsurface: A contribution to the modeling of hydrosystems.* Springer-Verlag, 1997.

A. A. Holland. Earthquakes triggered by hydraulic fracturing in south-central Oklahoma earthquakes triggered by hydraulic fracturing in south-central Oklahoma. *Bulletin of the Seismological Society of America*, 103(3):1784, 2013. doi:10.1785/0120120109. URL http://dx.doi.org/10.1785/0120120109.

S. Horton. Disposal of hydrofracking waste fluid by injection into subsurface aquifers triggers earthquake swarm in central Arkansas with potential for damaging earthquake. *Seismological Research Letters*, 83(2):250, 2012. doi:10.1785/gssrl.83.2.250. URL http://dx.doi.org/10.1785/gssrl.83.2.250.

J. A. Hudson and J. P. Harrison. *Engineering Rock Mechanics*. Pergamon, Oxford, 1st edition edition, 1997. ISBN 978-0-08-043864-1. doi:https://doi.org/10.1016/B978-008043864-1/50000-8. URL https://www.sciencedirect.com/science/article/pii/B9780080438641500008.

International Energy Agency (IEA). *Global Energy and CO_2 Status Report*. 2018. URL https://www.iea.org/geco.

R. B. Jackson, A. Vengosh, T. H. Darrah, N. R. Warner, A. Down, R. J. Poreda, S. G. Osborn, K. Zhao, and J. D. Karr. Increased stray gas abundance in a subset of drinking water wells near marcellus shale gas extraction. *Proceedings of the National Academy of Sciences*, 110(28):11250–11255, 2013. ISSN 0027-8424. doi:10.1073/pnas.1221635110. URL http://www.pnas.org/content/110/28/11250.

J. C. Jaeger and N. G. W. Cook. *Fundamentals of Rock Mechanics*. Champman & Hall, London, 2 edition, 1976. ISBN 0412214105.

B. Jha and R. Juanes. Coupled multiphase flow and poromechanics: A computational model of pore pressure effects on fault slip and earthquake triggering. *Water Resources Research*, 50(5):3776–3808, 2014.

R. Juanes, B. H. Hager, and H. J. Herzog. No geologic evidence that seismicity causes fault leakage that would render large-scale carbon capture and storage unsuccessful. *Proceedings of the National Academy of Sciences*, 109(52):E3623–E3623, 2012. ISSN 0027-8424. doi:10.1073/pnas.1215026109. URL http://www.pnas.org/content/109/52/E3623.

H. Kanamori. Chapter 11 energy budget of earthquakes and seismic efficiency. In R. Teisseyre and E. Majewski, editors, *Earthquake Thermodynamics and Phase Transformations in the Earth's Interior*, volume 76 of *International Geophysics*, pages 293 – 305. Academic Press, 2001. doi:http://dx.doi.org/10.1016/S0074-6142(01)80087-5. URL http://www.sciencedirect.com/science/article/pii/S0074614201800875.

H. Kanamori and D. L. Anderson. Theoretical basis of some empirical relations in seismology. *Bulletin of the Seismological Society of America*, 65(5):1073–1095, 1975.

H. Kanamori and E. E. Brodsky. The physics of earthquakes. *Reports on Progress in Physics*, 67(8):1429, 2004. URL http://stacks.iop.org/0034-4885/67/i=8/a=R03.

R. Kareem, P. Cubillas, J. Gluyas, L. Bowen, S. Hillier, and H. C. Greenwell. Multi-technique approach to the petrophysical characterization of Berea Sandstone core plugs (Cleveland Quarries, USA). *Journal of Petroleum Science and Engineering*, 149:436–455, 2017.

K. M. Keranen, H. M. Savage, G. A. Abers, and E. S. Cochran. Potentially induced earthquakes in Oklahoma, USA: Links between wastewater injection and the 2011 mw 5.7 earthquake sequence. *Geology*, 41(6):699, 2013. doi:10.1130/G34045.1. URL +http://dx.doi.org/10.1130/G34045.1.

J. Kim. *Sequential methods for coupled geomechanics and multiphase flow.* PhD thesis, Stanford University, 2010.

J. Kim, H. Tchelepi, and R. Juanes. Stability and convergence of sequential methods for coupled flow and geomechanics: Fixed-stress and fixed-strain splits. *Computer Methods in Applied Mechanics and Engineering*, 200(13):1591–1606, 2011a.

J. Kim, H. Tchelepi, and R. Juanes. Stability and convergence of sequential methods for coupled flow and geomechanics: Drained and undrained splits. *Computer Methods in Applied Mechanics and Engineering*, 200(23):2094–2116, 2011b.

J. Kozeny. Über kapillare Leitung des Wassers im Boden. *Sitzungsberichte der Akademie der Wissenschaften in Wien, mathematisch-naturwissenschaftliche Klasse, Abteilung IIa*, 136: 271–306, 1927.

S. Krevor, R. Pini, L. Zuo, and S. M. Benson. Relative permeability and trapping of CO_2 and water in sandstone rocks at reservoir conditions. *Water Resources Research*, 48(2), 2012.

M. Kutz. *Handbook of Measurement in Science and Engineering.* Number Bd. 1. Wiley, 2015. ISBN 9781118446973.

R. J. Lenhard, J. C. Parker, and S. Mishra. On the correspondence between brooks-corey and van genuchten models. *Journal of Irrigation and Drainage Engineering*, 115(4):744–751, 1989. doi:10.1061/(ASCE)0733-9437(1989)115:4(744).

D. P. Lesmes and K. M. Frye. Influence of pore fluid chemistry on the complex conductivity and induced polarization responses of Berea Sandstone. *Journal of Geophysical Research: Solid Earth*, 106(B3):4079–4090, 2001.

D. A. Lockner. *Rock Failure*, pages 127–147. American Geophysical Union (AGU), 2013. ISBN 9781118668108. doi:10.1029/RF003p0127. URL https://agupubs.onlinelibrary.wiley.com/doi/abs/10.1029/RF003p0127.

G. E. Manger. *Porosity and Bulk Density of Sedimentary Rocks.* Contributions to geochemistry. U.S. Government Printing Office, 1963.

G. Mavko and A. Nur. The effect of a percolation threshold in the Kozeny-Carman relation. *Geophysics*, 62(5):1480–1482, 1997.

G. Mavko, T. Mukerji, and J. Dvorkin. *The Rock Physics Handbook: Tools for Seismic Analysis of Porous Media*. Cambridge University Press, 1998.

A. Mazzoldi, A. P. Rinaldi, A. Borgia, and J. Rutqvist. Induced seismicity within geological carbon sequestration projects: maximum earthquake magnitude and leakage potential from undetected faults. *International Journal of Greenhouse Gas Control*, 10:434–442, 2012.

A. Mikelić and M. F. Wheeler. Convergence of iterative coupling for coupled flow and geomechanics. *Computational Geosciences*, 17(3):455–461, 2013.

A. Mikelic, M. F. Wheeler, and T. Wick. A phase-field method for propagating fluid-filled fractures coupled to a surrounding porous medium. *Multiscale Modeling & Simulation*, 13 (1):367–398, 2015.

R. N. Moghaddam and M. Jamiolahmady. Gas flow transport in shale matrix: Simultaneous effects of stress and slippage on matrix permeability. In *SPE Europec featured at 78th EAGE Conference and Exhibition, 30 May-2 June, Vienna, Austria*. Society of Petroleum Engineers, 2016.

T. Myers. Potential contaminant pathways from hydraulically fractured shale to aquifers. *Groundwater*, 50(6):872–882, 2012.

J.-P. Nicot and B. R. Scanlon. Water use for shale-gas production in Texas, U.S. *Environmental Science & Technology*, 46(6):3580–3586, 2012. doi:10.1021/es204602t. PMID: 22385152.

M. van Genuchten. A Closed-form Equation for Predicting the Hydraulic Conductivity of Unsaturated Soils. *Soil Science Society of America Journal*, 44, 09 1980. doi:10.2136/sssaj1980.03615995004400050002x.

W. L. Oberkampf and T. G. Trucano. Verification and validation in computational fluid dynamics. *Progress in Aerospace Sciences*, 38(3):209 – 272, 2002. ISSN 0376-0421. doi:https://doi.org/10.1016/S0376-0421(02)00005-2. URL http://www.sciencedirect.com/science/article/pii/S0376042102000052.

P.-E. Øren and S. Bakke. Reconstruction of Berea Sandstone and pore-scale modelling of wettability effects. *Journal of Petroleum Science and Engineering*, 39(3):177–199, 2003.

S. G. Osborn, A. Vengosh, N. R. Warner, and R. B. Jackson. Methane contamination of drinking water accompanying gas-well drilling and hydraulic fracturing. *Proceedings of the National Academy of Sciences*, 108(20):8172–8176, 2011. ISSN 0027-8424. doi:10.1073/pnas.1100682108. URL http://www.pnas.org/content/108/20/8172.

T. W. Patzek, F. Male, and M. Marder. Gas production in the Barnett shale obeys a simple scaling theory. *Proceedings of the National Academy of Sciences*, 110(49):19731–19736, 2013.

G. S. Penny, T. A. Dobkins, J. T. Pursley, et al. Field Study of Completion Fluids To Enhance Gas Production in the Barnett Shale. In *SPE Gas Technology Symposium, 15-17 May, Calgary, Alberta, Canada*. Society of Petroleum Engineers, 2006.

B. p.l.c. *BP Statistical Review of World Energy*. BP p.l.c, 2018. URL https://www.bp.com/en/global/corporate/energy-economics/statistical-review-of-world-energy.html.

K. Pruess, C. Oldenburg, and G. Moridis. TOUGH2 User's Guide Version 2, 1999.

A. P. Rinaldi, J. Rutqvist, and F. Cappa. Geomechanical effects on CO_2 leakage through fault zones during large-scale underground injection. *International Journal of Greenhouse Gas Control*, 20:117–131, 2014.

J. Rouquerol, D. Avnir, C. Fairbridge, D. Everett, J. Haynes, N. Pernicone, J. Ramsay, K. Sing, and K. Unger. Recommendations for the characterization of porous solids (Technical Report). *Pure and Applied Chemistry*, 66(8):1739–1758, 1994.

J. Rutqvist and C.-F. Tsang. A study of caprock hydromechanical changes associated with CO_2-injection into a brine formation. *Environmental Geology*, 42(2-3):296–305, 2002.

J. Rutqvist, Y.-S. Wu, C.-F. Tsang, and G. Bodvarsson. A modeling approach for analysis of coupled multiphase fluid flow, heat transfer, and deformation in fractured porous rock. *International Journal of Rock Mechanics and Mining Sciences*, 39(4):429–442, 2002.

J. Rutqvist, J. Birkholzer, and C.-F. Tsang. Coupled reservoir–geomechanical analysis of the potential for tensile and shear failure associated with CO_2 injection in multilayered reservoir–caprock systems. *International Journal of Rock Mechanics and Mining Sciences*, 45(2):132 – 143, 2008. ISSN 1365-1609. doi:https://doi.org/10.1016/j.ijrmms.2007.04.006. URL http://www.sciencedirect.com/science/article/pii/S1365160907000548.

J. Rutqvist, A. P. Rinaldi, F. Cappa, and G. J. Moridis. Modeling of fault reactivation and induced seismicity during hydraulic fracturing of shale-gas reservoirs. *Journal of Petroleum Science and Engineering*, 107:31–44, 2013.

J. Segura and I. Carol. Coupled hm analysis using zero-thickness interface elements with double nodes. part i: Theoretical model. *International Journal for Numerical and Analytical Methods in Geomechanics*, 32(18):2083–2101, 2008.

A. Settari, D. A. Walters, et al. Advances in coupled geomechanical and reservoir modeling with applications to reservoir compaction. *Spe Journal*, 6(03):334–342, 2001.

B. Skinner and S. Porter. *The Dynamic Earth: An Introduction to Physical Geology*. Wiley, 2000. ISBN 9780471161189.

R. J. Skoumal, M. R. Brudzinski, and B. S. Currie. Earthquakes induced by hydraulic fracturing in poland township, ohioearthquakes induced by hydraulic fracturing in poland township, ohio. *Bulletin of the Seismological Society of America*, 105(1):189, 2015. doi:10.1785/0120140168. URL http://dx.doi.org/10.1785/0120140168.

I. S. Sokolnikoff. *Mathematical theory of elasticity*. McGraw-Hill book company, 1956.

K. Stüben. *Algebraic Multigrid (AMG): An Introduction with Applications*. GMD-Report. GMD-Forschungszentrum Informationstechnik, 1999.

W. Thatcher and T. C. Hanks. Source parameters of southern california earthquakes. *Journal of geophysical research*, 78(35):8547–8576, 1973.

A. N. Tutuncu et al. Anisotropy, compaction and dispersion characteristics of reservoir and seal shales. In *44th US Rock Mechanics Symposium and 5th US-Canada Rock Mechanics Symposium*. American Rock Mechanics Association, 2010.

E. Ucar, I. Berre, and E. Keilegavlen. Three-dimensional numerical modeling of shear stimulation of naturally fractured rock formations. *arXiv preprint arXiv:1709.01847*, 2017.

J. P. Verdon, J.-M. Kendall, A. L. Stork, R. A. Chadwick, D. J. White, and R. C. Bissell. Comparison of geomechanical deformation induced by megatonne-scale CO_2 storage at sleipner, weyburn, and in salah. *Proceedings of the National Academy of Sciences*, 110(30): E2762–E2771, 2013. ISSN 0027-8424. doi:10.1073/pnas.1302156110. URL http://www.pnas.org/content/110/30/E2762.

V. Vilarrasa and J. Carrera. Geologic carbon storage is unlikely to trigger large earthquakes and reactivate faults through which CO_2 could leak. *Proceedings of the National Academy of Sciences*, 2015. ISSN 0027-8424. doi:10.1073/pnas.1413284112. URL http://www.pnas.org/content/early/2015/04/14/1413284112.

L. Walter, P. J. Binning, S. Oladyshkin, B. Flemisch, and H. Class. Brine migration resulting from CO_2 injection into saline aquifers – an approach to risk estimation including various levels of uncertainty. *International Journal of Greenhouse Gas Control*, 9:495 – 506, 2012. ISSN 1750-5836. doi:https://doi.org/10.1016/j.ijggc.2012.05.004.

Q. Wang, X. Chen, A. N. Jha, and H. Rogers. Natural gas from shale formation – the evolution, evidences and challenges of shale gas revolution in united states. *Renewable and Sustainable Energy Reviews*, 30:1 – 28, 2014. ISSN 1364-0321.

doi:https://doi.org/10.1016/j.rser.2013.08.065. URL http://www.sciencedirect.com/science/article/pii/S1364032113006059.

J. A. White and R. I. Borja. Block-preconditioned Newton-Krylov solvers for fully coupled flow and geomechanics. *Computational Geosciences*, 15(4):647, 2011.

J. A. White, N. Castelletto, and H. A. Tchelepi. Block-partitioned solvers for coupled poromechanics: A unified framework. *Computer Methods in Applied Mechanics and Engineering*, 303:55–74, 2016.

L. Williams, P. Macnaghten, R. Davies, and S. Curtis. Framing 'fracking': Exploring public perceptions of hydraulic fracturing in the united kingdom. *Public Understanding of Science*, 26(1):89–104, 2017. doi:10.1177/0963662515595159. URL https://doi.org/10.1177/0963662515595159.

Q. Zhou, J. T. Birkholzer, C.-F. Tsang, and J. Rutqvist. A method for quick assessment of CO_2 storage capacity in closed and semi-closed saline formations. *International Journal of Greenhouse Gas Control*, 2(4):626–639, 2008.

R. W. Zimmerman. *Compressibility of sandstones*, volume 29. Elsevier, 1991.

M. D. Zoback. *Reservoir Geomechanics*. Cambridge University Press, 2007. doi:10.1017/CBO9780511586477.

M. D. Zoback and S. M. Gorelick. Earthquake triggering and large-scale geologic storage of carbon dioxide. *Proceedings of the National Academy of Sciences*, 2012. ISSN 0027-8424. doi:10.1073/pnas.1202473109. URL http://www.pnas.org/content/early/2012/06/13/1202473109.

M. D. Zoback and S. M. Gorelick. To prevent earthquake triggering, pressure changes due to CO_2 injection need to be limited. *Proceedings of the National Academy of Sciences*, 112(33):E4510–E4510, 2015. ISSN 0027-8424. doi:10.1073/pnas.1508533112. URL http://www.pnas.org/content/112/33/E4510.

A Derivation of the effective porosity

The components of the porous medium exhibit different responses to stress and pressure changes. To describe this, the different bulk moduli were introduced. This has also consequences for the porosity ϕ. Its change is defined as:

$$\mathrm{d}\phi = \mathrm{d}\left(\frac{V_\mathrm{p}}{V_\mathrm{b}}\right) \tag{A.1}$$

The quotient rule gives:

$$= \frac{\mathrm{d}V_\mathrm{p} V_\mathrm{b} - V_\mathrm{p}\mathrm{d}V_\mathrm{b}}{V_\mathrm{b}^2} \tag{A.2}$$

$$= \frac{\mathrm{d}V_\mathrm{p} V_\mathrm{b}}{V_\mathrm{b}^2} - \frac{V_\mathrm{p}\mathrm{d}V_\mathrm{b}}{V_\mathrm{b}^2} \tag{A.3}$$

$$= \frac{\mathrm{d}V_\mathrm{p}}{V_\mathrm{b}} - \phi\frac{\mathrm{d}V_\mathrm{b}}{V_\mathrm{b}} \tag{A.4}$$

with the pore volume V_p and the bulk volume V_b. With Equation 2.47 and 2.40, the change in bulk volume V_p can be described as a function of volumetric stress σ_v and pore pressure p

$$\frac{\mathrm{d}V_\mathrm{b}}{V_\mathrm{b}} = -\frac{1}{K_\mathrm{dr}}\left(\mathrm{d}\sigma_\mathrm{v} - \alpha\,\mathrm{d}p\right) \tag{A.5}$$

By introducing an effective stress coefficient

$$\beta = 1 - \frac{K_\mathrm{p}}{K_\mathrm{s}} \tag{A.6}$$

for the pore volume V_p (equivalent to the Biot coefficient α for the bulk volume V_b), the change in the pore volume V_p can be expressed as

$$\frac{\mathrm{d}V_\mathrm{p}}{V_\mathrm{p}} = -\frac{1}{K_\mathrm{p}}\left(\mathrm{d}\sigma_\mathrm{v} - \beta\,\mathrm{d}p\right) \tag{A.7}$$

as described in Detouray and Cheng (1993). By using Equation A.5 and A.7 and by exploiting $V_\mathrm{p} = \phi\, V_\mathrm{b}$, $\mathrm{d}\phi$ becomes

$$\begin{aligned} \mathrm{d}\phi = \quad & -\frac{1}{K_\mathrm{p}}\,\phi\,\mathrm{d}\sigma_\mathrm{v} + \frac{\beta}{K_\mathrm{p}}\,\phi\,\mathrm{d}p \\ & +\frac{1}{K_\mathrm{dr}}\,\phi\,\mathrm{d}\sigma_\mathrm{v} - \frac{\alpha}{K_\mathrm{dr}}\,\phi\,\mathrm{d}p \end{aligned} \tag{A.8}$$

or

$$\begin{aligned} \mathrm{d}\phi = \quad & -\frac{1}{K_\mathrm{p}}\,\phi\,\mathrm{d}\sigma_\mathrm{v} + \frac{1-\frac{K_\mathrm{p}}{K_\mathrm{s}}}{K_\mathrm{p}}\,\phi\,\mathrm{d}p \\ & +\frac{1}{K_\mathrm{dr}}\,\phi\,\mathrm{d}\sigma_\mathrm{v} - \frac{1-\frac{K_\mathrm{dr}}{K_\mathrm{s}}}{K_\mathrm{dr}}\,\phi\,\mathrm{d}p \end{aligned}$$

which can be transformed into

$$\begin{aligned} \mathrm{d}\phi = \quad & -\frac{1}{K_\mathrm{p}}\,\phi\,\mathrm{d}\sigma_\mathrm{v} + \left(\frac{1}{K_\mathrm{p}} - \frac{1}{K_\mathrm{S}}\right)\phi\,\mathrm{d}p \\ & +\frac{1}{K_\mathrm{dr}}\,\phi\,\mathrm{d}\sigma_\mathrm{v} - \left(\frac{1}{K_\mathrm{dr}} - \frac{1}{K_\mathrm{S}}\right)\phi\,\mathrm{d}p \\ = \quad & -\frac{1}{K_\mathrm{p}}\,\phi\,\mathrm{d}\sigma_\mathrm{v} + \frac{1}{K_\mathrm{p}}\phi\,\mathrm{d}p \qquad \text{(A.9)} \\ & +\frac{1}{K_\mathrm{dr}}\,\phi\,\mathrm{d}\sigma_\mathrm{v} - \frac{1}{K_\mathrm{dr}}\phi\,\mathrm{d}p \qquad \text{(A.10)} \end{aligned}$$

which simplifies to

$$\mathrm{d}\phi = \left(-\frac{\phi}{K_\mathrm{dr}} + \frac{\phi}{K_\mathrm{p}}\right)(-\mathrm{d}\sigma_\mathrm{v} + \mathrm{d}p)\,. \tag{A.11}$$

Using $K_\mathrm{p} = \frac{\phi}{\alpha} K_\mathrm{dr}$ (Detouray and Cheng, 1993), one obtains

$$\mathrm{d}\phi = \left(-\frac{\phi}{K_\mathrm{dr}} + \frac{\alpha}{K_\mathrm{dr}}\right)(-\mathrm{d}\sigma_\mathrm{v} + \mathrm{d}p)\,. \tag{A.12}$$

Finally, with $\frac{1}{K_\mathrm{s}} = \frac{1-\alpha}{K_\mathrm{dr}}$, the change in porosity can be expressed as

$$\begin{aligned} \mathrm{d}\phi &= \left(\frac{1}{K_\mathrm{dr}} - \frac{\phi}{K_\mathrm{dr}} - \frac{1}{K_\mathrm{dr}} + \frac{\alpha}{K_\mathrm{dr}}\right)(-\mathrm{d}\sigma_\mathrm{v} + \mathrm{d}p)\,. \qquad \text{(A.13)} \\ &= \left(\frac{1}{K_\mathrm{dr}}(1-\phi) - \frac{1}{K_\mathrm{s}}\right)(-\mathrm{d}\sigma_\mathrm{v} + \mathrm{d}p)\,. \end{aligned}$$

This is in agreement with the relationship published in Han and Dusseault (2003), which was derived from the different compressibilities defined in Zimmerman (1991) instead of the different bulk moduli. Han and Dusseault (2003) further replace the stress the with volumetric strain defined by

$$\mathrm{d}\epsilon_\mathrm{v} = \frac{1}{K_\mathrm{dr}}\,(\sigma_\mathrm{v} - \alpha \mathrm{d}p) \tag{A.14}$$

so σ_v can be expressed as

$$\begin{aligned} \mathrm{d}\sigma_\mathrm{v} &= K_\mathrm{dr}\epsilon_\mathrm{v} + \alpha \mathrm{d}p \qquad (A.15) \\ &= K_\mathrm{dr}\epsilon_\mathrm{v} + \left(1 - \frac{K_\mathrm{dr}}{K_\mathrm{S}}\right)\mathrm{d}p, \qquad (A.16) \end{aligned}$$

so Equation A.13 becomes

$$\mathrm{d}\phi = \left(1 - \frac{K_\mathrm{dr}}{K_\mathrm{s}} - \phi\right)\left(-\mathrm{d}\epsilon_\mathrm{v} + \frac{1}{K_\mathrm{s}}\mathrm{d}p\right). \qquad (A.17)$$

For the assumption of very rigid grains ($K_\mathrm{s} \to \infty$), this reduces to

$$\mathrm{d}\phi = -\left(1 - \phi\right)\mathrm{d}\epsilon_\mathrm{v}. \qquad (A.18)$$

This allows to calculate an *effective porosity* ϕ_eff from the volumetric strain ϵ_v and the initial porosity ϕ_0 (assuming $\epsilon_{\mathrm{v},0} = 0$):

$$\phi_\mathrm{eff} = \frac{\phi_0 - \epsilon_\mathrm{v}}{1 - \epsilon_\mathrm{v}} \qquad (A.19)$$

B Software

module	version/branch	website	comment
dune-common	releases/2.4	https://gitlab.dune-project.org/core/dune-common.git	Blatt et al. (2016)
dune-geometry	releases/2.4	https://gitlab.dune-project.org/core/dune-geometry.git	
dune-grid	releases/2.4	https://gitlab.dune-project.org/core/dune-grid.git	Bastian et al. (2008b,a)
dune-istl	releases/2.4	https://gitlab.dune-project.org/core/dune-istl.git	Blatt and Bastian (2007)
dune-localfunction	releases/2.4	https://gitlab.dune-project.org/core/dune-localfunctions.git	
dune-pdflab	releases/2.0	https://gitlab.dune-project.org/pdelab/dune-pdelab.git	
dune-typetree	releases/2.3	https://gitlab.dune-project.org/pdelab/dune-typetree.git	
dune-alugrid	releases/2.4	https://gitlab.dune-project.org/extensions/dune-alugrid.git	Alkämper et al. (2016)
beck2019a	master	https://git.iws.uni-stuttgart.de/dumux-pub/beck2019a.git	Fully-coupled and fixed-stress implementation
beck2019b	master	https://git.iws.uni-stuttgart.de/dumux-pub/beck2019b.git	Fault reactivation

Institut für Wasser- und Umweltsystemmodellierung
Universität Stuttgart

Pfaffenwaldring 61
70569 Stuttgart (Vaihingen)
Telefon (0711) 685 - 64717/64749/64752/64679
Telefax (0711) 685 - 67020 o. 64746 o. 64681
E-Mail: iws@iws.uni-stuttgart.de
http://www.iws.uni-stuttgart.de

Verzeichnis der Mitteilungshefte

1 Röhnisch, Arthur: *Die Bemühungen um eine Wasserbauliche Versuchsanstalt an der Technischen Hochschule Stuttgart*, und
Fattah Abouleid, Abdel: *Beitrag zur Berechnung einer in lockeren Sand gerammten, zweifach verankerten Spundwand*, 1963

2 Marotz, Günter: *Beitrag zur Frage der Standfestigkeit von dichten Asphaltbelägen im Großwasserbau*, 1964

3 Gurr, Siegfried: *Beitrag zur Berechnung zusammengesetzter ebener Flächentrag-werke unter besonderer Berücksichtigung ebener Stauwände, mit Hilfe von Rand-wert- und Lastwertmatrizen*, 1965

4 Plica, Peter: *Ein Beitrag zur Anwendung von Schalenkonstruktionen im Stahlwasserbau*, und
Petrikat, Kurt: *Möglichkeiten und Grenzen des wasserbaulichen Versuchswesens*, 1966

5 Plate, Erich: *Beitrag zur Bestimmung der Windgeschwindigkeitsverteilung in der durch eine Wand gestörten bodennahen Luftschicht*, und
Röhnisch, Arthur; Marotz, Günter: *Neue Baustoffe und Bauausführungen für den Schutz der Böschungen und der Sohle von Kanälen, Flüssen und Häfen; Gestehungskosten und jeweilige Vorteile*, sowie
Unny, T.E.: *Schwingungsuntersuchungen am Kegelstrahlschieber*, 1967

6 Seiler, Erich: *Die Ermittlung des Anlagenwertes der bundeseigenen Binnenschiffahrtsstraßen und Talsperren und des Anteils der Binnenschiffahrt an diesem Wert*, 1967

7 *Sonderheft anläßlich des 65. Geburtstages von Prof. Arthur Röhnisch mit Beiträgen von* Benk, Dieter; Breitling, J.; Gurr, Siegfried; Haberhauer, Robert; Honekamp, Hermann; Kuz, Klaus Dieter; Marotz, Günter; Mayer-Vorfelder, Hans-Jörg; Miller, Rudolf; Plate, Erich J.; Radomski, Helge; Schwarz, Helmut; Vollmer, Ernst; Wildenhahn, Eberhard; 1967

8 Jumikis, Alfred: *Beitrag zur experimentellen Untersuchung des Wassernachschubs in einem gefrierenden Boden und die Beurteilung der Ergebnisse*, 1968

9 Marotz, Günter: *Technische Grundlagen einer Wasserspeicherung im natürlichen Untergrund*, 1968

10 Radomski, Helge: *Untersuchungen über den Einfluß der Querschnittsform wellenförmiger Spundwände auf die statischen und rammtechnischen Eigenschaften*, 1968

11 Schwarz, Helmut: *Die Grenztragfähigkeit des Baugrundes bei Einwirkung vertikal gezogener Ankerplatten als zweidimensionales Bruchproblem*, 1969

12 Erbel, Klaus: *Ein Beitrag zur Untersuchung der Metamorphose von Mittelgebirgsschneedecken unter besonderer Berücksichtigung eines Verfahrens zur Bestimmung der thermischen Schneequalität*, 1969

13 Westhaus, Karl-Heinz: *Der Strukturwandel in der Binnenschiffahrt und sein Einfluß auf den Ausbau der Binnenschiffskanäle*, 1969

14 Mayer-Vorfelder, Hans-Jörg: *Ein Beitrag zur Berechnung des Erdwiderstandes unter Ansatz der logarithmischen Spirale als Gleitflächenfunktion*, 1970

15 Schulz, Manfred: *Berechnung des räumlichen Erddruckes auf die Wandung kreiszylindrischer Körper*, 1970

16 Mobasseri, Manoutschehr: *Die Rippenstützmauer. Konstruktion und Grenzen ihrer Standsicherheit*, 1970

17 Benk, Dieter: *Ein Beitrag zum Betrieb und zur Bemessung von Hochwasserrückhaltebecken*, 1970

18 Gàl, Attila: *Bestimmung der mitschwingenden Wassermasse bei überströmten Fischbauchklappen mit kreiszylindrischem Staublech*, 1971, vergriffen

19 Kuz, Klaus Dieter: *Ein Beitrag zur Frage des Einsetzens von Kavitationserscheinungen in einer Düsenströmung bei Berücksichtigung der im Wasser gelösten Gase*, 1971, vergriffen

20 Schaak, Hartmut: *Verteilleitungen von Wasserkraftanlagen*, 1971

21 *Sonderheft zur Eröffnung der neuen Versuchsanstalt des Instituts für Wasserbau der Universität Stuttgart mit Beiträgen von* Brombach, Hansjörg; Dirksen, Wolfram; Gàl, Attila; Gerlach, Reinhard; Giesecke, Jürgen; Holthoff, Franz-Josef; Kuz, Klaus Dieter; Marotz, Günter; Minor, Hans-Erwin; Petrikat, Kurt; Röhnisch, Arthur; Rueff, Helge; Schwarz, Helmut; Vollmer, Ernst; Wildenhahn, Eberhard; 1972

22 Wang, Chung-su: *Ein Beitrag zur Berechnung der Schwingungen an Kegelstrahlschiebern*, 1972

23 Mayer-Vorfelder, Hans-Jörg: *Erdwiderstandsbeiwerte nach dem Ohde-Variationsverfahren*, 1972

24 Minor, Hans-Erwin: *Beitrag zur Bestimmung der Schwingungsanfachungsfunktionen überströmter Stauklappen*, 1972, vergriffen

25 Brombach, Hansjörg: *Untersuchung strömungsmechanischer Elemente (Fluidik) und die Möglichkeit der Anwendung von Wirbelkammerelementen im Wasserbau*, 1972, vergriffen

26 Wildenhahn, Eberhard: *Beitrag zur Berechnung von Horizontalfilterbrunnen*, 1972

27 Steinlein, Helmut: *Die Eliminierung der Schwebstoffe aus Flußwasser zum Zweck der unterirdischen Wasserspeicherung, gezeigt am Beispiel der Iller*, 1972

28 Holthoff, Franz Josef: *Die Überwindung großer Hubhöhen in der Binnenschiffahrt durch Schwimmerhebewerke*, 1973

29 Röder, Karl: *Einwirkungen aus Baugrundbewegungen auf trog- und kastenförmige Konstruktionen des Wasser- und Tunnelbaues*, 1973

30 Kretschmer, Heinz: *Die Bemessung von Bogenstaumauern in Abhängigkeit von der Talform*, 1973

31 Honekamp, Hermann: *Beitrag zur Berechnung der Montage von Unterwasserpipelines*, 1973

32 Giesecke, Jürgen: *Die Wirbelkammertriode als neuartiges Steuerorgan im Wasserbau*, und Brombach, Hansjörg: *Entwicklung, Bauformen, Wirkungsweise und Steuereigenschaften von Wirbelkammerverstärkern*, 1974

33 Rueff, Helge: *Untersuchung der schwingungserregenden Kräfte an zwei hintereinander angeordneten Tiefschützen unter besonderer Berücksichtigung von Kavitation*, 1974

34 Röhnisch, Arthur: *Einpreßversuche mit Zementmörtel für Spannbeton - Vergleich der Ergebnisse von Modellversuchen mit Ausführungen in Hüllwellrohren*, 1975

35 *Sonderheft anläßlich des 65. Geburtstages von Prof. Dr.-Ing. Kurt Petrikat mit Beiträgen von*: Brombach, Hansjörg; Erbel, Klaus; Flinspach, Dieter; Fischer jr., Richard; Gàl, Attila; Gerlach, Reinhard; Giesecke, Jürgen; Haberhauer, Robert; Hafner Edzard; Hausenblas, Bernhard; Horlacher, Hans-Burkhard; Hutarew, Andreas; Knoll, Manfred; Krummet, Ralph; Marotz, Günter; Merkle, Theodor; Miller, Christoph; Minor, Hans-Erwin; Neumayer, Hans; Rao, Syamala; Rath, Paul; Rueff, Helge; Ruppert, Jürgen; Schwarz, Wolfgang; Topal-Gökceli, Mehmet; Vollmer, Ernst; Wang, Chung-su; Weber, Hans-Georg; 1975

36 Berger, Jochum: *Beitrag zur Berechnung des Spannungszustandes in rotationssymmetrisch belasteten Kugelschalen veränderlicher Wandstärke unter Gas- und Flüssigkeitsdruck durch Integration schwach singulärer Differentialgleichungen*, 1975

37 Dirksen, Wolfram: *Berechnung instationärer Abflußvorgänge in gestauten Gerinnen mittels Differenzenverfahren und die Anwendung auf Hochwasserrückhaltebecken*, 1976

38 Horlacher, Hans-Burkhard: *Berechnung instationärer Temperatur- und Wärmespannungsfelder in langen mehrschichtigen Hohlzylindern*, 1976

39 Hafner, Edzard: *Untersuchung der hydrodynamischen Kräfte auf Baukörper im Tiefwasserbereich des Meeres*, 1977, ISBN 3-921694-39-6

40 Ruppert, Jürgen: *Über den Axialwirbelkammerverstärker für den Einsatz im Wasserbau*, 1977, ISBN 3-921694-40-X

41 Hutarew, Andreas: *Beitrag zur Beeinflußbarkeit des Sauerstoffgehalts in Fließgewässern an Abstürzen und Wehren*, 1977, ISBN 3-921694-41-8, *vergriffen*

42 Miller, Christoph: *Ein Beitrag zur Bestimmung der schwingungserregenden Kräfte an unterströmten Wehren*, 1977, ISBN 3-921694-42-6

43 Schwarz, Wolfgang: *Druckstoßberechnung unter Berücksichtigung der Radial- und Längsverschiebungen der Rohrwandung*, 1978, ISBN 3-921694-43-4

44 Kinzelbach, Wolfgang: *Numerische Untersuchungen über den optimalen Einsatz variabler Kühlsysteme einer Kraftwerkskette am Beispiel Oberrhein*, 1978, ISBN 3-921694-44-2

45 Barczewski, Baldur: *Neue Meßmethoden für Wasser-Luftgemische und deren Anwendung auf zweiphasige Auftriebsstrahlen*, 1979, ISBN 3-921694-45-0

46 Neumayer, Hans: *Untersuchung der Strömungsvorgänge in radialen Wirbelkammerverstärkern*, 1979, ISBN 3-921694-46-9

47 Elalfy, Youssef-Elhassan: *Untersuchung der Strömungsvorgänge in Wirbelkammerdioden und -drosseln*, 1979, ISBN 3-921694-47-7

48 Brombach, Hansjörg: *Automatisierung der Bewirtschaftung von Wasserspeichern*, 1981, ISBN 3-921694-48-5

49 Geldner, Peter: *Deterministische und stochastische Methoden zur Bestimmung der Selbstdichtung von Gewässern*, 1981, ISBN 3-921694-49-3, *vergriffen*

50 Mehlhorn, Hans: *Temperaturveränderungen im Grundwasser durch Brauchwassereinleitungen*, 1982, ISBN 3-921694-50-7, *vergriffen*

51 Hafner, Edzard: *Rohrleitungen und Behälter im Meer*, 1983, ISBN 3-921694-51-5

52 Rinnert, Bernd: *Hydrodynamische Dispersion in porösen Medien: Einfluß von Dichteunterschieden auf die Vertikalvermischung in horizontaler Strömung*, 1983, ISBN 3-921694-52-3, *vergriffen*

53 Lindner, Wulf: *Steuerung von Grundwasserentnahmen unter Einhaltung ökologischer Kriterien*, 1983, ISBN 3-921694-53-1, *vergriffen*

54 Herr, Michael; Herzer, Jörg; Kinzelbach, Wolfgang; Kobus, Helmut; Rinnert, Bernd: *Methoden zur rechnerischen Erfassung und hydraulischen Sanierung von Grundwasserkontaminationen*, 1983, ISBN 3-921694-54-X

55 Schmitt, Paul: *Wege zur Automatisierung der Niederschlagsermittlung*, 1984, ISBN 3-921694-55-8, *vergriffen*

56 Müller, Peter: *Transport und selektive Sedimentation von Schwebstoffen bei gestautem Abfluß*, 1985, ISBN 3-921694-56-6

57 El-Qawasmeh, Fuad: *Möglichkeiten und Grenzen der Tropfbewässerung unter besonderer Berücksichtigung der Verstopfungsanfälligkeit der Tropfelemente*, 1985, ISBN 3-921694-57-4, *vergriffen*

58 Kirchenbaur, Klaus: *Mikroprozessorgesteuerte Erfassung instationärer Druckfelder am Beispiel seegangsbelasteter Baukörper*, 1985, ISBN 3-921694-58-2

59 Kobus, Helmut (Hrsg.): *Modellierung des großräumigen Wärme- und Schadstofftransports im Grundwasser*, Tätigkeitsbericht 1984/85 (DFG-Forschergruppe an den Universitäten Hohenheim, Karlsruhe und Stuttgart), 1985, ISBN 3-921694-59-0, *vergriffen*

60 Spitz, Karlheinz: *Dispersion in porösen Medien: Einfluß von Inhomogenitäten und Dichteunterschieden*, 1985, ISBN 3-921694-60-4, *vergriffen*

61 Kobus, Helmut: *An Introduction to Air-Water Flows in Hydraulics*, 1985, ISBN 3-921694-61-2

62 Kaleris, Vassilios: *Erfassung des Austausches von Oberflächen- und Grundwasser in horizontalebenen Grundwassermodellen*, 1986, ISBN 3-921694-62-0

63 Herr, Michael: *Grundlagen der hydraulischen Sanierung verunreinigter Porengrundwasserleiter*, 1987, ISBN 3-921694-63-9

64 Marx, Walter: *Berechnung von Temperatur und Spannung in Massenbeton infolge Hydratation*, 1987, ISBN 3-921694-64-7

65 Koschitzky, Hans-Peter: *Dimensionierungskonzept für Sohlbelüfter in Schußrinnen zur Vermeidung von Kavitationsschäden*, 1987, ISBN 3-921694-65-5

66 Kobus, Helmut (Hrsg.): *Modellierung des großräumigen Wärme- und Schadstofftransports im Grundwasser*, Tätigkeitsbericht 1986/87 (DFG-Forschergruppe an den Universitäten Hohenheim, Karlsruhe und Stuttgart) 1987, ISBN 3-921694-66-3

67 Söll, Thomas: *Berechnungsverfahren zur Abschätzung anthropogener Temperaturanomalien im Grundwasser*, 1988, ISBN 3-921694-67-1

68 Dittrich, Andreas; Westrich, Bernd: *Bodenseeufererosion, Bestandsaufnahme und Bewertung*, 1988, ISBN 3-921694-68-X, *vergriffen*

69 Huwe, Bernd; van der Ploeg, Rienk R.: *Modelle zur Simulation des Stickstoffhaushaltes von Standorten mit unterschiedlicher landwirtschaftlicher Nutzung*, 1988, ISBN 3-921694-69-8, *vergriffen*

70 Stephan, Karl: *Integration elliptischer Funktionen*, 1988, ISBN 3-921694-70-1

71 Kobus, Helmut; Zilliox, Lothaire (Hrsg.): *Nitratbelastung des Grundwassers, Auswirkungen der Landwirtschaft auf die Grundwasser- und Rohwasserbeschaffenheit und Maßnahmen zum Schutz des Grundwassers*. Vorträge des deutsch-französischen Kolloquiums am 6. Oktober 1988, Universitäten Stuttgart und Louis Pasteur Strasbourg (Vorträge in deutsch oder französisch, Kurzfassungen zweisprachig), 1988, ISBN 3-921694-71-X

72 Soyeaux, Renald: *Unterströmung von Stauanlagen auf klüftigem Untergrund unter Berücksichtigung laminarer und turbulenter Fließzustände*,1991, ISBN 3-921694-72-8

73 Kohane, Roberto: *Berechnungsmethoden für Hochwasserabfluß in Fließgewässern mit überströmten Vorländern*, 1991, ISBN 3-921694-73-6

74 Hassinger, Reinhard: *Beitrag zur Hydraulik und Bemessung von Blocksteinrampen in flexibler Bauweise*, 1991, ISBN 3-921694-74-4, vergriffen

75 Schäfer, Gerhard: *Einfluß von Schichtenstrukturen und lokalen Einlagerungen auf die Längsdispersion in Porengrundwasserleitern*, 1991, ISBN 3-921694-75-2

76 Giesecke, Jürgen: *Vorträge, Wasserwirtschaft in stark besiedelten Regionen; Umweltforschung mit Schwerpunkt Wasserwirtschaft*, 1991, ISBN 3-921694-76-0

77 Huwe, Bernd: *Deterministische und stochastische Ansätze zur Modellierung des Stickstoffhaushalts landwirtschaftlich genutzter Flächen auf unterschiedlichem Skalenniveau*, 1992, ISBN 3-921694-77-9, vergriffen

78 Rommel, Michael: *Verwendung von Kluftdaten zur realitätsnahen Generierung von Kluftnetzen mit anschließender laminar-turbulenter Strömungsberechnung*, 1993, ISBN 3-92 1694-78-7

79 Marschall, Paul: *Die Ermittlung lokaler Stofffrachten im Grundwasser mit Hilfe von Einbohrloch-Meßverfahren*, 1993, ISBN 3-921694-79-5, vergriffen

80 Ptak, Thomas: *Stofftransport in heterogenen Porenaquiferen: Felduntersuchungen und stochastische Modellierung*, 1993, ISBN 3-921694-80-9, vergriffen

81 Haakh, Frieder: *Transientes Strömungsverhalten in Wirbelkammern,* 1993, ISBN 3-921694-81-7

82 Kobus, Helmut; Cirpka, Olaf; Barczewski, Baldur; Koschitzky, Hans-Peter: *Versuchseinrichtung zur Grundwasser- und Altlastensanierung VEGAS, Konzeption und Programmrahmen*, 1993, ISBN 3-921694-82-5

83 Zang, Weidong: *Optimaler Echtzeit-Betrieb eines Speichers mit aktueller Abflußregenerierung*, 1994, ISBN 3-921694-83-3, vergriffen

84 Franke, Hans-Jörg: *Stochastische Modellierung eines flächenhaften Stoffeintrages und Transports in Grundwasser am Beispiel der Pflanzenschutzmittelproblematik*, 1995, ISBN 3-921694-84-1

85 Lang, Ulrich: *Simulation regionaler Strömungs- und Transportvorgänge in Karstaquiferen mit Hilfe des Doppelkontinuum-Ansatzes: Methodenentwicklung und Parameteridentifikation*, 1995, ISBN 3-921694-85-X, vergriffen

86 Helmig, Rainer: *Einführung in die Numerischen Methoden der Hydromechanik*, 1996, ISBN 3-921694-86-8, vergriffen

87 Cirpka, Olaf: *CONTRACT: A Numerical Tool for Contaminant Transport and Chemical Transformations - Theory and Program Documentation -*, 1996, ISBN 3-921694-87-6

88 Haberlandt, Uwe: *Stochastische Synthese und Regionalisierung des Niederschlages für Schmutzfrachtberechnungen*, 1996, ISBN 3-921694-88-4

89 Croisé, Jean: *Extraktion von flüchtigen Chemikalien aus natürlichen Lockergesteinen mittels erzwungener Luftströmung*, 1996, ISBN 3-921694-89-2, vergriffen

90 Jorde, Klaus: *Ökologisch begründete, dynamische Mindestwasserregelungen bei Ausleitungskraftwerken*, 1997, ISBN 3-921694-90-6, vergriffen

91 Helmig, Rainer: *Gekoppelte Strömungs- und Transportprozesse im Untergrund - Ein Beitrag zur Hydrosystemmodellierung-*, 1998, ISBN 3-921694-91-4, vergriffen

92 Emmert, Martin: *Numerische Modellierung nichtisothermer Gas-Wasser Systeme in porösen Medien,* 1997, ISBN 3-921694-92-2

93 Kern, Ulrich: *Transport von Schweb- und Schadstoffen in staugeregelten Fließgewässern am Beispiel des Neckars*, 1997, ISBN 3-921694-93-0, vergriffen

94 Förster, Georg: *Druckstoßdämpfung durch große Luftblasen in Hochpunkten von Rohrleitungen 1997*, ISBN 3-921694-94-9

95 Cirpka, Olaf: *Numerische Methoden zur Simulation des reaktiven Mehrkomponententransports im Grundwasser*, 1997, ISBN 3-921694-95-7, *vergriffen*

96 Färber, Arne: *Wärmetransport in der ungesättigten Bodenzone: Entwicklung einer thermischen In-situ-Sanierungstechnologie*, 1997, ISBN 3-921694-96-5

97 Betz, Christoph: *Wasserdampfdestillation von Schadstoffen im porösen Medium: Entwicklung einer thermischen In-situ-Sanierungstechnologie*, 1998, SBN 3-921694-97-3

98 Xu, Yichun: *Numerical Modeling of Suspended Sediment Transport in Rivers*, 1998, ISBN 3-921694-98-1, *vergriffen*

99 Wüst, Wolfgang: *Geochemische Untersuchungen zur Sanierung CKW-kontaminierter Aquifere mit Fe(0)-Reaktionswänden,* 2000, ISBN 3-933761-02-2

100 Sheta, Hussam: *Simulation von Mehrphasenvorgängen in porösen Medien unter Einbeziehung von Hysterese-Effekten*, 2000, ISBN 3-933761-03-4

101 Ayros, Edwin: *Regionalisierung extremer Abflüsse auf der Grundlage statistischer Verfahren*, 2000, ISBN 3-933761-04-2, *vergriffen*

102 Huber, Ralf: *Compositional Multiphase Flow and Transport in Heterogeneous Porous Media*, 2000, ISBN 3-933761-05-0

103 Braun, Christopherus: *Ein Upscaling-Verfahren für Mehrphasenströmungen in porösen Medien*, 2000, ISBN 3-933761-06-9

104 Hofmann, Bernd: *Entwicklung eines rechnergestützten Managementsystems zur Beurteilung von Grundwasserschadensfällen*, 2000, ISBN 3-933761-07-7

105 Class, Holger: *Theorie und numerische Modellierung nichtisothermer Mehrphasenprozesse in NAPL-kontaminierten porösen Medien,* 2001, ISBN 3-933761-08-5

106 Schmidt, Reinhard: *Wasserdampf- und Heißluftinjektion zur thermischen Sanierung kontaminierter Standorte*, 2001, ISBN 3-933761-09-3

107 Josef, Reinhold: *Schadstoffextraktion mit hydraulischen Sanierungsverfahren unter Anwendung von grenzflächenaktiven Stoffen*, 2001, ISBN 3-933761-10-7

108 Schneider, Matthias: *Habitat- und Abflussmodellierung für Fließgewässer mit unscharfen Berechnungsansätzen*, 2001, ISBN 3-933761-11-5

109 Rathgeb, Andreas: *Hydrodynamische Bemessungsgrundlagen für Lockerdeckwerke an überströmbaren Erddämmen*, 2001, ISBN 3-933761-12-3

110 Lang, Stefan: *Parallele numerische Simulation instätionärer Probleme mit adaptiven Methoden auf unstrukturierten Gittern*, 2001, ISBN 3-933761-13-1

111 Appt, Jochen; Stumpp Simone: *Die Bodensee-Messkampagne 2001, IWS/CWR Lake Constance Measurement Program 2001*, 2002, ISBN 3-933761-14-X

112 Heimerl, Stephan: *Systematische Beurteilung von Wasserkraftprojekten,* 2002, ISBN 3-933761-15-8, *vergriffen*

113 Iqbal, Amin: *On the Management and Salinity Control of Drip Irrigation,* 2002, ISBN 3-933761-16-6

114 Silberhorn-Hemminger, Annette: *Modellierung von Kluftaquifersystemen: Geostatistische Analyse und deterministisch-stochastische Kluftgenerierung,* 2002, ISBN 3-933761-17-4

115 Winkler, Angela: *Prozesse des Wärme- und Stofftransports bei der In-situ-Sanierung mit festen Wärmequellen,* 2003, ISBN 3-933761-18-2

116 Marx, Walter: *Wasserkraft, Bewässerung, Umwelt - Planungs- und Bewertungsschwerpunkte der Wasserbewirtschaftung,* 2003, ISBN 3-933761-19-0

117 Hinkelmann, Reinhard: *Efficient Numerical Methods and Information-Processing Techniques in Environment Water,* 2003, ISBN 3-933761-20-4

118 Samaniego-Eguiguren, Luis Eduardo: *Hydrological Consequences of Land Use / Land Cover and Climatic Changes in Mesoscale Catchments*, 2003, ISBN 3-933761-21-2

119 Neunhäuserer, Lina: *Diskretisierungsansätze zur Modellierung von Strömungs- und Transportprozessen in geklüftet-porösen Medien*, 2003, ISBN 3-933761-22-0

120 Paul, Maren: *Simulation of Two-Phase Flow in Heterogeneous Poros Media with Adaptive Methods*, 2003, ISBN 3-933761-23-9

121 Ehret, Uwe: *Rainfall and Flood Nowcasting in Small Catchments using Weather Radar*, 2003, ISBN 3-933761-24-7

122 Haag, Ingo: *Der Sauerstoffhaushalt staugeregelter Flüsse am Beispiel des Neckars - Analysen, Experimente, Simulationen -,* 2003, ISBN 3-933761-25-5

123 Appt, Jochen: *Analysis of Basin-Scale Internal Waves in Upper Lake Constance,* 2003, ISBN 3-933761-26-3

124 Hrsg.: Schrenk, Volker; Batereau, Katrin; Barczewski, Baldur; Weber, Karolin und Koschitzky, Hans-Peter: *Symposium Ressource Fläche und VEGAS - Statuskolloquium 2003, 30. September und 1. Oktober 2003,* 2003, ISBN 3-933761-27-1

125 Omar Khalil Ouda: *Optimisation of Agricultural Water Use: A Decision Support System for the Gaza Strip,* 2003, ISBN 3-933761-28-0

126 Batereau, Katrin: *Sensorbasierte Bodenluftmessung zur Vor-Ort-Erkundung von Schadensherden im Untergrund*, 2004, ISBN 3-933761-29-8

127 Witt, Oliver: *Erosionsstabilität von Gewässersedimenten mit Auswirkung auf den Stofftransport bei Hochwasser am Beispiel ausgewählter Stauhaltungen des Oberrheins*, 2004, ISBN 3-933761-30-1

128 Jakobs, Hartmut: *Simulation nicht-isothermer Gas-Wasser-Prozesse in komplexen Kluft-Matrix-Systemen*, 2004, ISBN 3-933761-31-X

129 Li, Chen-Chien: *Deterministisch-stochastisches Berechnungskonzept zur Beurteilung der Auswirkungen erosiver Hochwasserereignisse in Flussstauhaltungen,* 2004, ISBN 3-933761-32-8

130 Reichenberger, Volker; Helmig, Rainer; Jakobs, Hartmut; Bastian, Peter; Niessner, Jennifer: *Complex Gas-Water Processes in Discrete Fracture-Matrix Systems: Up-scaling, Mass-Conservative Discretization and Efficient Multilevel Solution,* 2004, ISBN 3-933761-33-6

131 Hrsg.: Barczewski, Baldur; Koschitzky, Hans-Peter; Weber, Karolin; Wege, Ralf: *VEGAS - Statuskolloquium 2004,* Tagungsband zur Veranstaltung am 05. Oktober 2004 an der Universität Stuttgart, Campus Stuttgart-Vaihingen, 2004, ISBN 3-933761-34-4

132 Asie, Kemal Jabir: *Finite Volume Models for Multiphase Multicomponent Flow through Porous Media*. 2005, ISBN 3-933761-35-2

133 Jacoub, George: *Development of a 2-D Numerical Module for Particulate Contaminant Transport in Flood Retention Reservoirs and Impounded Rivers,* 2004, ISBN 3-933761-36-0

134 Nowak, Wolfgang: *Geostatistical Methods for the Identification of Flow and Transport Parameters in the Subsurface,* 2005, ISBN 3-933761-37-9

135 Süß, Mia: *Analysis of the influence of structures and boundaries on flow and transport processes in fractured porous media*, 2005, ISBN 3-933761-38-7

136 Jose, Surabhin Chackiath: *Experimental Investigations on Longitudinal Dispersive Mixing in Heterogeneous Aquifers,* 2005, ISBN: 3-933761-39-5

137 Filiz, Fulya: *Linking Large-Scale Meteorological Conditions to Floods in Mesoscale Catchments,* 2005, ISBN 3-933761-40-9

138 Qin, Minghao: *Wirklichkeitsnahe und recheneffiziente Ermittlung von Temperatur und Spannungen bei großen RCC-Staumauern*, 2005, ISBN 3-933761-41-7

139 Kobayashi, Kenichiro: *Optimization Methods for Multiphase Systems in the Subsurface - Application to Methane Migration in Coal Mining Areas*, 2005, ISBN 3-933761-42-5

140 Rahman, Md. Arifur: *Experimental Investigations on Transverse Dispersive Mixing in Heterogeneous Porous Media,* 2005, ISBN 3-933761-43-3

141 Schrenk, Volker: *Ökobilanzen zur Bewertung von Altlastensanierungsmaßnahmen,* 2005, ISBN 3-933761-44-1

142 Hundecha, Hirpa Yeshewatesfa: *Regionalization of Parameters of a Conceptual Rainfall-Runoff Model*, 2005, ISBN: 3-933761-45-X

143 Wege, Ralf: *Untersuchungs- und Überwachungsmethoden für die Beurteilung natürlicher Selbstreinigungsprozesse im Grundwasser,* 2005, ISBN 3-933761-46-8

144 Breiting, Thomas: *Techniken und Methoden der Hydroinformatik - Modellierung von komplexen Hydrosystemen im Untergrund*, 2006, ISBN 3-933761-47-6

145 Hrsg.: Braun, Jürgen; Koschitzky, Hans-Peter; Müller, Martin: *Ressource Untergrund: 10 Jahre VEGAS: Forschung und Technologieentwicklung zum Schutz von Grundwasser und Boden,* Tagungsband zur Veranstaltung am 28. und 29. September 2005 an der Universität Stuttgart, Campus Stuttgart-Vaihingen, 2005, ISBN 3-933761-48-4

146 Rojanschi, Vlad: *Abflusskonzentration in mesoskaligen Einzugsgebieten unter Berücksichtigung des Sickerraumes,* 2006, ISBN 3-933761-49-2

147 Winkler, Nina Simone: *Optimierung der Steuerung von Hochwasserrückhaltebeckensystemen,* 2006, ISBN 3-933761-50-6

148 Wolf, Jens: *Räumlich differenzierte Modellierung der Grundwasserströmung alluvialer Aquifere für mesoskalige Einzugsgebiete*, 2006, ISBN: 3-933761-51-4

149 Kohler, Beate: *Externe Effekte der Laufwasserkraftnutzung*, 2006, ISBN 3-933761-52-2

150 Hrsg.: Braun, Jürgen; Koschitzky, Hans-Peter; Stuhrmann, Matthias: *VEGAS-Statuskolloquium 2006,* Tagungsband zur Veranstaltung am 28. September 2006 an der Universität Stuttgart, Campus Stuttgart-Vaihingen, 2006, ISBN 3-933761-53-0

151 Niessner, Jennifer: *Multi-Scale Modeling of Multi-Phase - Multi-Component Processes in Heterogeneous Porous Media*, 2006, ISBN 3-933761-54-9

152 Fischer, Markus: *Beanspruchung eingeerdeter Rohrleitungen infolge Austrocknung bindiger Böden,* 2006, ISBN 3-933761-55-7

153 Schneck, Alexander: *Optimierung der Grundwasserbewirtschaftung unter Berücksichtigung der Belange der Wasserversorgung, der Landwirtschaft und des Naturschutzes*, 2006, ISBN 3-933761-56-5

154 Das, Tapash: *The Impact of Spatial Variability of Precipitation on the Predictive Uncertainty of Hydrological Models,* 2006, ISBN 3-33761-57-3

155 Bielinski, Andreas: *Numerical Simulation of CO_2 sequestration in geological formations*, 2007, ISBN 3-933761-58-1

156 Mödinger, Jens: *Entwicklung eines Bewertungs- und Entscheidungsunterstützungssystems für eine nachhaltige regionale Grundwasserbewirtschaftung*, 2006, ISBN 3-933761-60-3

157 Manthey, Sabine: *Two-phase flow processes with dynamic effects in porous media - parameter estimation and simulation,* 2007, ISBN 3-933761-61-1

158 Pozos Estrada, Oscar: *Investigation on the Effects of Entrained Air in Pipelines,* 2007, ISBN 3-933761-62-X

159 Ochs, Steffen Oliver: *Steam injection into saturated porous media – process analysis including experimental and numerical investigations*, 2007, ISBN 3-933761-63-8

160 Marx, Andreas: *Einsatz gekoppelter Modelle und Wetterradar zur Abschätzung von Niederschlagsintensitäten und zur Abflussvorhersage, 2007,* ISBN 3-933761-64-6

161 Hartmann, Gabriele Maria: *Investigation of Evapotranspiration Concepts in Hydrological Modelling for Climate Change Impact Assessment*, 2007, ISBN 3-933761-65-4

162 Kebede Gurmessa, Tesfaye: *Numerical Investigation on Flow and Transport Characteristics to Improve Long-Term Simulation of Reservoir Sedimentation*, 2007, ISBN 3-933761-66-2

163 Trifković, Aleksandar: *Multi-objective and Risk-based Modelling Methodology for Planning, Design and Operation of Water Supply Systems*, 2007, ISBN 3-933761-67-0

164 Götzinger, Jens: *Distributed Conceptual Hydrological Modelling - Simulation of Climate, Land Use Change Impact and Uncertainty Analysis*, 2007, ISBN 3-933761-68-9

165 Hrsg.: Braun, Jürgen; Koschitzky, Hans-Peter; Stuhrmann, Matthias: *VEGAS – Kolloquium 2007,* Tagungsband zur Veranstaltung am 26. September 2007 an der Universität Stuttgart, Campus Stuttgart-Vaihingen, 2007, ISBN 3-933761-69-7

166 Freeman, Beau: *Modernization Criteria Assessment for Water Resources Planning; Klamath Irrigation Project, U.S.*, 2008, ISBN 3-933761-70-0

167 Dreher, Thomas: *Selektive Sedimentation von Feinstschwebstoffen in Wechselwirkung mit wandnahen turbulenten Strömungsbedingungen*, 2008, ISBN 3-933761-71-9

168 Yang, Wei: *Discrete-Continuous Downscaling Model for Generating Daily Precipitation Time Series*, 2008, ISBN 3-933761-72-7

169 Kopecki, Ianina: *Calculational Approach to FST-Hemispheres for Multiparametrical Benthos Habitat Modelling,* 2008*,* ISBN 3-933761-73-5

170 Brommundt, Jürgen: *Stochastische Generierung räumlich zusammenhängender Niederschlagszeitreihen*, 2008, ISBN 3-933761-74-3

171 Papafotiou, *Alexandros: Numerical Investigations of the Role of Hysteresis in Heterogeneous Two-Phase Flow Systems*, 2008, ISBN 3-933761-75-1

172 He, Yi: *Application of a Non-Parametric Classification Scheme to Catchment Hydrology*, 2008, ISBN 978-3-933761-76-7

173 Wagner, Sven: *Water Balance in a Poorly Gauged Basin in West Africa Using Atmospheric Modelling and Remote Sensing Information*, 2008, ISBN 978-3-933761-77-4

174 Hrsg.: Braun, Jürgen; Koschitzky, Hans-Peter; Stuhrmann, Matthias; Schrenk, Volker: *VEGAS-Kolloquium 2008 Ressource Fläche III*, Tagungsband zur Veranstaltung am 01. Oktober 2008 an der Universität Stuttgart, Campus Stuttgart-Vaihingen, 2008, ISBN 978-3-933761-78-1

175 Patil, Sachin: *Regionalization of an Event Based Nash Cascade Model for Flood Predictions in Ungauged Basins*, 2008, ISBN 978-3-933761-79-8

176 Assteerawatt, Anongnart: *Flow and Transport Modelling of Fractured Aquifers based on a Geostatistical Approach,* 2008, ISBN 978-3-933761-80-4

177 Karnahl, Joachim Alexander: *2D numerische Modellierung von multifraktionalem Schwebstoff- und Schadstofftransport in Flüssen*, 2008, ISBN 978-3-933761-81-1

178 Hiester, Uwe: *Technologieentwicklung zur In-situ-Sanierung der ungesättigten Bodenzone mit festen Wärmequellen,* 2009, ISBN 978-3-933761-82-8

179 Laux, Patrick: *Statistical Modeling of Precipitation for Agricultural Planning in the Volta Basin of West Africa,* 2009, ISBN 978-3-933761-83-5

180 Ehsan, Saqib: *Evaluation of Life Safety Risks Related to Severe Flooding,* 2009, ISBN 978-3-933761-84-2

181 Prohaska, Sandra: *Development and Application of a 1D Multi-Strip Fine Sediment Transport Model for Regulated Rivers,* 2009, ISBN 978-3-933761-85-9

182 Kopp, Andreas: *Evaluation of CO_2 Injection Processes in Geological Formations for Site Screening,* 2009, ISBN 978-3-933761-86-6

183 Ebigbo, Anozie: *Modelling of biofilm growth and its influence on CO_2 and water (two-phase) flow in porous media,* 2009, ISBN 978-3-933761-87-3

184 Freiboth, Sandra: *A phenomenological model for the numerical simulation of multiphase multicomponent processes considering structural alterations of porous media*, 2009, ISBN 978-3-933761-88-0

185 Zöllner, Frank: *Implementierung und Anwendung netzfreier Methoden im Konstruktiven Wasserbau und in der Hydromechanik*, 2009, ISBN 978-3-933761-89-7

186 Vasin, Milos: *Influence of the soil structure and property contrast on flow and transport in the unsaturated zone*, 2010, ISBN 978-3-933761-90-3

187 Li, Jing: *Application of Copulas as a New Geostatistical Tool*, 2010, ISBN 978-3-933761-91-0

188 AghaKouchak, Amir: *Simulation of Remotely Sensed Rainfall Fields Using Copulas*, 2010, ISBN 978-3-933761-92-7

189 Thapa, Pawan Kumar: *Physically-based spatially distributed rainfall runoff modelling for soil erosion estimation*, 2010, ISBN 978-3-933761-93-4

190 Wurms, Sven: *Numerische Modellierung der Sedimentationsprozesse in Retentionsanlagen zur Steuerung von Stoffströmen bei extremen Hochwasserabflussereignissen*, 2011, ISBN 978-3-933761-94-1

191 Merkel, Uwe: *Unsicherheitsanalyse hydraulischer Einwirkungen auf Hochwasserschutzdeiche und Steigerung der Leistungsfähigkeit durch adaptive Strömungsmodellierung*, 2011, ISBN 978-3-933761-95-8

192 Fritz, Jochen: *A Decoupled Model for Compositional Non-Isothermal Multiphase Flow in Porous Media and Multiphysics Approaches for Two-Phase Flow*, 2010, ISBN 978-3-933761-96-5

193 Weber, Karolin (Hrsg.): *12. Treffen junger WissenschaftlerInnen an Wasserbauinstituten*, 2010, ISBN 978-3-933761-97-2

194 Bliefernicht, Jan-Geert: *Probability Forecasts of Daily Areal Precipitation for Small River Basins,* 2011, ISBN 978-3-933761-98-9

195 Hrsg.: Koschitzky, Hans-Peter; Braun, Jürgen: *VEGAS-Kolloquium 2010 In-situ-Sanierung - Stand und Entwicklung Nano und ISCO -,* Tagungsband zur Veranstaltung am 07. Oktober 2010 an der Universität Stuttgart, Campus Stuttgart-Vaihingen*,* 2010*,* ISBN 978-3-933761-99-6

196 Gafurov, Abror: *Water Balance Modeling Using Remote Sensing Information - Focus on Central Asia,* 2010, ISBN 978-3-942036-00-9

197 Mackenberg, Sylvia: *Die Quellstärke in der Sickerwasserprognose: Möglichkeiten und Grenzen von Labor- und Freilanduntersuchungen,* 2010, ISBN 978-3-942036-01-6

198 Singh, Shailesh Kumar: *Robust Parameter Estimation in Gauged and Ungauged Basins,* 2010, ISBN 978-3-942036-02-3

199 Doğan, Mehmet Onur: *Coupling of porous media flow with pipe flow,* 2011, ISBN 978-3-942036-03-0

200 Liu, Min: *Study of Topographic Effects on Hydrological Patterns and the Implication on Hydrological Modeling and Data Interpolation,* 2011, ISBN 978-3-942036-04-7

201 Geleta, Habtamu Itefa: *Watershed Sediment Yield Modeling for Data Scarce Areas,* 2011, ISBN 978-3-942036-05-4

202 Franke, Jörg: *Einfluss der Überwachung auf die Versagenswahrscheinlichkeit von Staustufen,* 2011, ISBN 978-3-942036-06-1

203 Bakimchandra, Oinam: *Integrated Fuzzy-GIS approach for assessing regional soil erosion risks,* 2011, ISBN 978-3-942036-07-8

204 Alam, Muhammad Mahboob: *Statistical Downscaling of Extremes of Precipitation in Mesoscale Catchments from Different RCMs and Their Effects on Local Hydrology,* 2011, ISBN 978-3-942036-08-5

205 Hrsg.: Koschitzky, Hans-Peter; Braun, Jürgen: *VEGAS-Kolloquium 2011 Flache Geothermie - Perspektiven und Risiken,* Tagungsband zur Veranstaltung am 06. Oktober 2011 an der Universität Stuttgart, Campus Stuttgart-Vaihingen*,* 2011*,* ISBN 978-3-933761-09-2

206 Haslauer, Claus: *Analysis of Real-World Spatial Dependence of Subsurface Hydraulic Properties Using Copulas with a Focus on Solute Transport Behaviour,* 2011, ISBN 978-3-942036-10-8

207 Dung, Nguyen Viet: *Multi-objective automatic calibration of hydrodynamic models – development of the concept and an application in the Mekong Delta,* 2011, ISBN 978-3-942036-11-5

208 Hung, Nguyen Nghia: *Sediment dynamics in the floodplain of the Mekong Delta, Vietnam,* 2011, ISBN 978-3-942036-12-2

209 Kuhlmann, Anna: *Influence of soil structure and root water uptake on flow in the unsaturated zone,* 2012, ISBN 978-3-942036-13-9

210 Tuhtan, Jeffrey Andrew: *Including the Second Law Inequality in Aquatic Ecodynamics: A Modeling Approach for Alpine Rivers Impacted by Hydropeaking,* 2012, ISBN 978-3-942036-14-6

211 Tolossa, Habtamu: *Sediment Transport Computation Using a Data-Driven Adaptive Neuro-Fuzzy Modelling Approach,* 2012, ISBN 978-3-942036-15-3

212 Tatomir, Alexandru-Bodgan: *From Discrete to Continuum Concepts of Flow in Fractured Porous Media,* 2012, ISBN 978-3-942036-16-0

213 Erbertseder, Karin: *A Multi-Scale Model for Describing Cancer-Therapeutic Transport in the Human Lung,* 2012, ISBN 978-3-942036-17-7

214 Noack, Markus: *Modelling Approach for Interstitial Sediment Dynamics and Reproduction of Gravel Spawning Fish,* 2012, ISBN 978-3-942036-18-4

215 De Boer, Cjestmir Volkert: *Transport of Nano Sized Zero Valent Iron Colloids during Injection into the Subsurface*, 2012, ISBN 978-3-942036-19-1

216 Pfaff, Thomas: *Processing and Analysis of Weather Radar Data for Use in Hydrology*, 2013, ISBN 978-3-942036-20-7

217 Lebrenz, Hans-Henning: *Addressing the Input Uncertainty for Hydrological Modeling by a New Geostatistical Method*, 2013, ISBN 978-3-942036-21-4

218 Darcis, Melanie Yvonne: *Coupling Models of Different Complexity for the Simulation of CO_2 Storage in Deep Saline Aquifers*, 2013, ISBN 978-3-942036-22-1

219 Beck, Ferdinand: *Generation of Spatially Correlated Synthetic Rainfall Time Series in High Temporal Resolution - A Data Driven Approach*, 2013, ISBN 978-3-942036-23-8

220 Guthke, Philipp: *Non-multi-Gaussian spatial structures: Process-driven natural genesis, manifestation, modeling approaches, and influences on dependent processes*, 2013, ISBN 978-3-942036-24-5

221 Walter, Lena: *Uncertainty studies and risk assessment for CO_2 storage in geological formations*, 2013, ISBN 978-3-942036-25-2

222 Wolff, Markus: *Multi-scale modeling of two-phase flow in porous media including capillary pressure effects,* 2013, ISBN 978-3-942036-26-9

223 Mosthaf, Klaus Roland: *Modeling and analysis of coupled porous-medium and free flow with application to evaporation processes,* 2014, ISBN 978-3-942036-27-6

224 Leube, Philipp Christoph: *Methods for Physically-Based Model Reduction in Time: Analysis, Comparison of Methods and Application*, 2013, ISBN 978-3-942036-28-3

225 Rodríguez Fernández, Jhan Ignacio: *High Order Interactions among environmental variables: Diagnostics and initial steps towards modeling*, 2013, ISBN 978-3-942036-29-0

226 Eder, Maria Magdalena: *Climate Sensitivity of a Large Lake*, 2013, ISBN 978-3-942036-30-6

227 Greiner, Philipp: *Alkoholinjektion zur In-situ-Sanierung von CKW Schadensherden in Grundwasserleitern: Charakterisierung der relevanten Prozesse auf unterschiedlichen Skalen*, 2014, ISBN 978-3-942036-31-3

228 Lauser, Andreas: *Theory and Numerical Applications of Compositional Multi-Phase Flow in Porous Media*, 2014, ISBN 978-3-942036-32-0

229 Enzenhöfer, Rainer: *Risk Quantification and Management in Water Production and Supply Systems*, 2014, ISBN 978-3-942036-33-7

230 Faigle, Benjamin: *Adaptive modelling of compositional multi-phase flow with capillary pressure*, 2014, ISBN 978-3-942036-34-4

231 Oladyshkin, Sergey: *Efficient modeling of environmental systems in the face of complexity and uncertainty*, 2014, ISBN 978-3-942036-35-1

232 Sugimoto, Takayuki: *Copula based Stochastic Analysis of Discharge Time Series*, 2014, ISBN 978-3-942036-36-8

233 Koch, Jonas: *Simulation, Identification and Characterization of Contaminant Source Architectures in the Subsurface*, 2014, ISBN 978-3-942036-37-5

234 Zhang, Jin: *Investigations on Urban River Regulation and Ecological Rehabilitation Measures, Case of Shenzhen in China*, 2014, ISBN 978-3-942036-38-2

235 Siebel, Rüdiger: *Experimentelle Untersuchungen zur hydrodynamischen Belastung und Standsicherheit von Deckwerken an überströmbaren Erddämmen,* 2014, ISBN 978-3-942036-39-9

236 Baber, Katherina: *Coupling free flow and flow in porous media in biological and technical applications: From a simple to a complex interface description,* 2014, ISBN 978-3-942036-40-5

237 Nuske, Klaus Philipp: *Beyond Local Equilibrium — Relaxing local equilibrium assumptions in multiphase flow in porous media,* 2014, ISBN 978-3-942036-41-2

238 Geiges, Andreas: *Efficient concepts for optimal experimental design in nonlinear environmental systems*, 2014, ISBN 978-3-942036-42-9

239 Schwenck, Nicolas: *An XFEM-Based Model for Fluid Flow in Fractured Porous Media*, 2014, ISBN 978-3-942036-43-6

240 Chamorro Chávez, Alejandro: *Stochastic and hydrological modelling for climate change prediction in the Lima region, Peru*, 2015, ISBN 978-3-942036-44-3

241 Yulizar: *Investigation of Changes in Hydro-Meteorological Time Series Using a Depth-Based Approach*, 2015, ISBN 978-3-942036-45-0

242 Kretschmer, Nicole: *Impacts of the existing water allocation scheme on the Limarí watershed – Chile, an integrative approach*, 2015, ISBN 978-3-942036-46-7

243 Kramer, Matthias: *Luftbedarf von Freistrahlturbinen im Gegendruckbetrieb*, 2015, ISBN 978-3-942036-47-4

244 Hommel, Johannes: *Modeling biogeochemical and mass transport processes in the subsurface: Investigation of microbially induced calcite precipitation*, 2016, ISBN 978-3-942036-48-1

245 Germer, Kai: *Wasserinfiltration in die ungesättigte Zone eines makroporösen Hanges und deren Einfluss auf die Hangstabilität*, 2016, ISBN 978-3-942036-49-8

246 Hörning, Sebastian: *Process-oriented modeling of spatial random fields using copulas*, 2016, ISBN 978-3-942036-50-4

247 Jambhekar, Vishal: *Numerical modeling and analysis of evaporative salinization in a coupled free-flow porous-media system,* 2016, ISBN 978-3-942036-51-1

248 Huang, Yingchun: *Study on the spatial and temporal transferability of conceptual hydrological models*, 2016, ISBN 978-3-942036-52-8

249 Kleinknecht, Simon Matthias: *Migration and retention of a heavy NAPL vapor and remediation of the unsaturated zone*, 2016, ISBN 978-3-942036-53-5

250 Kwakye, Stephen Oppong: *Study on the effects of climate change on the hydrology of the West African sub-region*, 2016, ISBN 978-3-942036-54-2

251 Kissinger, Alexander: *Basin-Scale Site Screening and Investigation of Possible Impacts of CO_2 Storage on Subsurface Hydrosystems*, 2016, ISBN 978-3-942036-55-9

252 Müller, Thomas: *Generation of a Realistic Temporal Structure of Synthetic Precipitation Time Series for Sewer Applications*, 2017, ISBN 978-3-942036-56-6

253 Grüninger, Christoph: *Numerical Coupling of Navier-Stokes and Darcy Flow for Soil-Water Evaporation*, 2017, ISBN 978-3-942036-57-3

254 Suroso: *Asymmetric Dependence Based Spatial Copula Models: Empirical Investigations and Consequences on Precipitation Fields*, 2017, ISBN 978-3-942036-58-0

255 Müller, Thomas; Mosthaf, Tobias; Gunzenhauser, Sarah; Seidel, Jochen; Bárdossy, András: *Grundlagenbericht Niederschlags-Simulator (NiedSim3)*, 2017, ISBN 978-3-942036-59-7

256 Mosthaf, Tobias: *New Concepts for Regionalizing Temporal Distributions of Precipitation and for its Application in Spatial Rainfall Simulation,* 2017, ISBN 978-3-942036-60-3

257 Fenrich, Eva Katrin: *Entwicklung eines ökologisch-ökonomischen Vernetzungsmodells für Wasserkraftanlagen und Mehrzweckspeicher,* 2018, ISBN 978-3-942036-61-0

258 Schmidt, Holger: *Microbial stabilization of lotic fine sediments*, 2018, ISBN 978-3-942036-62-7

259 Fetzer, Thomas: *Coupled Free and Porous-Medium Flow Processes Affected by Turbulence and Roughness – Models, Concepts and Analysis*, 2018, ISBN 978-3-942036-63-4

260 Schröder, Hans Christoph: *Large-scale High Head Pico Hydropower Potential Assessment*, 2018, ISBN 978-3-942036-64-1

261 Bode, Felix: *Early-Warning Monitoring Systems for Improved Drinking Water Resource Protection*, 2018, ISBN 978-3-942036-65-8

262 Gebler, Tobias: *Statistische Auswertung von simulierten Talsperrenüberwachungsdaten zur Identifikation von Schadensprozessen an Gewichtsstaumauern*, 2018, ISBN 978-3-942036-66-5

263 Harten, Matthias von: *Analyse des Zuppinger-Wasserrades – Hydraulische Optimierungen unter Berücksichtigung ökologischer Aspekte*, 2018, ISBN 978-3-942036-67-2

264 Yan, Jieru: *Nonlinear estimation of short time precipitation using weather radar and surface observations*, 2018, ISBN 978-3-942036-68-9

265 Beck, Martin: *Conceptual approaches for the analysis of coupled hydraulic and geomechanical processes*, 2019, ISBN 978-3-942036-69-6

Die Mitteilungshefte ab der Nr. 134 (Jg. 2005) stehen als pdf-Datei über die Homepage des Instituts: www.iws.uni-stuttgart.de zur Verfügung.